



저작자표시-비영리-변경금지 2.0 대한민국

이용자는 아래의 조건을 따르는 경우에 한하여 자유롭게

- 이 저작물을 복제, 배포, 전송, 전시, 공연 및 방송할 수 있습니다.

다음과 같은 조건을 따라야 합니다:



저작자표시. 귀하는 원저작자를 표시하여야 합니다.



비영리. 귀하는 이 저작물을 영리 목적으로 이용할 수 없습니다.



변경금지. 귀하는 이 저작물을 개작, 변형 또는 가공할 수 없습니다.

- 귀하는, 이 저작물의 재이용이나 배포의 경우, 이 저작물에 적용된 이용허락조건을 명확하게 나타내어야 합니다.
- 저작권자로부터 별도의 허가를 받으면 이러한 조건들은 적용되지 않습니다.

저작권법에 따른 이용자의 권리는 위의 내용에 의하여 영향을 받지 않습니다.

이것은 [이용허락규약\(Legal Code\)](#)을 이해하기 쉽게 요약한 것입니다.

[Disclaimer](#)

공학박사 학위논문

**Estimation of Cyclic Deformation and Static
Fracture Characteristic of Metallic Materials
Using Cyclic/Static Indentation Test**

반복/정적압입시험을 이용한
금속소재의 반복소성변형 및 정적파괴 특성 평가

2017 년 2 월

서울대학교 대학원

재료공학부

전 승 원

Estimation of Cyclic Deformation and Static Fracture Characteristic of Metallic Materials Using Cyclic/Static Indentation Test

반복/정적압입시험을 이용한
금속소재의 반복소성변형 및 정적파괴 특성 평가

지도교수 권 동 일

이 논문을 공학박사 학위논문으로 제출함
2016년 12월

서울대학교 대학원
재료공학부
전 승 원

전승원의 박사학위논문을 인준함
2016년 12월

위 원 장 
부위원장 
위 원 
위 원 
위 원 

Abstract

Jeon, Seung-Won

Dept. Materials Science and Engineering

The Graduate School

Seoul National University

Structural integrity concerns with the ability of a structure or component to support the designed service load without failure caused by deformation, fracture or fatigue. To construct an item with structural integrity, an engineer must first consider the mechanical properties of the material, such as strength, hardness, fracture toughness and fatigue properties and then determine a suitable size, thickness, or shape that will endure the necessary loading for a long lifetime. In many cases, structural failure occurs because of changes in the material's mechanical properties due to degradation or embrittlement, so that measuring the in-situ mechanical properties of in-service structural components is required to assess structural integrity. Fatigue properties and fracture toughness, which are among the most important properties required for structural integrity, can be determined using standardized test methods such as

those developed by ASTM and BS. However, these methods cannot be applied directly to in-service structures or to small-volume regions of material such as the weld zone because they require specific specimen dimensions and complex test procedures. For this reason, an alternative test method to measure in-situ mechanical properties has been developed. Instrumented indentation testing (IIT), developed for nondestructive testing of in field structures, can be used to measure such mechanical properties as hardness, elastic modulus, tensile properties, residual stress, and fracture toughness by analysis of the indentation load-depth curve. IIT makes just a small indent on the material surface and hence can be applied in in-situ and in-field measurement as nondestructive mechanical testing as well as for property mapping by local area testing on multi-scale levels. Most studies on instrumented indentation testing have focused on static indentation testing, and little work has been done on cyclic indentation testing. Cyclic indentation testing has great potential to complement conventional cyclic or fatigue testing because the advantages of static IIT also apply to cyclic indentation. In this thesis, we adapt cyclic instrumented indentation testing to evaluate fatigue properties. Two kinds of control mode on cyclic indentation are used; cyclic indentation depth-controlled mode and cyclic indentation load-

controlled mode. In cyclic indentation depth-controlled testing, hysteresis loop observed in indentation load-depth and is found to be caused by Bauschinger effect induced by kinematic hardening. Therefore, we develop a model for evaluating the uniaxial Bauschinger effect, which is also called backstress. In the load-controlled test, we observed that indentation depth continuously increases and saturates at a certain cycle. We analyze this phenomenon in terms of hardening behavior and confirm that increase in indentation depth behavior is similar to uniaxial ratcheting behavior. Therefore, we develop the new model for estimating material ratcheting property. The estimated Bauschinger effect and material ratcheting property were compared to values obtained in conventional fatigue tests.

In addition, static flat punch indentation is also used to develop a criterion for estimating fracture characteristics. For ductile materials like metals, cracking does not occur during indentation. Many researchers have worked to estimate the fracture toughness of metallic materials using instrumented indentation testing and trying to develop theoretical or experimental models. Most such models are one of two types: the models for brittle metallic materials or the models for ductile metallic materials. For brittle metallic materials, the estimated fracture toughness

has been limited to specific ranges for relatively low fracture toughness ($K_{JC} < 120 \text{ MPa}\cdot\text{m}^{0.5}$), that is, in the lower shelf region of the ductile-brittle transition curve. For ductile metallic materials, the estimated fracture toughness has been limited to a specific range for relatively large fracture toughness ($K_{JC} > 250 \text{ MPa}\cdot\text{m}^{0.5}$) or in the upper shelf region of the ductile-brittle transition curve. Therefore, distinguishing the two types of model or selecting a specific models are important issues. We propose a criterion for estimating whether a material is in the range of brittle fracture characteristic ($K_{JC} < 120 \text{ MPa}\cdot\text{m}^{0.5}$) or ductile fracture characteristic ($K_{JC} > 250 \text{ MPa}\cdot\text{m}^{0.5}$) using static flat punch indentation. The two key factors for developing the criterion are determined based on equivalence of fracture mechanics and contact mechanics. The fracture toughness values of 23 kinds of materials obtained from conventional fracture toughness testing are compared to the proposed criterion for verification.

Keyword: Cyclic indentation; Flat punch indentation; Bauschinger effect; Material ratcheting; Brittle fracture; Ductile fracture; Structural integrity

Student Number: 2010-20629

Contents

Abstract	i
Contents	v
List of Tables	vii
List of Figures	viii
Chapter 1. Introduction	1
1.1. Objective and Scope of this Study	2
1.2. Outline of the Thesis	7
Chapter 2. Research Background	8
2.1. Cyclic stress-strain behavior	9
2.1.1. Cyclic hardening and softening	9
2.1.2. Bauschinger effect	10
2.1.3. Ratcheting or Cyclic creep	15
2.2. Fracture Mechanics	24
2.2.1. Stress Analysis of Cracks	24
2.2.2. Fracture Toughness Parameters	28
2.2.3. Equivalence of Fracture mechanics and Contact mechanics ..	40
2.3. Instrumented Indentation Testing	47
2.3.1. Introduction and Application	47
2.3.2. Static Indentation for Estimating Fracture Toughness	66
2.3.3. Cyclic Indentation for Estimating Fatigue properties	78

Chapter 3. Estimation of fatigue properties using cyclic indentation	..	86
3.1 Motivation and Research Flow	87
3.2. Estimation of Bauschinger effect	89
3.2.1 Introduction	89
3.2.2 Theoretical Modeling	90
3.2.3 Experimental Verification	96
3.3 Estimation of Material Ratcheting Property	108
3.3.1 Introduction	108
3.3.2 Phenomenological Modeling	111
3.3.3 Experimental Verification	115
Chapter 4. Development of Fracture criterion using static indentation	125
4.1. Introduction	126
4.2. Empirical Modeling	129
4.3. Experimental Verification	135
Chapter 5. Conclusions	148
Reference	151
Abstract in Korean	159
List of Publications	163

List of Tables

Table 2.1 Stress fields ahead of crack tip for Mode

Table 3.1. Experimental condition detail for uniaxial ratcheting test.

Table 4.1. List and fracture toughness for tested materials

List of Figures

Figure 2.1. Schematic diagram of cyclic hardening and softening behavior

Figure 2.2. Schematic diagram of Bauschinger effect.

Figure 2.3. Schematic of stress-strain curve for fully reversed loading and replotting curve.

Figure 2.4. Block diagram of ratcheting

Figure 2.5. Illustration of material ratchetting phenomenon.

Figure 2.6. Effect of thickness on K_C behavior.

Figure 2.7. Constraint to plastic flow caused by notched geometries.

Figure 2.8. Crack tip opening displacement (CTOD). An initially sharp crack blunts with plastic deformation, resulting in a finite displacement, δ , at the crack tip.

Figure 2.9. Alternative definitions of CTOD: (a) displacement at the original crack tip and (b) displacement at the intersection of a 90° vertex with the crack flanks.

Figure 2.10. Arbitrary contour around the tip of a crack.

Figure 2.11. Schematic of flat punch indentation

Figure 2.12. A schematic representation of the contact between the end of a right-circular cylindrical punch and a substrate.

Figure 2.13. Crack analogue of Figure 2.25 showing the circumferentially cracked cylindrical rod specimen, and the associated nomenclature.

Figure 2.14. Schematic diagram of typical load-depth curve obtainable during instrumented indentations

Figure 2.15. Algorithm for evaluating indentation tensile properties

Figure 2.16. Variation of indentation loading curves with changes in the stress state.

Figure 2.17. Theoretical surface morphologies around the contact for (a) stress-free, (b) tensile stress, and (c) compressive stress states.

Figure 2.18. Crack system for Vickers indenter: (a) radial cracks, (b) lateral cracks, (c) median cracks, and (d) half-penny cracks.

Figure 2.19. Schematic of radial cracking by Vickers indentation.

Figure 2.20. Decreasing elastic modulus with indentation depth (API steels)

Figure 2.21. Hysteresis loops in indentation load-depth curve due to kinematic hardening

Figure 2.22. Experimental indentation curve under cycle loading (Above: indentation load-depth curve, Below: indentation depth-cycle curve)

Figure 2.23. Indentation depth-cycles curve and surface topography ((a) Evolution of indentation depth with acoustic emission count, (b) Surface topography near the impression after failure)

Figure 3.1. Reversed plastic yielding during unloading process

Figure 3.2. Comparison of indentation Bauschinger effect and uniaxial Bauschinger effect

Figure 3.3. Effect of loading rate on indentation hysteresis loop

Figure 3.4. material dependency on indentation hysteresis loop

Figure 3.5. Testing machine for obtaining Bauschinger effect

Figure 3.6. Comparison of indentation Bauschinger effect and Uniaxial Bauschinger effect at strain rate 0.6%, 0.9% (the dotted lines indicate a deviation of 30 %)

Figure 3.7. Comparison of indentation Bauschinger effect and Uniaxial Bauschinger effect at strain rate 1.2%, 1.5% (the dotted lines indicate a deviation of 30 %)

Figure 3.8. Comparison of cyclic depth-controlled test and cyclic load-controlled test.

Figure 3.9. Effect of hardening rule on cyclic indentation curve

Figure 3.10. Determination of steady-state indentation strain rate.

Figure 3.11. Example of indentation load-depth curve under cyclic loading test.(Material: Carbon steel(S45c))

Figure 3.12. Results of indentation ratcheting test for 4 kinds of materials

Figure 3.13 Log-log plot of indentation ratcheting test for 4 kinds of materials

Figure 3.14 Results of uniaxial ratcheting tests

Figure 4.1 Finite element model of flat punch indentation

Figure 4.2. Development of plastic zone beneath flat punch indenter

Figure 4.3. Geometrical similarity between flat punch indenter and circumferentially cracked round bar specimen

Figure 4.4 Equivalence of cracked round bar specimen and flat punch specimen

Figure 4.5 Determination of key parameters from flat punch curve

Figure 4.6 Indentation load-depth curves using flat punch indenters of various indenter radiuses

Figure 4.7 Normalization of indentation load-depth curves using flat punch indenters of various indenter radius

Figure 4.8 Results of verification for the criterion

Chapter 1

INTRODUCTION

Contents

1.1. Objective and Scope of this Thesis	2
1.2. Outline of the Thesis	7

1.1. Objective and Scope of this Thesis

Structural integrity is the ability of a structure or component to support a designed service load without failure caused by deformation, fracture and fatigue. In engineering, the concept of structural integrity is applied to produce items that will function adequately not only for their designed purpose but also for their desired service life. To construct an item with structural integrity, an engineer must first consider the mechanical properties of the material, such as strength, hardness, fracture toughness and fatigue properties and then determine the suitable size, thickness, or shape that will resist the desired loading for a long life. Structure failure is the loss of structural integrity. In many cases, structural failure occurs from changes in mechanical properties of the material due to degradation or embrittlement, so that to assess structural integrity it is necessary to measure in-situ mechanical properties of in-service structural components.

Fatigue properties, roughly defined as material's deformation and failure resistance under cyclic loading, are among the most important properties required in structural integrity. Fatigue is the weakening of a material caused by repeatedly applied service loads. Progressive and localized structural damage occurs when a material is subjected to cyclic loading.

Fracture toughness, defined as a material's resistance to crack propagation, is also important for structural integrity. Fracture toughness is a quantitative way of expressing a material's resistance to brittle or ductile fracture. Embrittlement caused by a structure's service condition (low temperature, hydrogen absorption, neutron radiation, etc.) can induce early failure.

Fatigue properties and fracture toughness can be measured using standardized test method such as those developed by ASTM and BS [1-5]. However, these methods cannot be applied directly to in-service structures or small-volume regions of material such as weld zones because they require specific specimen dimensions and complex test procedures. For this reason, an alternative test method to measure in-situ mechanical properties has been developed to improve the reliability of structural integrity assessment.

Among the alternative test methods available, instrumented Indentation testing (IIT) is widely used, which measures penetration depth and applied load continuously under static indentation loading, is most often applied to evaluate mechanical properties such as hardness, elastic modulus [33-35], flow properties [36-49], residual stress [50-54], fracture toughness [55-64]. IIT attracts much interest as an in-situ nondestructive

testing method for evaluating mechanical properties of in-service structures or components because of its simplicity and non-destructive nature. In addition, IIT can be applied to small-scale (micro, nano, pico-scale) structures because the indentation load can be easily controlled from macro to pico ranges.

However, most studies on instrumented indentation testing have focused on static indentation testing, and research on cyclic indentation testing has not evolved greatly. Cyclic indentation testing has great potential to complement conventional cyclic or fatigue testing because the advantages of static IIT can be applied to cyclic indentation. Cyclic indentation testing can be applied to components and materials to which conventional fatigue testing is difficult or impossible to apply: in-service structures and components, weld zones, micro/nano thin films, etc.

In chapter 3 of this thesis, therefore, we attempt to evaluate fatigue properties using cyclic instrumented indentation testing. The two kinds of control mode in cyclic indentation are used; cyclic indentation depth-controlled and cyclic indentation load-controlled mode. In cyclic indentation depth-controlled testing, we found a hysteresis loop in the indentation load-depth curve and analyze its cause using contact mechanics. The hysteresis loop is caused by Bauschinger effect which is

induced by kinematic hardening of material, so that we develop a model for evaluating a uniaxial Bauschinger effect, also called back stress, using cyclic indentation depth-controlled tests. In the load-controlled test, we observed that indentation depth continuously increases and saturates at a certain cycle and also that a hysteresis loop appear in the load-depth curve. We analyze the phenomenon in terms of hardening behavior. The indentation depth increase behavior is similar to uniaxial ratcheting behavior, so that we develop a model for estimating material ratcheting property. Finally, the estimated Bauschinger effect and material ratcheting property were compared to values obtained in conventional fatigue tests.

Chapter 4 of this thesis develops a criterion for estimating fracture characteristics of materials using static flat punch indentation. For ductile materials like metals, cracking does not occur during indentation. Many researchers have worked to estimate fracture toughness of metallic materials using instrumented indentation testing, trying to develop theoretical or experimental models. Most models are of one of two types: for brittle metallic materials or for ductile metallic materials. For brittle metallic materials, the estimated fracture toughness has been limited to specific ranges for relatively low fracture toughness ($K_{IC} < 100 \text{ MPa}\cdot\text{m}^{0.5}$),

or in the lower shelf region of the ductile-brittle transition curve. For ductile metallic materials, the estimated value has been limited to specific ranges for relatively large fracture toughness ($K_{JC} > 250 \text{ MPa}\cdot\text{m}^{0.5}$), or in the upper shelf region of the ductile-brittle transition curve. Therefore, distinguishing the model type and selecting a specific model are important issues. We must know preliminarily whether the material of interest corresponds to a brittle metallic model or ductile metallic model when its composition is unknown or its fracture toughness is altered due to embrittlement induced by degradation or low temperatures.

We propose a criterion for estimating whether a material involves a range of brittle fracture characteristic ($K_{JC} < 100 \text{ MPa}\cdot\text{m}^{0.5}$) or ductile fracture characteristic ($K_{JC} < 250 \text{ MPa}\cdot\text{m}^{0.5}$) using static flat punch indentation. The two key factors for developing the criterion are determined using the equivalence of fracture mechanics and contact mechanics. Fracture toughness values for 23 kinds of materials obtained from conventional fracture toughness testing are compared to the criterion for verification purpose.

1.2. Outline of the Thesis

The thesis has five chapters. The objective and organization of thesis are introduced in Chapter 1. Chapter 2 gives theoretical background on cyclic hardening and softening behavior and also reviews the Bauschinger effect and material ratcheting behavior. Chapter 3 presents two new models for estimating fatigue properties. A theoretical modeling to estimate the Bauschinger effect is presented in Chapter 3.1 and phenomenological model for estimating the material ratcheting property is presented in Chapter 3.2. Chapter 4 discusses a new criterion for distinguishing brittle or ductile fracture characteristics. Experimental work to verify developed models is described and the results are discussed. Finally, conclusions and recommendations for further study are given in Chapter 5.

Chapter 2

RESEARCH BACKGROUND

Contents

2.1	Cyclic stress-strain behavior	9
2.1.1.	Cyclic Hardening and Softening	
2.1.2.	Bauschinger Effect	
2.1.3.	Ratcheting or Cyclic Creep	
2.2	Fracture Mechanics	24
2.2.1.	Stress Analysis of Cracks	
2.2.2.	Fracture Toughness Parameters	
2.2.3.	Equivalence of Fracture mechanics and Contact mechanics	
2.3	Instrumented Indentation Testing	47
2.3.1.	Introduction and Application	
2.3.2.	Static Indentation for Estimating Fracture Toughness	
2.3.3.	Cyclic Indentation for Estimating Fatigue Properties	

2.1. Cyclic stress-strain behavior

2.1.1. Cyclic Hardening and Softening

Here we briefly review the fundamentals of cyclic hardening and softening behavior [6]. Cyclic hardening and softening is a change in the strength with a loading cycle that may occur through cyclic test or even in the first stage of cyclic deformation. Schematic examples of cyclic hardening and cyclic softening are shown in Figure 2.1. The stress course and the hysteresis loop shape from a symmetrical stress-controlled fatigue test with constant amplitude. Cyclic hardening causes an increase in the stress amplitude, and consequently the hysteresis loop becomes larger. Cyclic softening has the opposite effect. A decrease of stress amplitude and a reduction of the size of the hysteresis loop. The type of cyclic hardening and softening behavior is commonly determined by the pre-condition of the material tested. For example, cold working prior to cyclic loading can cause subsequent cyclic softening, while a recrystallization treatment can give rise to cyclic hardening. In addition, microstructural changes induced plastic deformation can also be the reason for cyclic hardening and softening deformation behavior. In case

of asymmetry cyclic deformation, it is common that cyclic hardening and softening processes take place that tend to reduce asymmetry. Figure 2.1 shows the situation in a strain-controlled test in which a mean strain is superimposed. As a consequence, a mean stress arise that slowly diminishes. This process is termed cyclic relaxation. If the test is performed under stress control with mean stress is applied, the material may exhibit cyclic creep (or ratcheting). The mean strain increases continuously, leading to a shift of the hysteresis loop to the right.

2.1.2. Bauschinger Effect

2.1.2.1. Introduction

Bauschinger [7] was the first confirm that after plastic deformation of a metallic material in tension or compression, the material yields at a lower stress when the direction of loading is reversed than in forward deformation. A schematic illustration of the Bauschinger effect is shown in Figure 2.2 [8]. The Bauschinger effect is central to cyclic plasticity, and understanding the mechanism of this effect is necessary to develop constitutive models for complex cyclic deformation, to analyze the work-

hardening phenomenon and to understand fatigue effects such as cyclic creep [10]. In cyclic loading, the Bauschinger effect takes place without additional mean stress or strain. It is known that the Bauschinger effects in precipitation-hardened steel continues even after a stable hysteresis loop is achieved [12]. In addition, the loss in strength caused by the Bauschinger effect has practical significance. After manufacturing processes that use cold working, if the working stress is applied to a component in reverse loading, its strength is seriously decreased [12]. Moreover, low flow stresses occur under in-service conditions because most metals exhibit the Bauschinger effect. Therefore the Bauschinger effect must be quantitatively evaluated in manufacturing processes and in-service conditions.

2.1.2.2. Bauschinger Parameter

Suresh [8] introduced parameters related to the Bauschinger effect and we review them here to quantify Bauschinger effect in terms of stress and strain. The schematic stress-strain curve for reverse loading in compression following pre-straining in tension is shown in Figure 2.3. Defining the magnitude of the reverse strain, $\Delta\epsilon_b$, is a common way to

quantify the Bauschinger effect and characterizes the Bauschinger strain. However, the flow stress difference between tension and compression at a certain strain values can be determined by replotting the stress-strain curve as shown in Figure 2.3. This figure illustrates only the magnitudes of the stress and the accumulated strain; ABCD represents the tensile loading part and DEF is the compressive loading part. If the tensile-hardening part is extrapolated to point C', the difference in magnitude between flow stresses in the nearly parallel segments CC' and EF gives an indication of the Bauschinger effect in terms of stress, $\Delta\sigma_b$, and it characterizes the amount of permanent softening.

2.1.2.3. Previous Approaches and Models

1) Continuum approach

Two sorts of work hardening have been widely used in continuum mechanics; isotropic and kinematic hardening. Isotropic hardening occurs when the initial yield surface, which can be either isotropic or anisotropic, expands uniformly during plastic flow. Kinematic hardening occurs when the initial yield surface translates in stress space, but the size of initial

yield surface does not change during plastic flow. The basic concept of the two kinds of hardening extends to develop theoretical models to describe work-hardening behavior as well as the Bauschinger effect [12]. However, even sophisticated models do not yield a priori descriptions of the actual behavior. Some measurements must inevitably be made on materials in order to provide numerical quantities for coefficients in theoretical models.

2) Microscopic approach

Plastic flow is inhomogeneous on the level of dislocations, grains, second-phase inclusions, etc. [12], and this in-homogeneities give rise to material incompatibilities and hence to occur internal stresses. The internal stresses can be divided into short-range or long-range. While short-range stresses are related to dislocation arrangements and inter-particle spacing, the long-range stresses are a function of incompatibilities between particles and the matrix. It is these long-range stresses that give rise to the Bauschinger effect. The stresses, called back stresses, can be estimated from forward and reverse plastic flow test.

3) Theoretical models

Permanent softening can be calculated when the forward and reverse loading curve are parallel. In general, the permanent softening provides a means of evaluating the back stresses. However, parallelism of the curve is difficult to assess and in certain instances convergence may be indicated if the curve can be extrapolated reliably. Various models have been developed to reproduce the forward and reverse flow characteristics of real materials [12].

- Model based on residual stresses
- Hardening model using elastic-plastic elements (the Masing model)
- Combined kinematic and isotropic hardening model
- Work-hardening models based on the translation, expansion and distortion of an initial yield surface
- Microscopic models

2.1.3. Material Ratcheting

2.1.3.1. Definition

Ratcheting is widely accepted as phenomenon which the progressive plastic strain accumulation caused by asymmetric cyclic stress [14], i.e. a tension stress level not equal to compressive stress level under uniaxial cyclic stress condition (the mean stress is not zero). The term of ratcheting can be specifically defined in two ways; structural ratcheting and material ratcheting [14].

Structural ratcheting can occur under cyclic loading even if there is no material ratcheting and is commonly caused by inhomogeneity in the stress state of a structure.

Material ratcheting can occur under cyclic loading without structural effects. If stress is distributed homogeneously in a certain structure, a material ratcheting effect can be observed in that structure. Almost all materials show ratcheting behavior under even homogeneous stresses, so that ratcheting behavior can be defined as a material property.

2.1.3.2. Importance of material ratcheting

The ratcheting phenomenon should be considered as an aspect of structural integrity because it induces early failure. Figure 2.4 gives a schematic diagram of ratcheting [9]. When two damage mechanisms, fatigue damage and accumulation of ratcheting strain, occur together, they can lead to early failure of in-service structures. Ratcheting also has a strong influence on fatigue in various engineering applications. For example, in case of component undergo contact fatigue (railroad rails, bearings, gears), an asymmetrical load cycle is imposed on the deformed region beneath the component surface. Hence, crack and incremental collapse frequently take place in the component, and hence ratcheting behavior must be evaluated and modeled to prevent the damage accumulation.

2.1.3.3. Material ratcheting behavior

The accumulation of strain caused by ratcheting occurs progressively in one direction (tension or compression direction). The term “strain accumulation” means an increase in plastic strain by an additional

increment of plastic strain in one direction. The accumulation of plastic strain is accelerated by two processes: (1) an increase in cyclic plastic strain as a result of cyclic softening and (2) higher mean tensile strain level. Similarly, a compressive mean stress can enhance buckling. Ratcheting can occur even without tension or compressive mean stress, in material that exhibit yield anisotropy between tension and compression.

The uniaxial stress-controlled fatigue test is widely used to evaluate material ratcheting. Material ratcheting behavior is characterized by a constant stress condition with a prescribed cyclic stress load. Material ratcheting behavior under uniaxial cyclic loading is schematically illustrated in Figure 2.5 [11]. The strain response under constant stress-controlled conditions is composed of an elastic component, $\epsilon_e = \sigma_{\max}/E$, and a plastic component, ϵ_p . With continued cyclic stress, plastic strain accumulation occurs at a high rate in the early stage (also called the primary region). After the primary region, the rate of plastic strain accumulation saturates and become steady, $\epsilon_N = d\epsilon/dN$; that region is called secondary or steady-state region. At a late stage, final fracture occurs after the strain rate rapidly increases. The last stage is also called the tertiary region. In Figure 2.5, the strain-cycle plot is similar to strain-time plot in conventional creep testing. Hence, ratcheting is widely called

cyclic creep although ratcheting is unlike creep a time-independent phenomenon.

The rate of plastic strain accumulation decreases with the number of loading cycles after primary region, a phenomenon referred to as ratcheting decay. Ratcheting decay is widely observed in most metals. Jiang studied the ratcheting decay rate in several metallic materials under constant loading and showed that relationship between the decay rate and number of cycles is given by a power-law expression. However, Hassan et al. showed that the ratcheting rate is clearly increasing even in the secondary stage, contrary to the behavior of ratcheting decay [10]. He confirmed experimentally that cyclic softening in metallic materials accelerated ratcheting and performed complementary test to confirm the effect of cyclic softening on ratcheting.

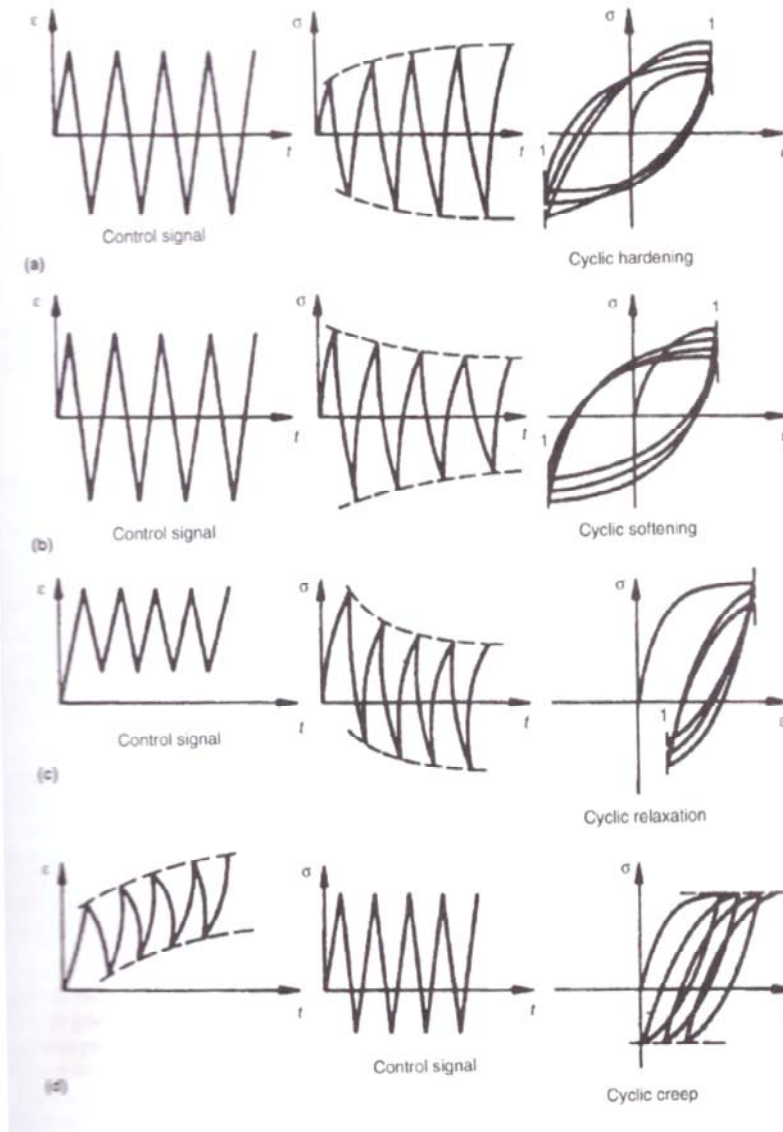


Figure 2.1. Schematic diagram of cyclic hardening and softening behavior [6].

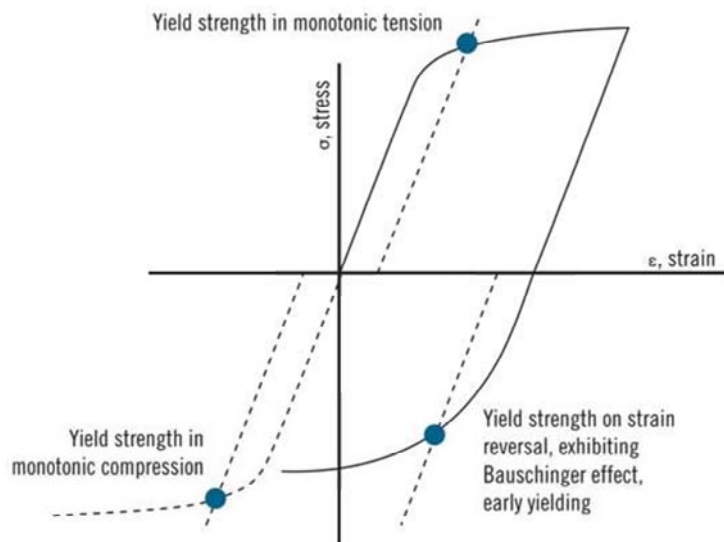


Figure 2.2 Schematic diagram of Bauschinger effect

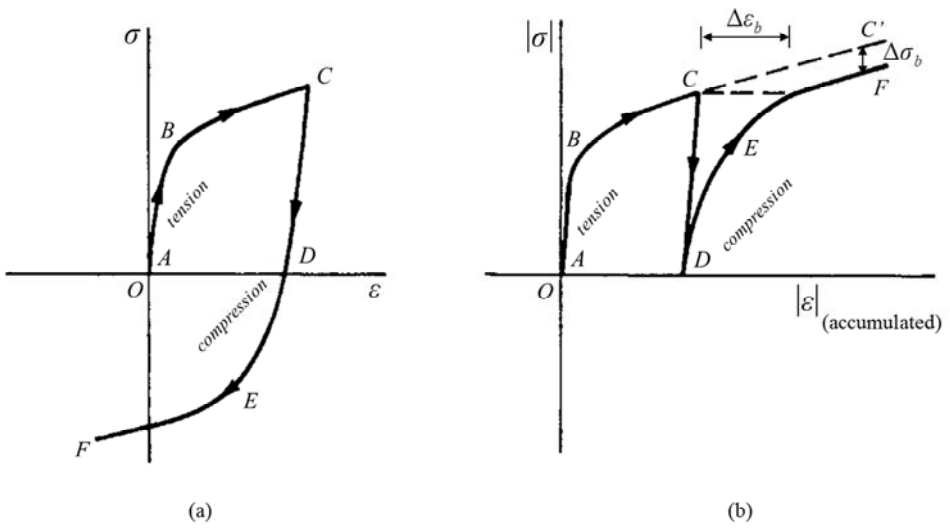


Figure 2.3. Schematic of stress-strain curve for fully reversed loading and replotting curve [8].

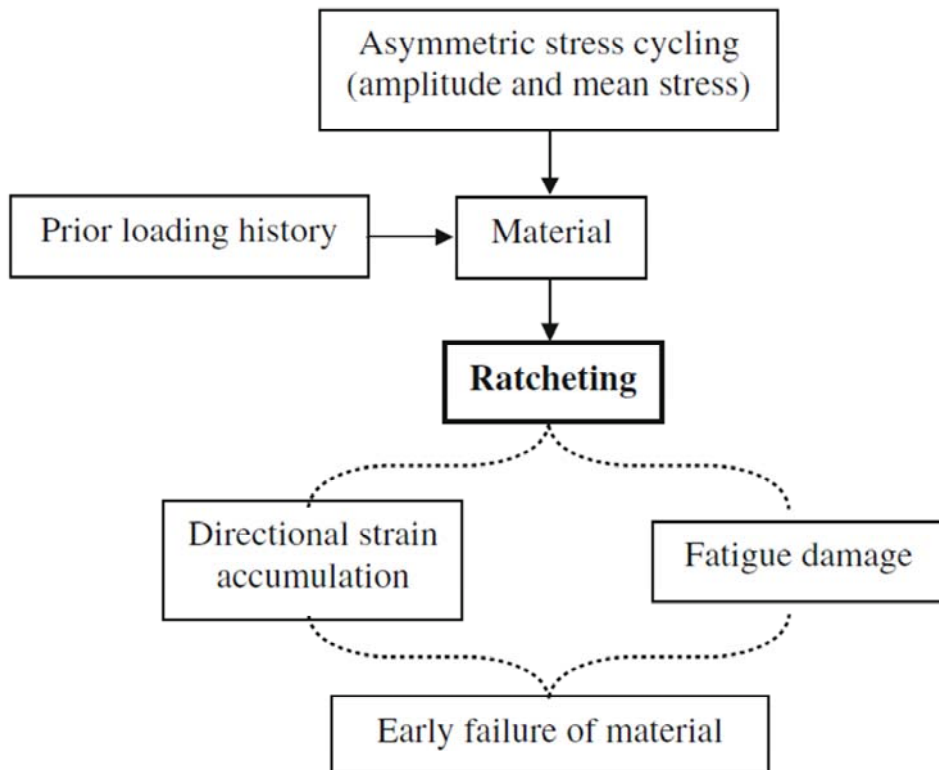


Figure 2.4. Block diagram of ratcheting [9].

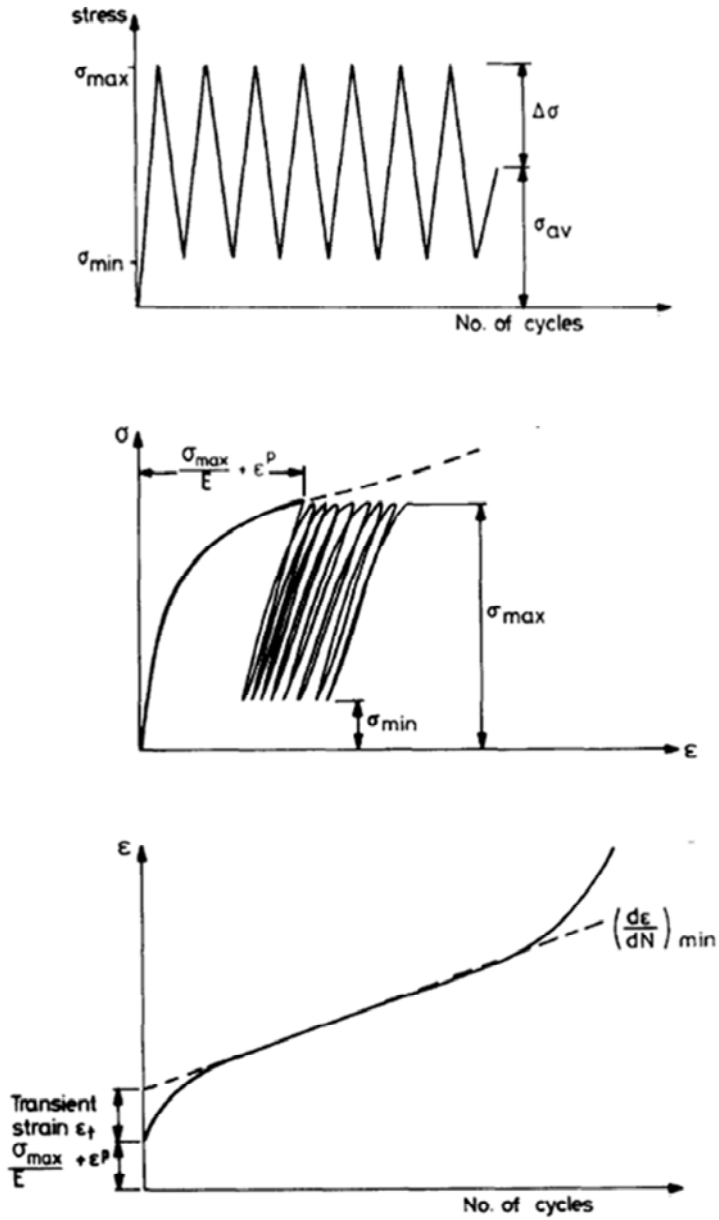


Figure 2.5 Illustration of material ratchetting phenomenon [11].

2.2. Fracture mechanics

2.2.1. Stress analysis of crack

2.2.1.1. Crack Tip Stress Analysis

There are three mode of loading that a crack is induced. In Mode I loading mode, the principle load is applied normal to the crack plane. The two fracture surfaces are displaced perpendicular to each other in opposite directions. Mode II corresponds to in-plane shear loading and tends to slide one crack face with respect to the other. Mode III refers to out-of-plane shear. A cracked body can be loaded in any one of these modes, or a combination of two or three modes.

Westergaad [15] and Irwin [16] developed analytically the crack tip stress field for a linear elastic isotropic material subjected to the three modes of deformation, and they are listed in Table 2.1.

2.1.2.2. Effect of Constraint on Fracture Toughness

Of the three primary factors that affect the fracture toughness of a given material; that is, temperature, loading rate, and constraint, the effect of constraint is the most difficult to establish quantitatively. The primary definition of constraint deals with the plane strain to plane stress transition as defined by specimen thickness. Plane strain refers to maximum constraint and occurs in very thick test specimens that have deep cracks. In contrast, plane stress refers to minimum constraint and occurs in thin test specimens.

Ahead of sharp crack, the lateral constraint which increases with increasing specimen thickness is such that through-thickness stresses are present. Because these through-thickness stresses must be zero at each surface of a specimen, they are less for thin specimens compared with thick them. For very thick specimens, the through-thickness stresses at the centerline are large, and a triaxial tensile state of stress occurs ahead of the crack. This triaxial state of stress reduces the apparent ductility of the material by decreasing the shear stresses. Because yielding is restricted, the constraint ahead of the crack is increased and thus the fracture toughness is reduced. This decrease in fracture toughness is

controlled by the thickness of the specimen, even though the inherent metallurgical properties of the material may be unchanged. Thus, the fracture toughness is smaller for thick specimens compared with thinner specimens of the same material. This behavior is shown schematically in figure 2.6 [17], which indicates that the minimum fracture toughness of a particular material, K_{IC} , is reached when the thickness of the specimen is large enough so that the state of stress is plane strain.

To demonstrate the significant constraint effect on the fracture behavior of a given material, it can be consider a point on the crack plane just ahead of the crack tip. According to Table 2.1, the stresses in the x and y direction a point on the crack plane ($\theta = 0$) for Mode I are equal:

$$\sigma_x = \sigma_y = \frac{K_I}{\sqrt{2\pi r}} \quad (2-1)$$

when $\theta = 0$ under linear elastic conditions, the shear stress is zero, which means that the crack plane is a principal plane for pure Mode I loading. If the stress state is the plane stress, $\sigma_z = 0$ by definition. Under plane strain conditions, $\sigma_z = 2\nu\sigma_y$. Substituting these stresses into the von Mises yield criterion leads to the following:

$$\sigma_y = \sigma_{ys} \quad (\text{plane stress}) \quad (2-2)$$

$$\sigma_y = 2.5\sigma_{ys} \quad (\text{plane strain}), \quad (2-3)$$

assuming $\nu = 0.3$. Therefore, the triaxial stress state associated with plane strain leads to higher stresses in the plastic zone. For fracture mechanisms that are governed by normal stress, such as cleavage in metals, the material will behave in a more brittle fashion when subjected to a triaxial stress state. Triaxial stresses also assist ductile fracture process such as microvoid coalescence.

Pellini [18] described the physical significance of constraint and plate thickness on fracture toughness in terms of plastic flow, as shown in figure 2.7. This figure shows that the introduction of a circular notch in a bar loaded in tension causes an elevation of the stress-strain curve. The plastic flow of the smooth tensile bar, which is usually used to develop conventional stress-strain curves, is free flow because lateral contraction is not constrained during initial loading. In the notched bar, however, the reduced section deforms inelastically while the ends of the specimen are still loaded elastically. Since the amount of elastic contraction is small compared to the inelastic contraction of reduced section, a restriction to plastic flow is developed. This restriction is in the nature of a reaction-

stress system such that the σ_x and σ_y stresses restrict or constrain the flow in the σ_y direction. Thus, the uniaxial stress state of the smooth bar is changed to a triaxial tensile stress system in the notched bar compared with the unnotched bar. As the notch becomes far sharper, the severity of the stress state increases.

2.2.2. Fracture Toughness Parameters

The fracture toughness of a material measures its ability to resist crack initiation and propagation. Several fracture toughness parameters available, including critical stress intensity factor, the critical value of the J integral, and the critical crack tip opening displacement.

1) Stress Intensity Factor

Irwin [16] confirmed that the stresses in the vicinity of a crack tip take the form as following:

$$\sigma_{ij} = \frac{K}{\sqrt{2\pi r}} f_{ij}(\theta) + \dots, \quad (2-4)$$

where r, θ are the cylindrical polar coordinates of a point with respect to the crack tip. K is a quantity which gives the magnitude of the elastic stress field. It is called the stress intensity factor. Dimensional analysis shows that K must be linearly related to stress and directly related to the square root of a characteristic length. Eq. (2-1) from Griffith analysis indicates that this characteristic length is the crack length, and it turns out that the general form of the stress intensity factor is given by:

$$K = \sigma \sqrt{\pi a} \cdot f(a/W), \quad (2-5)$$

where $f(a/w)$ is a dimensionless parameter that depends on the geometries of the specimen and crack, and σ is the applied stress.

It is customary to write the limiting value of K for maximum constraint, *i.e.* plane strain, in Mode I fracture as K_{IC} . K_{IC} can be considered a material property characterizing the crack resistance, and is therefore called the plane strain fracture toughness. Thus the same value of K_{IC} should be found by testing specimen of the same material with different geometries and with critical combinations of crack size and shape and fracture stress.

2) Crack Tip Opening Displacement

Wells [90] focuses on the strains in the crack tip region instead of the stresses. He noticed that the crack faces moved apart prior to fracture; In the presence of the plasticity, an initial sharp crack was blunted. The degree of crack blunting increased in proportion to the toughness of the material, as illustrated in figure 2.8. Therefore, Wells [90] proposed to use the crack flank displacement at the tip of a blunting crack, the well-known the Crack Tip Opening Displacement (CTOD) as a measure of fracture toughness parameter.

There are a number of alternative definitions of CTOD. The two most common definitions are the displacement at the original crack tip and the 90° intercept, as shown in Figure 2.9. These two definitions are equivalent if the crack blunts in a semicircle.

CTOD can be considered as a strain-based estimate of fracture toughness. However, it can be separated into elastic and plastic components, which is displayed in Eq. (2-6).

$$\delta = \delta_{el} + \delta_p. \quad (2-6)$$

The subscripts *el* and *p* denote elastic and plastic components, respectively. The elastic part of CTOD is derived from the stress intensity factor computed by the load and specimen dimensions, *K*. In some

standards, the plastic component of CTOD is obtained by assuming that the specimen rotates about a plastic hinge like in figure 2.9 [19]. The plastic component is derived from the crack mouth opening displacement which measured using a clip gauge. The position of the plastic hinge is given in test standards for each specimen type.

3) J-Integral

The fracture parameter J -integral proposed by Rice [20] means a contour integral that can be evaluated along any arbitrary path enclosing the crack tip, as illustrated in figure 2.10. Rice [20] considered the potential energy changes involved in crack growth in non-linear elastic material. Such non-linear elastic behavior is a realistic approximation for plastic behavior provided no unloading occurs in any part of the material. From these concepts, Rice derived J -integral. J is derived from the Eq. (2-7):

$$J = \int_r \left(w dy - T_i \frac{\partial u_i}{\partial x} ds \right), \quad (2-7)$$

where w is the strain energy density and s is distance along the arbitrary path, Γ , around the crack tip. T_i and u_i are the component of the traction vector and the displacement vector, respectively.

He also showed that J to be equal to the energy release rate for a crack in an elastic-plastic material, analogous to G for linear elastic material [20]. J is more general version of the energy release rate and for the special case of a linear elastic material only, J is identical to G . The energy release rate is generally defined as the potential energy that is released from a structure when the crack grows in an elastic material. However, much of the strain energy absorbed by an elastic-plastic material is not recovered when the crack grows or the specimen is unloaded; a growing crack in an elastic-plastic material leaves a plastic wake. Thus the energy release rate concept has a somewhat different interpretation for elastic-plastic materials. Consequently, the energy release rate of J is useful for elastic-plastic materials when applying in appropriate manner.

4) Relationship among fracture parameters

For linear elastic condition, the J -integral is identical to G which is the energy release rate per unit crack extension. Therefore, it is possible to convert "equivalent" K_{IC} values from J and $CTOD$ by using the relationships among three fracture toughness parameters. Under plane strain linear elastic conditions,

$$J_{IC} = G_{IC} = \frac{(1-\nu^2)K_{IC}^2}{E} \quad (2-8)$$

The $CTOD$ parameter, δ , also is related to J as follows:

$$\delta = \frac{G}{m\sigma_{ys}} = \frac{K_{IC}^2}{m\sigma_{ys}E}, \quad (2-9)$$

where m is a dimensionless constant that depends on the stress state and material properties, $1 \leq m \leq 2$. By Eq. (2-9) and (2-10), the fracture toughness can be expressed in terms of any one of the three parameters based on the relationships shown below:

- a) For small scale yielding, an equivalent K_{IC} , denoted as K_{JC} , can be computed as follow:

$$K_{JC} = \sqrt{\frac{J_{IC} \cdot E}{1 - \nu^2}} \quad (2-10)$$

b) An approximate relationship between the J-integral and CTOD is given by:

$$J_{IC} = m \cdot \sigma_{ys} \cdot \delta_{IC} \quad (2-11)$$

c) By combining the above equations, the equivalent value computed from CTOD data is given by:

$$K_{JC} = \sqrt{\frac{m \cdot \sigma_{ys} \cdot \delta_{IC} \cdot E}{1 - \nu^2}} \quad (2-12)$$

Table 2.1 Stress and displacement fields ahead of crack tip for each Mode [15,16]

	Mode I	Mode II	Mode III
σ_{xx}	$\frac{K_I}{\sqrt{2\pi r}} \cos\left(\frac{\theta}{2}\right) \left[1 - \sin\left(\frac{\theta}{2}\right) \sin\left(\frac{3\theta}{2}\right)\right]$	$\frac{K_{II}}{\sqrt{2\pi r}} \sin\left(\frac{\theta}{2}\right) \left[2 + \cos\left(\frac{\theta}{2}\right) \cos\left(\frac{3\theta}{2}\right)\right]$	-
σ_{yy}	$\frac{K_I}{\sqrt{2\pi r}} \cos\left(\frac{\theta}{2}\right) \left[1 + \sin\left(\frac{\theta}{2}\right) \sin\left(\frac{3\theta}{2}\right)\right]$	$\frac{K_{II}}{\sqrt{2\pi r}} \sin\left(\frac{\theta}{2}\right) \cos\left(\frac{\theta}{2}\right) \cos\left(\frac{3\theta}{2}\right)$	-
σ_{zz}	0 (plane stress) $\nu(\sigma_{xx} + \sigma_{yy})$ (plane strain)	0 (plane stress) $\nu(\sigma_{xx} + \sigma_{yy})$ (plane strain)	-
τ_{xy}	$\frac{K_I}{\sqrt{2\pi r}} \cos\left(\frac{\theta}{2}\right) \sin\left(\frac{\theta}{2}\right) \cos\left(\frac{3\theta}{2}\right)$	$\frac{K_{II}}{\sqrt{2\pi r}} \cos\left(\frac{\theta}{2}\right) \left[1 - \sin\left(\frac{\theta}{2}\right) \sin\left(\frac{3\theta}{2}\right)\right]$	-
τ_{yz}	0	0	$\frac{K_{III}}{\sqrt{2\pi r}} \cos\left(\frac{\theta}{2}\right)$
τ_{xz}	0	0	$-\frac{K_{III}}{\sqrt{2\pi r}} \sin\left(\frac{\theta}{2}\right)$
u_x	$\frac{K_I}{2\mu} \sqrt{\frac{r}{2\pi}} \cos\left(\frac{\theta}{2}\right) \left[\kappa - 1 + 2 \sin^2\left(\frac{\theta}{2}\right)\right]$	$\frac{K_{II}}{2\mu} \sqrt{\frac{r}{2\pi}} \sin\left(\frac{\theta}{2}\right) \left[\kappa + 1 + 2 \cos^2\left(\frac{\theta}{2}\right)\right]$	-
u_y	$\frac{K_I}{2\mu} \sqrt{\frac{r}{2\pi}} \sin\left(\frac{\theta}{2}\right) \left[\kappa + 1 - 2 \cos^2\left(\frac{\theta}{2}\right)\right]$	$-\frac{K_{II}}{2\mu} \sqrt{\frac{r}{2\pi}} \cos\left(\frac{\theta}{2}\right) \left[\kappa - 1 - 2 \sin^2\left(\frac{\theta}{2}\right)\right]$	-
u_z	-	-	$\frac{2K_{III}}{\mu} \sqrt{\frac{r}{2\pi}} \sin\left(\frac{\theta}{2}\right)$

Note: ν is Poisson's ratio and μ is the shear modulus. $\kappa = 3 - 4\nu$ (plane strain) and $\kappa = (3 - \nu) / (1 + \nu)$ (plane stress).

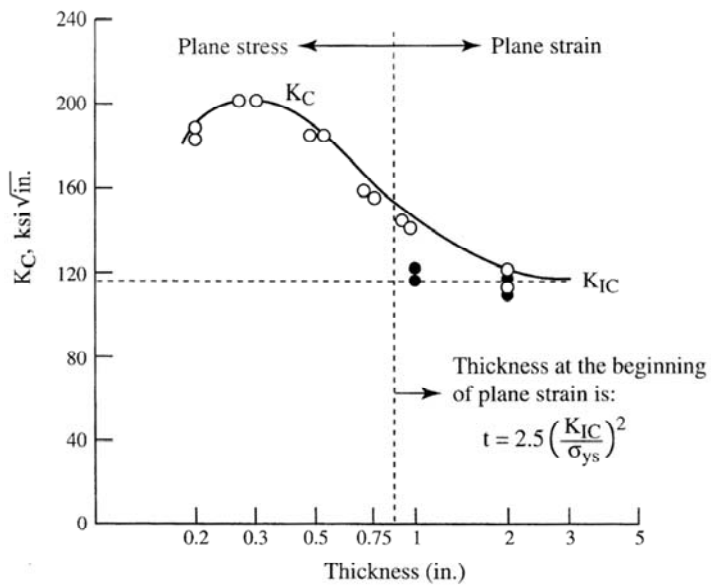


Figure 2.6. Effect of thickness on K_C behavior [17].

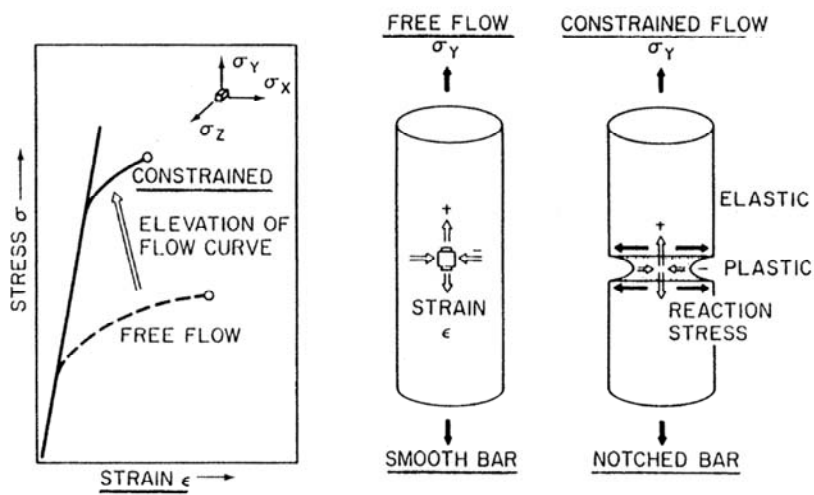


Figure 2.7. Constraint to plastic flow caused by notched geometries [17].

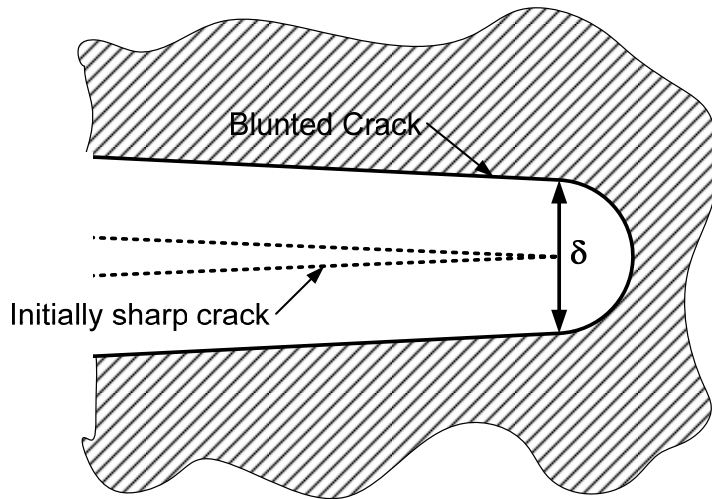


Figure 2.8. Crack tip opening displacement (CTOD). An initially sharp crack blunts with plastic deformation, resulting in a finite displacement, δ , at the crack tip [19].

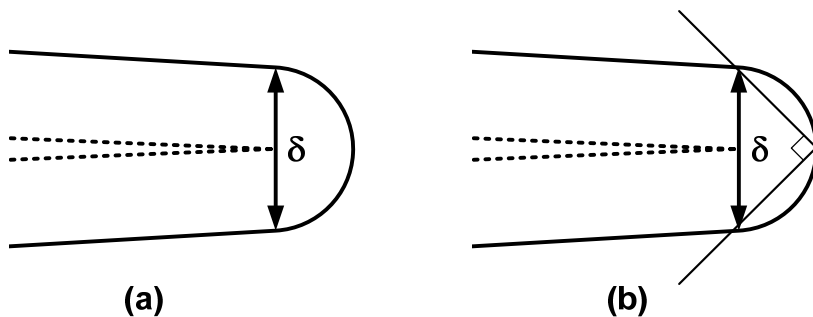


Figure 2.9. Alternative definitions of CTOD: (a) displacement at the original crack tip and (b) displacement at the intersection of a 90° vertex with the crack flanks [19].

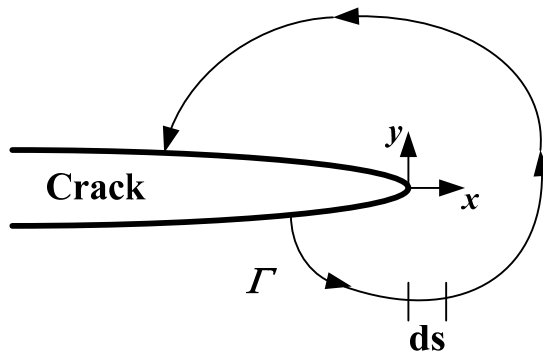


Figure 2.10. Arbitrary contour around the tip of a crack [20].

2.2.3. Equivalence of Fracture Mechanics and Contact Mechanics

2.2.3.1. Contact mechanics in flat punch indentation

(1) Elastic models

Sneddon [29] derived load and displacement relationship for axisymmetric punch indentation. He proposed a solution for the indentation of an elastic half-space by a flat-ended cylindrical punch indenter (also called flat punch indenter). A schematic diagram of flat punch indentation is shown in Figure 2.11. The contact area is assumed to be circular and equal to the indenter tip area. The mean contact pressure P_m corresponding to an indentation penetration depth h is defined as follows:

$$P_m = \frac{2Eh}{\pi a(1-\nu^2)} \quad (2-13)$$

where E is elastic modulus, a is contact radius and ν is Poisson's ratio. Equation (2-13) shows that relationship between the mean contact pressure and the indentation depth is linear because of constant contact area. The pressure distribution beneath the flat punch indenter is given by:

$$\sigma_z(r,0) = \frac{P_m}{2\sqrt{1-r^2/a^2}} \quad (2-14)$$

(2) Elastic-plastic models

Two models has been proposed to describe the stress-strain field in a material subjected to indentation with different indenter: the spherical cavity [23] and the slip-line model [24]. The spherical cavity model was developed by consideration of a spherical and conical indenter and assumes that the plastic zone beneath the indenters has spherical symmetry. However, this model is too coarse to be applied to a cylindrical indentation because the plastic zone does not remain shape of spherical with depth penetration [25, 26].

The slip-line model can be used to describe the stress-strain field under rigid plastic condition, so that this model considers plastic deformation only. Shield [27] showed that the axisymmetric plastic flow of a rigid plastic material can be described by a slip-line field. He described the plastic stress field of a semi-infinite solid in flat-ended cylindrical indentation. Afterward, Eason and Shield [28] also studied the indentation stress field of a semi-infinite solid in terms of depth and size of plastic zone; their results indicated that plasticity extends to the

indenter and specimen axis when the mean contact pressure is about six times the shear strength, and the mean contact pressure is about three times the uniaxial tensile yield stress.

2.2.3.2. Equivalence with fracture mechanics

Sneddon [29] found the elastic solution for a normally loaded axisymmetric rigid punch of circular contact radius a , shown in Figure 2.25. It is shown in this section that the stress fields of the contact problem are the same as those in the semi-infinite circumferential crack in a right circular, cylindrical rod (Figure 2.12).

With cylindrical coordinates, r, z, φ , in Figure 2.12, the non-zero stresses are [24]

$$\begin{pmatrix} \sigma_{zz} \\ \sigma_{rz} \\ \sigma_{rr} \\ \sigma_{\varphi\varphi} \end{pmatrix} \rightarrow -\frac{P}{2\pi a^2 \sqrt{2s}} \cos \frac{\varphi}{2} \begin{pmatrix} 1 + \sin \frac{\varphi}{2} \sin \frac{3\varphi}{2} \\ \sin \frac{\varphi}{2} \cos \frac{3\varphi}{2} \\ 1 - \sin \frac{\varphi}{2} \sin \frac{3\varphi}{2} \\ 2\nu \end{pmatrix} \quad (2-15)$$

Therefore, all stresses are square root singular with respect to σ , the local radial coordinate of the “crack analogue” (Figure 2.13).

To calculate the Mode I stress intensity factor, we note that the contact pressure gives the only non-zero stress at the surface,

$$\sigma_{zz} = -\frac{P}{2\pi a\sqrt{a^2 - r^2}} \quad (2-16)$$

The first of Eq. (2-51) is the correct asymptote of Eq. (2-52) as $r \rightarrow a$ - . From

$$\sigma_{zz} = -\frac{K_I}{\sqrt{2\pi(a - r)}} \quad (2-17)$$

we readily conclude that

$$K_I = -\frac{P}{2a\sqrt{\pi a}} \quad (2-18)$$

This result is the same as that in [30-32] for a circular semi-infinite crack located along the circumference of a cylindrical rod (with an uncracked ligament of radius a) loaded remotely with a concentrated normal load P , Figure 2.13. Eq. (2-18) also provide stress distributions that are identical to those for the fields ahead of a circumferentially located crack in a cylindrical rod (where the crack depth \gg uncracked ligament radius).

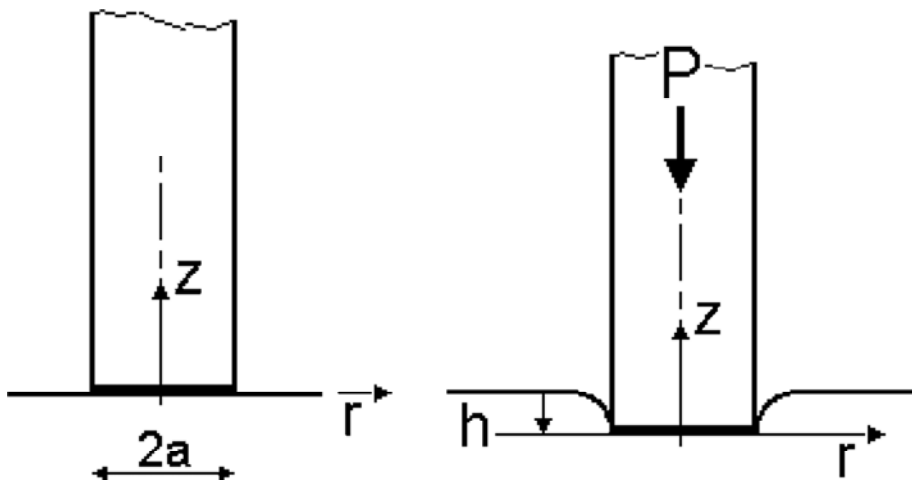


Figure 2.11. Schematic of flat punch indentation.

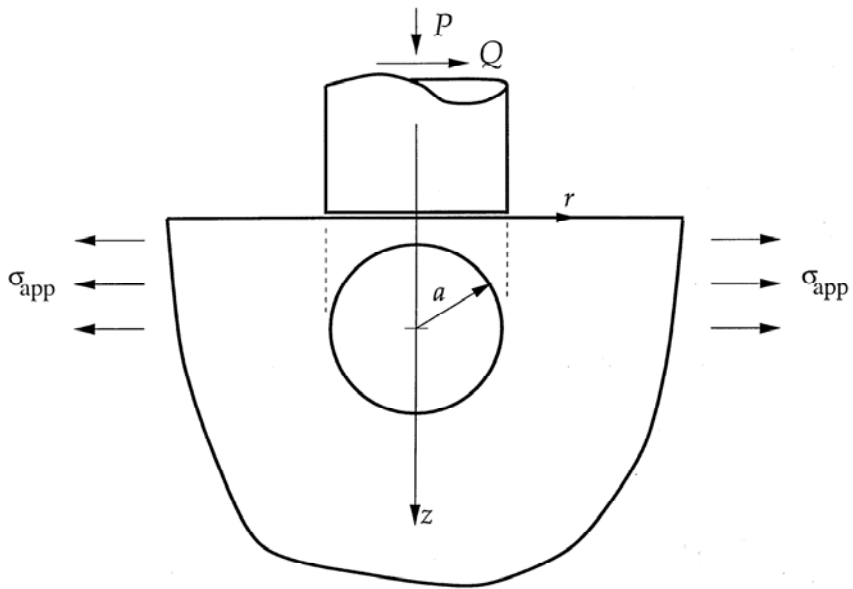


Figure 2.12. A schematic representation of the contact between the end of a right-circular cylindrical punch and a substrate [29].

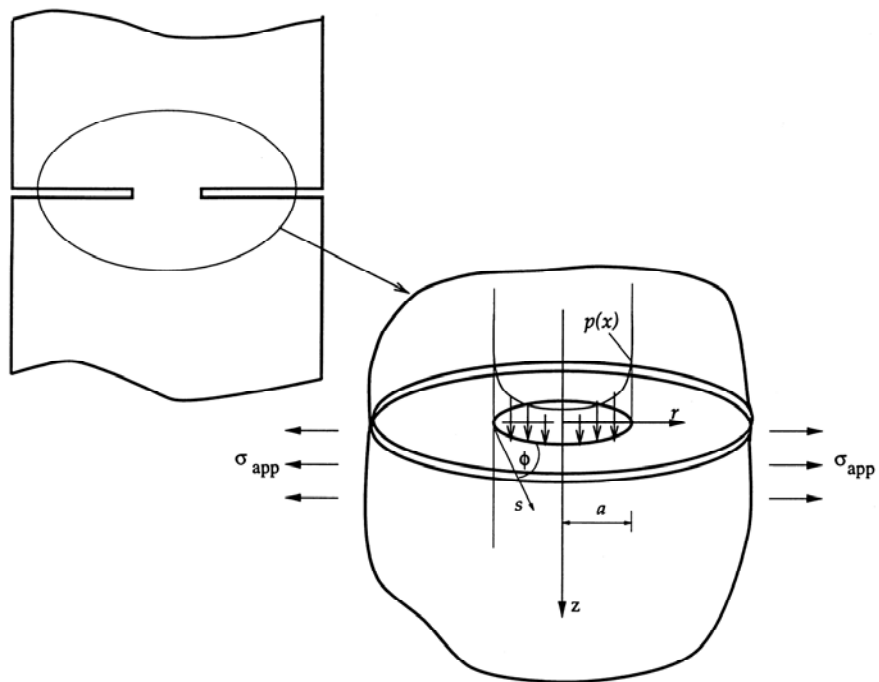


Figure 2.13. Crack analogue of Figure 2.25 showing the circumferentially cracked cylindrical rod specimen, and the associated nomenclature [29].

2.3. Instrumented indentation testing

2.3.1. Introduction and application

2.3.1.1. Introduction

Instrumented indentation technique is derived from the conventional hardness test. Conventional hardness testing only measures hardness from residual indent size, which means the deformation resistance for the material to penetration. However, instrumented indentation testing measures the applied load and the depth of penetration of an indenter into the specimen simultaneously and the area of contact are determined indirectly from indentation load-depth curve. Elastic modulus of the specimen can be evaluated from the indentation load-depth curve. [33-35]. The other mechanical properties such as the yield strength, tensile strength, strain hardening exponent [48, 49], fracture toughness [60-64], and residual stress [50-54] can also be obtained from the indentation curve.

Instrumented indentation technique commonly have four merits; 1) it is very simple, 2) it can be applied to local area such as weld zone, thin

film and individual grain/grain boundary using micro or nanoindentation, 3) it is cost effective since specific specimen requirement is not needed and 4) it can be applied nondestructively in a macroscale, which on-site testing becomes available.

Instrumented indentation test can be divided into three categories according to the applied load range: macro, micro, and nano. A macro-indentation is mainly applied to the safety assessment of an in-service component due to its nondestructive nature. Micro or nanoindentation is one of the most powerful tools for evaluating material properties and deformation behavior at small scales as thin films, MEMS.

Over the past decade, instrumented indentation test have been standardized all over the world. The ISO 14577-1 [65] specifies not only the method of instrumented indentation test for hardness and material parameter, but the method of verification and calibration of testing machine. The part of ISO 14577-4 [66] is particularly suitable for testing in the micro/nano range applicable to thin coatings is also under discussion. In addition, a new ISO technical report, TR 29381:2008[67], was standardized in 2008. The technical report describes the method for determining the tensile properties and residual stress of metallic materials using instrumented indentation tests.

2.3.1.2. Application

2.3.1.2.1. Hardness and Elastic Modulus

A schematic diagram of an indentation load-depth curve with a sharp indenter such as Vickers and Berkovich indenter is shown in Figure 2.14, where the parameter P designates the load and h the displacement relative to the initial un-deformed surface. For modeling purposes, deformation during loading is assumed to be both elastic and plastic in nature as the permanent hardness impression forms. During unloading, it is assumed that only the elastic displacements are recovered; it is the elastic nature of the unloading curve that facilitates the analysis. For this reason, the method does not apply to materials in which plasticity reverses during unloading. However, finite element simulations have shown that reverse plastic deformation is usually negligible [68]. There are three important quantities that must be measured from the P - h curves: the maximum load, P_{max} , the maximum displacement, h_{max} , and the elastic unloading stiffness, $S=dP/dh$, defined as the slope of the upper portion of the unloading curve during the initial stages of unloading (also called the contact stiffness). The accuracy of hardness and modulus measurement depends inherently

on how well these parameters can be measured experimentally. Another important quantity is the final depth, h_f , the permanent depth of penetration after the indenter is fully unloaded. The analysis used to determine the hardness, H , and elastic modulus, E , is essentially an extension of the method proposed by Doerner and Nix [33] that accounts for the fact that unloading curves are distinctly curved in a manner that cannot be accounted for by the flat punch approximation. In the flat punch approximation used by Doerner and Nix [33], the contact area remains constant as the indenter is withdrawn, and the resulting unloading curve is linear. In contrast, experiments have shown that unloading curves are distinctly curved and usually well approximated by the power law relation

$$P = \alpha(h - h_f)^m, \quad (2-19)$$

where α and m are power law fitting constants [34]. The exact procedure used to measure H and E is based on the unloading processes in which it is assumed that the behavior of the Berkovich indenter can be modeled by a conical indenter with a half-included angle, θ , that gives the same depth-to-area relationship, $\theta = 70.3^\circ$. The basic assumption is that the contact periphery sinks-in in a manner that can be described by models

for indentation of a flat elastic half-space by rigid punches of simple geometry. This assumption limits the applicability of the method since it does not account for the pile-up of material at the contact periphery that occurs in some elastic-plastic materials. Assuming, however, that pile-up is negligible, the elastic models show that the amount of sink-in, h_d , is given by

$$h_d = \omega \frac{P_{max}}{S}, \quad (2-20)$$

where ω is a constant that depends on the geometry of the indenter. Important values are: $\omega = 0.72$ for a conical punch, $\omega = 0.75$ for a parabolic of revolution (which approximates to a sphere at small depths), and $\omega = 1.00$ for a flat punch [29].

Using Eq. (2-20) to approximate the vertical displacement of the contact periphery, the depth along which contact is made between the indenter and the specimen, $h_c = h_{max} - h_d$, is

$$h_c = h_{max} - \varepsilon \frac{P_{max}}{S}. \quad (2-21)$$

Letting $F(d)$ be an area function that describes the projected (or cross-sectional) area of the indenter at a distance d back from its tip, the contact area A is then

$$A = F(h_c) \quad (2-22)$$

The area function, also sometimes called the indenter shape function, must be carefully calibrated by independent measurements so that deviations from non-ideal indenter geometry are taken into account. These deviations can be quite severe near the tip of the Berkovich indenter, where some rounding inevitably occurs during the grinding process.

Once the contact area is determined, the hardness is estimated from

$$H = \frac{P_{\max}}{A} . \quad (2-23)$$

Note that because this definition of hardness is based on the contact area under load, it may deviate from the traditional hardness measured from the area of the residual hardness impression if there is significant elastic recovery during unloading. However, this is generally important only in materials with extremely small values of E/H [52]. Measurement of the elastic modulus follows from its relationship to contact area and the measured unloading stiffness through the relation

$$S = \beta \frac{2}{\sqrt{\pi}} E_r \sqrt{A} , \quad (2-24)$$

where E_r is the reduced modulus as in the Eq. (2-24). The effective elastic modulus takes into account the fact that elastic displacements occur in both the specimen, with Young's modulus E and Poisson's ratio ν , and the indenter, with elastic constants E_i and ν_i . Note that Eq. (2-24) is a very general relation that applies to any axisymmetric indenter. It is not limited to a specific simple geometry, even though it is often associated with flat punch indentation. Although originally derived for elastic contact only, it has subsequently been shown to apply equally well to elastic-plastic contact, and that small perturbations from pure axisymmetric geometry do not affect it either. It is also unaffected by pile-up and sink-in.

2.3.2.1.2. Indentation Tensile Properties

The procedure for evaluating the tensile properties involves four steps, as illustrated in figure 2.15: step 1- determination of the contact area, step 2 -definition of the true stress and strain, step 3 - fitting to the constitutive equation, and step 4 - evaluation of the tensile properties [67]. Partial repetition of the load-removal procedure is performed fifteen times before step 1. Three important parameters must be obtained from each

partial loading-unloading curve: the maximum load, L_{max} ; the maximum depth, h_{max} ; and the elastic unloading stiffness, S , which is defined as the slope of the upper portion of the unloading curve during the initial stage of unloading (also called the contact stiffness), as illustrated in figure 2.15. Determination of the exact contact depth is important for determining the contact area. During spherical indentation testing, materials exhibit two types of response: elastic deflection and plastic pile-up. Oliver and Pharr defined elastic deflection h_d as [34]:

$$h_d = w \frac{L_{max}}{S} \quad (2-25)$$

where w is a constant that depends on the geometry of the indenter ($w=0.75$ for a spherical indenter) [34]. The other response is the plastic pile-up behavior, which depends on the work-hardening exponent n and h_{max}/R [36]:

$$h_{pile} = f\left(n, \frac{h_{max}}{R}\right) \quad (2-26)$$

where h_{pile} is the plastic pile-up height and R is the indenter radius. From Eqs. (2-25) and (2-26), the contact depth (h_c) can be obtained as:

$$h_c = h_{max} - h_d + h_{pile} \quad (2-27)$$

After the contact depth is determined, the contact area, A_c , can be calculated from the relationship between the contact area and contact depth:

$$A_c = \pi(2Rh_c - h_c^2) \quad (2-28)$$

In step 2, the uniaxial true stress is determined from the maximum load, L_{max} , and the contact area, A_c . According to Tabor's approach [36], the mean indentation pressure has the following linear relationship with the uniaxial true stress:

$$\sigma_r = \frac{p_m}{\psi} = \frac{1}{\psi} \frac{L}{A_c} \quad (2-29)$$

where σ_r is the true stress obtained from the indentation, p_m is the mean indentation pressure and is a plastic constraint factor. Eq. (2-23) is widely used in indentation research, and there are various definitions of the value of the plastic constraint factor. The uniaxial true strain is determined from the geometric parameter a/R based on the deformation shape and the strain distribution under a spherical indenter:

$$\varepsilon_r = f(a/R) \quad (2-30)$$

where a is the contact radius and R is the indenter radius. In step 3, the true stress and strain obtained by instrumented indentation testing are fitted using two constitutive equations:

$$\sigma = K\varepsilon^n \quad (2-31)$$

$$\sigma = A + E_T\varepsilon \quad (2-32)$$

where K is the strength coefficient, n is the strain-hardening exponent and E_T is the tangential modulus of the material. Eq. (31) is used for common metals that show power-law hardening, while Eq. (32) is used for austenitic materials, such as stainless steel, that show linear hardening. In step 4, the tensile properties are determined. The elastic modulus is measured from the indentation load-depth curve to determine the yield strength. Oliver and Pharr [34] expressed the elastic modulus as a function of contact stiffness and contact area as follows:

$$E_r = \frac{\sqrt{\pi}}{2} \frac{S}{\sqrt{A_c}} \quad (33)$$

where E_r is the reduced elastic modulus measured from indentation, S is the contact stiffness and A_c is the contact area. The yield strength is determined as the interception of the fitted stress-strain curve and the

linear curve with the slope of the elastic modulus of 0.2 offset from the origin. The strain-hardening exponent is determined from the fitting curve of the stress-strain curve. The ultimate tensile strain is the same as the strain-hardening exponent according to the theory of instability in tension. The ultimate tensile strength can be determined at the ultimate tensile strain, which is obtained from the strain-hardening exponent. Finally, we can obtain the yield strength, tensile strength and elastic modulus from indentation testing.

2.3.2.1.3. Residual Stress

Indentation hardness evaluated from the indentation $P-h$ curve changes with the residual stress. Indentation $P-h$ curves are shifted with the direction and magnitude of residual stress within the tested material. However, the variations in the apparent indentation hardness with change in residual stress have been identified as an artifact of erroneous optical measurements of the indentation imprint [50,51]. The contact hardness was found to be invariant regardless of the elastically applied stress (residual stress) [50,51]. The finite element method results showed the important role of sink-in or pile-up deformations around the contact in

the stressed state in producing the stress-insensitive contact hardness [52]. Therefore, the change in contact morphologies with residual stress was modeled for constant maximum indentation depth assuming the independence of intrinsic hardness and residual stress [53].

The change in indentation deformation caused by the residual stress was identified in the indentation loading curve in figure 2.16. The applied load in the tensile-stressed state is lower than that in the stress-free state for the same maximum indentation depth [50-52]. In other words, the maximum indentation depth desired is reached at a smaller indentation load in a tensile-stressed state because a residual-stress-induced normal load acts as an additive load to the applied load. Therefore, the residual stress can be evaluated by analyzing the residual-stress-induced normal load.

The detailed changes in contact morphology can be seen in the schematic diagram in figure 2.17. The residual stress is relaxed from a tensile-stressed state to stress-free state while maintaining the constant maximum depth, h_{max} , as the stress relaxation pushes the indenter out from the surface. The pushing force appears as an increase in the applied load ($L_T \rightarrow L_0$) and the contact depth ($h_c^T \rightarrow h_c$), because the maximum depth is held constant. The indentation load and maximum depth for the

tensile-stressed state (L_T, h_{max}) are equivalent to those in the relaxed state (L_0, h_{max}). Thus, the relationship between the two states can be expressed as

$$L_0 = L_T + L_{res} . \quad (2-34)$$

In the compressive stress state, the applied load and contact depth decrease by stress relaxation under the maximum-depth-controlled path. Furthermore, this decreasing portion of the applied load was the residual-stress-induced normal load, L_{res} . Therefore, the residual stress in a welded joint can be evaluated by dividing L_{res} by the contact area, A_c , regardless of the stress state [54]

$$\sigma_{res} = \alpha \frac{L_{res}}{A_c} \quad (2-35)$$

where α is a constant related to the stress directionality of biaxial residual stress. The biaxial stress state, in which $\sigma_y = k\sigma_x$, can be divided into a mean stress term and plastic-deformation-sensitive shear deviator term [54]

Biaxial stress

Mean stress

Deviator stress

$$\begin{pmatrix} \sigma_{res}^x & 0 & 0 \\ 0 & \sigma_{res}^y & 0 \\ 0 & 0 & 0 \end{pmatrix} = \begin{pmatrix} \frac{1+k}{3}\sigma_{res}^x & 0 & 0 \\ 0 & \frac{1+k}{3}\sigma_{res}^x & 0 \\ 0 & 0 & \frac{1+k}{3}\sigma_{res}^x \end{pmatrix} + \begin{pmatrix} \frac{2-k}{3}\sigma_{res}^x & 0 & 0 \\ 0 & \frac{2-k}{3}\sigma_{res}^x & 0 \\ 0 & 0 & -\frac{1+k}{3}\sigma_{res}^x \end{pmatrix} \quad (2-51)$$

The stress component parallel to the indentation axis in the deviator stress term directly affects the indenting plastic deformation. A residual-stress-induced normal load L_{res} can be defined from the selected deviator stress component as:

$$L_{res} = \frac{1+k}{3}\sigma_{res}A_c \quad (2-36)$$

Therefore, α in Eq. (2-36) can be taken as approximately 1.5 in the equi-biaxial stress state. In the instrumented indentation test, the contact area is determined by unloading curve analysis. By differentiation of the power-law-fitted unloading curve at maximum indentation depth, the contact depth and contact area can be calculated from the contact depth based on the geometry of the Vickers indenter as [35]:

$$A_c = 24.5h_c^2 \quad (2-37)$$

Thus, residual stress was calculated from the analyzed contact area in Eq. (2-37) and the measured load change L_{res} by the effect of residual stress in Eq. (2-36).

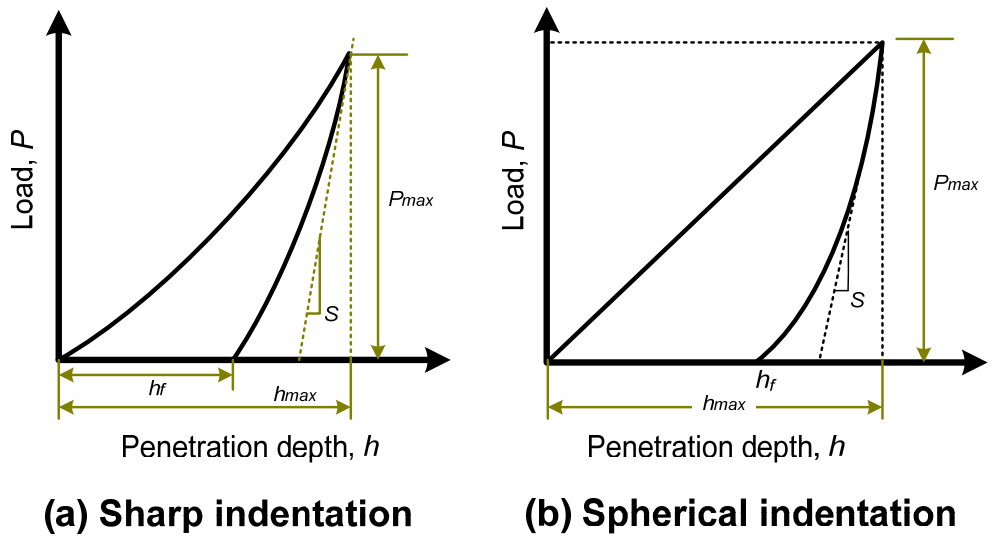


Figure 2.14. Schematic diagram of typical load-depth curve obtainable during instrumented indentations

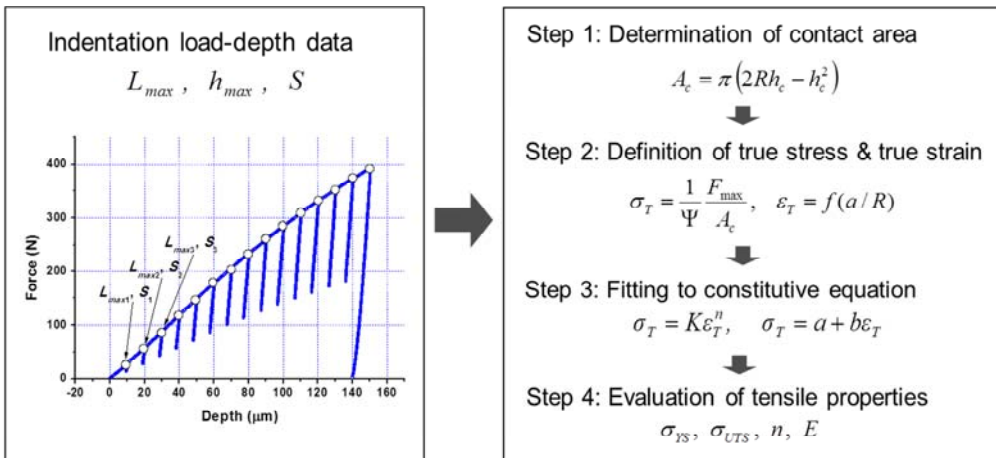


Figure 2.15. Algorithm for evaluating indentation tensile properties

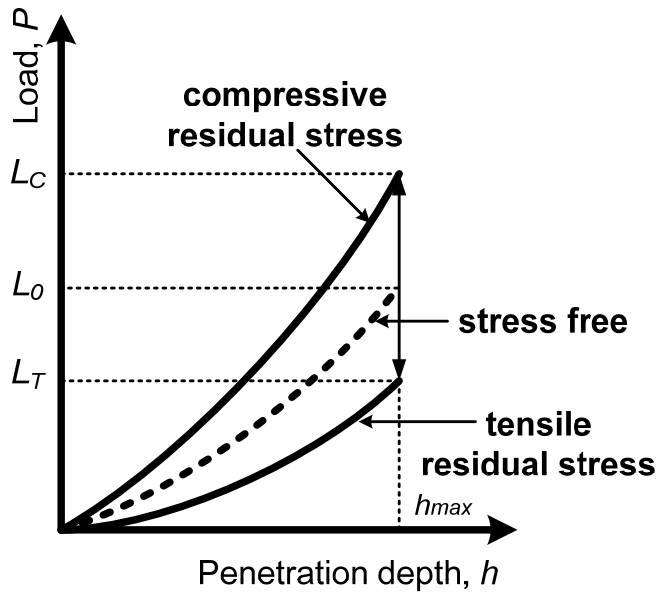


Fig. 2.16. Variation of indentation loading curves with changes in the stress state.

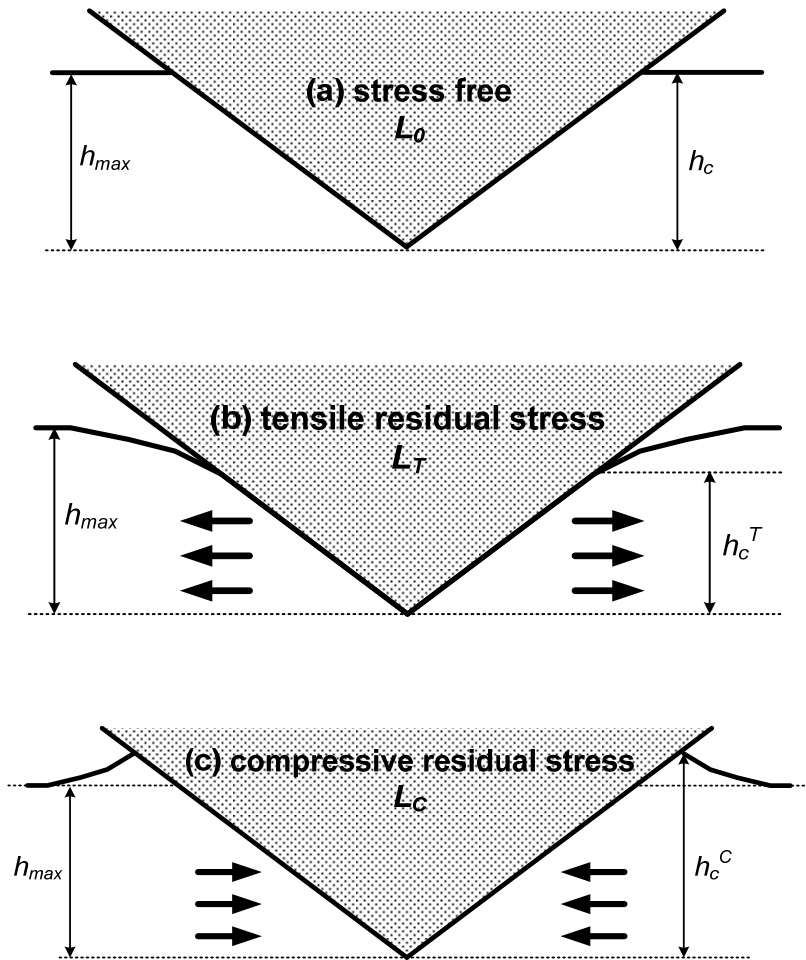


Fig. 2.17. Theoretical surface morphologies around the contact for (a) stress-free, (b) tensile stress, and (c) compressive stress states.

2.3.2. Static Indentation for Estimating Fracture Toughness

2.3.2.1. Indentation Cracking Methods

Instrumented indentation can be used to evaluate the fracture toughness of materials in a similar manner to that conventionally used in larger scale testing. During loading, tensile stresses are induced in the specimen material as the radius of the plastic zone increases. Upon unloading, additional stresses arise as the elastically strained material outside the plastic zone attempts to resume its original shape but is prevented from doing so by the permanent deformation associated with the plastic zone. There exists a large body of literature on the subject of indentation cracking with Vickers and other sharp indenters.

In general, there are various types of crack, and they are illustrated in figure 2.18 [45]. Radial cracks are vertical half-penny type cracks that occur on the surface of the specimen outside the plastic zone and at the corners of the residual impression at the indentation site. These radial cracks are formed by a hoop stress and extend downward into the specimen but are usually quite shallow.

Lateral cracks are horizontal cracks that occur beneath the surface and are symmetric with the load axis. They are produced by a tensile stress and often extend to the surface, resulting in a surface ring that may lead to chipping of the surface of the specimen. Median cracks are vertical circular penny cracks that form beneath the surface along the axis of symmetry and have a direction aligned with the corners of the residual impression. Depending on the loading conditions, median cracks may extend upward and join with surface radial cracks, thus forming two half-penny cracks that intersect the surface as shown in Fig.2-18. They arise due to the action of an outward stress. The exact sequence of initiation of these three types of cracks is sensitive to experimental conditions. However, it is generally observed that in soda-lime glass loaded with a Vickers indenter, median cracks initiate first. When the load is removed, the elastically strained material surrounding the median cracks cannot resume its former shape owing to the presence of the permanently deformed plastic material and this leads to a residual impression in the surface of the specimen.

Residual tensile stresses in the normal direction then produce a horizontal lateral crack that may or may not curve upward and intersect the specimen surface. Upon reloading, the lateral cracks close and the

median cracks reopen. For low values of indenter load, radial cracks also form during unloading (in other materials, radial cracks may form during loading). For large loads, upon unloading, the median cracks extend outward and upward and may join with the radial cracks to form a system of half-penny cracks, which are then referred to as median/radial cracks. In glass, the observed cracks at the corners of the residual impression on the specimen surface are usually fully formed median/radial cracks.

It is the radial and lateral cracks that are of particular importance, since their proximity to the surface has a significant influence on the fracture strength of the specimen. Fracture mechanics treatments of these types of cracks seek to provide a measure of fracture toughness based on the length of the radial surface cracks. Attention is usually given to the length of the radial cracks as measured from the corner of the indentation and then radials outward along the specimen surface as shown in figure 2.19.

Palmqvist [55] stated that the crack length varied as a linear function of the indentation load. Lawn, Evans, and Marshall [59] formulated a different relationship, where they treated the fully formed median/radial crack and found the ratio $P/c^{3/2}$ (where c is measured from the center of contact to the end of the corner radial crack) is a constant, the value of

which depends on the specimen material. Fracture toughness is found from:

$$K_c = \alpha \left(\frac{E}{H} \right)^{1/2} \left(\frac{P_{max}}{c^{3/2}} \right) \quad (2-38)$$

where α is an empirical calibration constant dependent on the geometry of the indenter. It was found that the value of 0.016 could give good correlation between the toughness values measured from the crack length and the ones obtained using more conventional methods. An attractive feature of using this method in indentation is that both H and E can be determined directly from analyses of indentation force-depth data. Thus, provided one has a way to measure crack lengths, implementing the method is relatively straightforward.

2.3.2.2. Indentation Fracture Toughness models for Ductile Materials

1) Critical strain model

Ju et. al [63] was modified the critical strain model proposed by Hahn and Rosenfield to evaluate the ductile fracture toughness using the mechanical properties measured from the instrumented indentation tests. The modification of the critical strain model involved: 1) the use of fracture strain from the newly develop model, consisting the stress state, i.e. stress triaxiality, and deformation parameter which can be determined from indentation tests, instead of the critical strain at ahead of crack tip, and 2) the assumption of an empirical calibrated value for the characteristic length, l^* , as the function of the strain hardening exponent [61]. To determine the fracture strain, he adopted the void growth rate considered in a rigid-perfectly plastic material by Rice and Tracey [72]. Through its integrating, the fracture strain is given by:

$$\varepsilon_f = \ln\left(\frac{R_f}{R_i}\right) / 0.32 \exp\left(1.5 \frac{\sigma_m}{\sigma}\right), \quad (2-39)$$

where R_f and R_i are the final and initial void radius, and σ_m and σ are the mean normal stress and the equivalent stress, respectively. He has shown experimentally that the ratio of void volume can be expressed by the reciprocal to the strain hardening exponent. Also ratio of stress is defined as the indentation parameter with regard to deformation. Thus, the critical fracture strain is expressed by:

$$\varepsilon_f = f\left(\frac{l}{n}\right) \exp\left(1 - \frac{6A5^n}{\pi \cdot K}\right), \quad (2-40)$$

where A is the material yield parameter, n is strain hardening exponents, and K is the strength coefficient. From the relation between the characteristic length and strain hardening exponent [61], the modified critical strain model could be defined as:

$$K_{IC} = const. \sqrt{E \cdot \sigma_{ys} \cdot n^2 \cdot f\left(\frac{l}{n}\right) \exp\left(1 - \frac{6A5^n}{\pi \cdot K}\right)}, \quad (2-41)$$

where the constant is determined experimentally.

2) Continuum damage model

From Griffith theory [73], the relation of the fracture energy, w_f and plane strain fracture toughness, K_{IC} is expressed as following:

$$K_{IC} = \sqrt{2Ew_f} \quad (2-42)$$

where E is the elastic modulus. To estimate K_{IC} on the basis of Eq.(2-58) by using the indentation technique, w_f must be determined using only indentation parameters. Triaxiality ahead of the indenter tip is in the range 2~3, and the degree of constraint in the deformed indentation region is similar to that ahead of the crack tip [62-64]. Hence the indentation energy per unit contact area to the characteristic point can be related to w_f if there is a characteristic fracture initiation point during or over the indentation process. This energy, henceforth called the critical indentation energy, is calculated from the indentation load-depth curve:

$$2w_f = \lim_{h \rightarrow h^*} \int_0^h \frac{4P}{\pi d^2} dh \quad (2-43)$$

where P is the applied load, h is the indentation depth, d is the chordal diameter of the impression and h^* is the critical indentation depth corresponding to the characteristic fracture initiation point. $2w_f$ indicates the formation of two crack surfaces.

Since there are no distinguishing marks that can be used to identify fractures occurring during indentation, h^* in Eq. (2-59) cannot be measured by direct methods (optical microscope or SEM observation). Thus to determine h^* , continuum damage mechanics (CDM) was applied to the indentation process. CDM is used mainly to predict failure in structures loaded statically and dynamically. According to Lemaitre's strain equivalence principle [74], damage variable D can be represented as following:

$$E_{eff} = E(1 - D) \quad (2-44)$$

where E_{eff} is the effective elastic modulus of the damaged material and E is the elastic modulus of the initial non-damaged material. E_{eff} decreases as h increases due to the increase in damage beneath the indenter [64]. In addition, E_{eff} is represented by a function comprised only of indentation parameters in Eq. (2-60)

From multiple loading-unloading, the values of E_{eff} for various indentation depths can be calculated from each unloading and E_{eff} vs. h may be plotted as in figure 2.20. If critical value of the elastic modulus is determined, h^* can be determined from the corresponding value of h . Since the indentation load is compressive in terms of the loading axis, the deformed region beneath the indenter experiences compressive stress. Hence, voids will be nucleated by localized shear due to compressive stress, and the void volume fraction, f will increase as h increases. The D can be represented in terms of f as:

$$D = \frac{\pi}{(1.3\pi)^{2/3}} f^{2/3} \quad (2-45)$$

From previous experimental and computational researches, the void volume fraction, f of two types is proved; the values $f_C = 0.15$ (void volume fraction at onset of coalescence) and $f_F = 0.25$ (void volume fraction at initiation of stable crack growth). The concept of critical void volume fraction was adopted to determine the critical value of the elastic modulus. Critical *CTOD* are classified as δ_C , δ_U and δ_m , but ductile structural materials generally have δ_U and δ_m . Since δ_U -type materials are brittle and have poor resistance to strain localization between voids

compared to δ_m materials, they experience abrupt loss of load-carrying capacity soon after void coalescence begins. On the other hand, δ_m -type materials retain load-carrying capacity even after the onset of void coalescence, showing gradual loss of this capacity at the initiation of stable crack growth. With these phenomena in mind, f_C is used as the fracture criterion for δ_U -type materials and f_F is used for δ_m -type materials. The f_C and f_F can be converted into corresponding damage variables D_C and D_F through Eq. (2-61); then corresponding values of E_C and E_F are calculated by Eq. (2-60). Therefore, h^* is determined as the corresponding h by using critical value of elastic modulus, $E^* = E_C$ for δ_m -type materials and $E^* = E_F$ for δ_U -type materials.

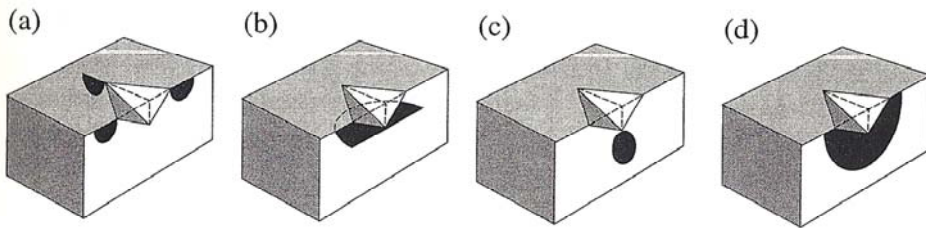


Figure 2.18. Crack system for Vickers indenter: (a) radial cracks, (b) lateral cracks, (c) median cracks, and (d) half-penny cracks [45].

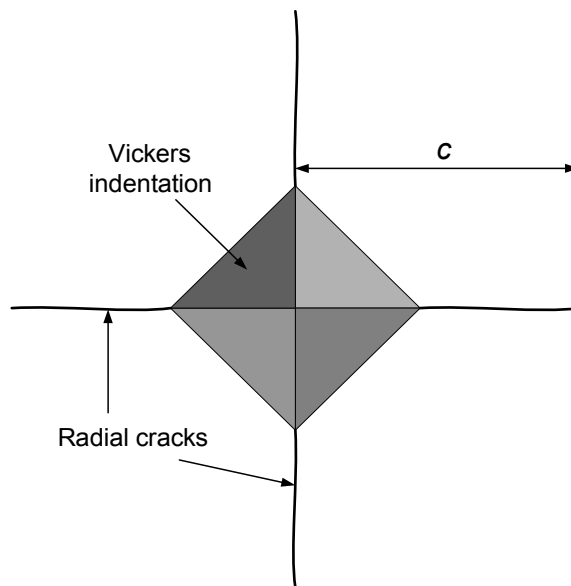


Fig. 2.19. Schematic of radial cracking by Vickers indentation.

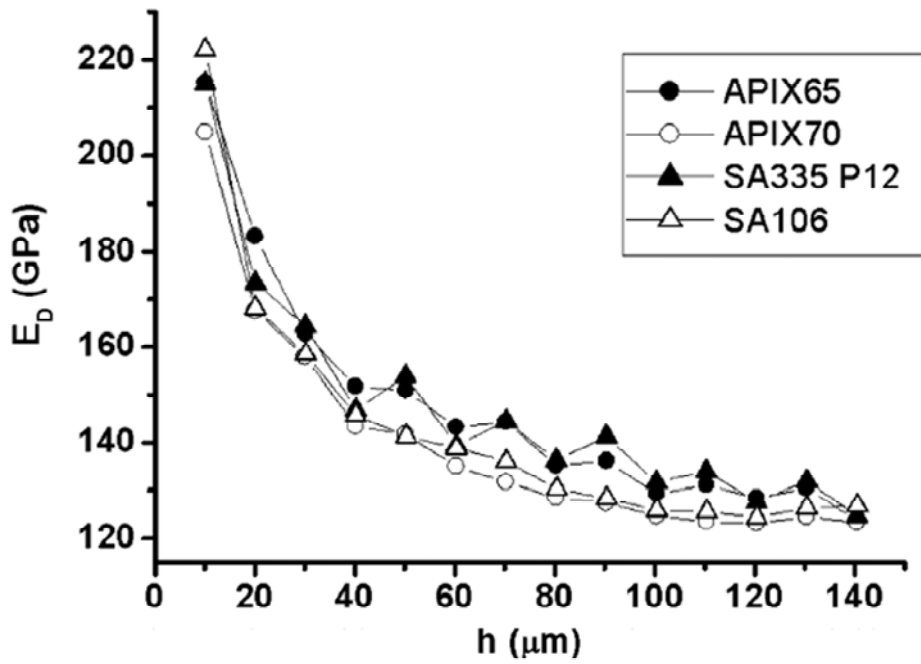


Figure 2.20. Decreasing elastic modulus with indentation depth [64].

2.3.3. Cyclic Indentation for Estimating Fatigue Properties

Instrumented indentation testing has been used over past decades as an alternative method to obtain mechanical properties such as hardness, tensile properties, residual stress, and fracture toughness. However, most researchers have focused on indentation behavior under static loading conditions. Alternatively, indentation testing with cyclic loading, called the cyclic indentation test or indentation fatigue test, has been used to investigate cyclic indentation deformation behavior and correlate conventional fatigue properties. Here we give a brief review of the work on cyclic indentation.

2.3.3.1. Cyclic indentation deformation behavior

S. Jayaraman et al. [85] studied the cyclic deformation behavior of hardened bearing steel under repeated indentation loading. They point out that the load-displacement curve for repeated indentation displays hysteresis loops and the loop parameters can reflect the cyclic properties of the material. Huber et al. [86] discussed the effect of isotropic and kinematic hardening characteristic on the indentation load-depth curve

due to cyclic spherical indentation using the finite element method. They confirmed that kinematic hardening causes hysteresis loops in indentation curve applied with unloading and reloading (Figure 2.21). They also remarked that cyclic indentation testing can be applied to determine the characteristic properties of hardening response. Pane et al. [77] studied the role of plasticity parameters on monotonic and cyclic indentation behavior, again using finite element method. They found that materials with kinematic or combined hardening laws exhibit some form of reversible plastic deformation that can be identified from the indentation hysteresis loop during the load-unload-reload cycle. All these cyclic indentation tests were carried out for several repeated indentations.

2.3.3.2. Indentation fatigue deformation behavior

Indentation deformation behavior has been studied using applied fatigue loading using fatigue tester with flat cylindrical indenters. Li et al. [87] studied the indentation fatigue response of the β -tin single crystal specimens under cyclic loading; they found that the indentation depth continues to increase and the indenter sinks further into the specimens, so that the increase in indentation depth could be used as a characteristic

measure of indentation fatigue properties. They pointed out that the increase in indentation fatigue depth is similar to that of fatigue-crack propagation. Kaszynski et al. [88] studied the indentation fatigue response of stainless steel with a Vickers diamond indenter and they found that the indentation depth varied with the logarithm of the number of cycles.

2.3.3.3. Indentation fatigue properties

The few studies on indentation fatigue method that have been carried out have shown the possibility of correlating conventional fatigue tests and indentation fatigue tests.

Recently, Xu et al. [78-81] attempted to obtain conventional fatigue properties qualitatively using a fatigue tester with indenters. They carried out indentation fatigue experiments on copper with flat cylindrical indenter and obtained indentation load-depth curve and depth-cycles curve shown in Figure 2.22. They founded that hysteresis loops exist for the indentation-depth curve and the loops never close as the number of cycles increase and defined this phenomenon as indentation ratcheting. They also confirmed that the steady-state indentation depth per cycle is a

power-law relation to the indentation load. This relation was analogue to uniaxial ratcheting equation. They thus concluded that the experimental uniaxial fatigue parameters for the steady-state stage can be obtained by the flat indentation fatigue test.

Meanwhile, Xu et al. [80] proposed a simple power-law equation that correlates indentation fatigue depth propagation and fatigue crack growth in a phenomenological way. They founded that the steady-state indentation propagation rate is a power-law function of the stress intensity range and the maximum stress intensity induced by the stress concentration at the rim of flat punch contact. They concluded that the function is quantitatively similar to steady-state fatigue crack growth as defined by well-known Paris law, pointing out that the work provides an alternative indentation technique to determine fatigue properties.

Xu et al. [78] carried out indentation fatigue tests on polyvinyl chloride (PVC) bulk material and TiN/NiP films deposited on stainless steel substrates. They monitored in-situ failure using acoustic emission during indentation fatigue testing and confirmed that cracks occurred in the specimen as the acoustic emission signal significantly increases (Figure 2.23). They also proposed that a simple power-law relationship can be established between the indentation load amplitude and number of cycle

to failure. They stated that the relationship is analogous to the conventional fatigue strength law obtained by uniaxial fatigue test. They also suggest that the fatigue stress exponents obtained by uniaxial and indentation fatigue testing agree well, so that indentation fatigue test can be an alternative method for extracting fatigue properties.

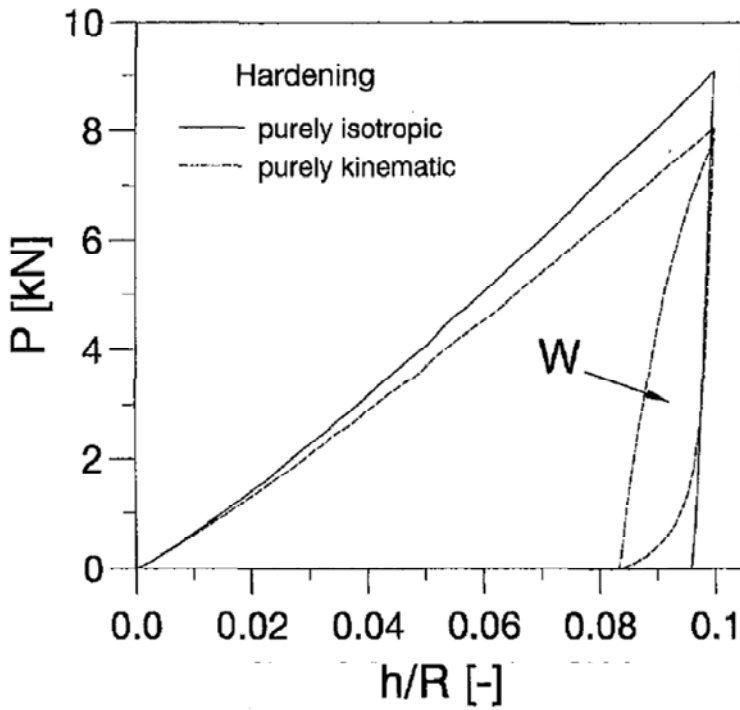


Figure 2.21. Hysteresis loops in indentation load-depth curve due to kinematic hardening [86]

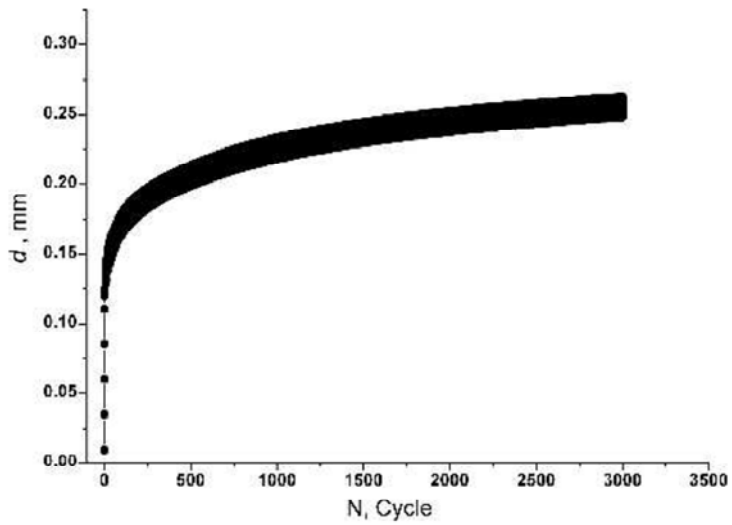
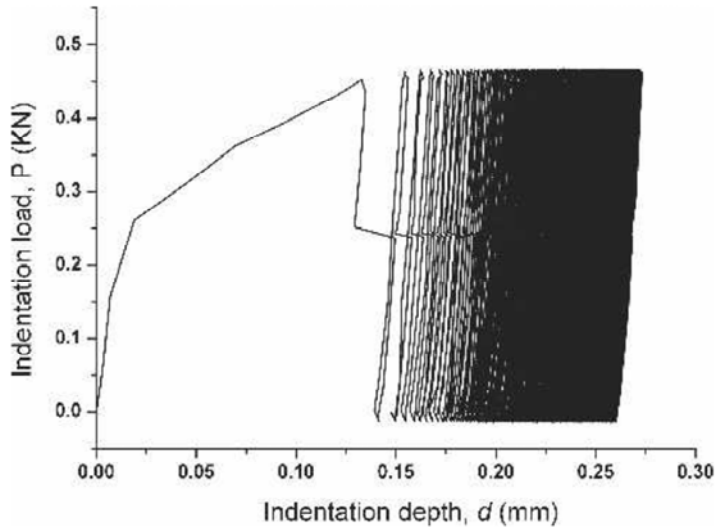


Figure 2.22. Experimental indentation curve under cycle loading [76]
 (Above: indentation load-depth curve, Below: indentation depth-cycle curve)

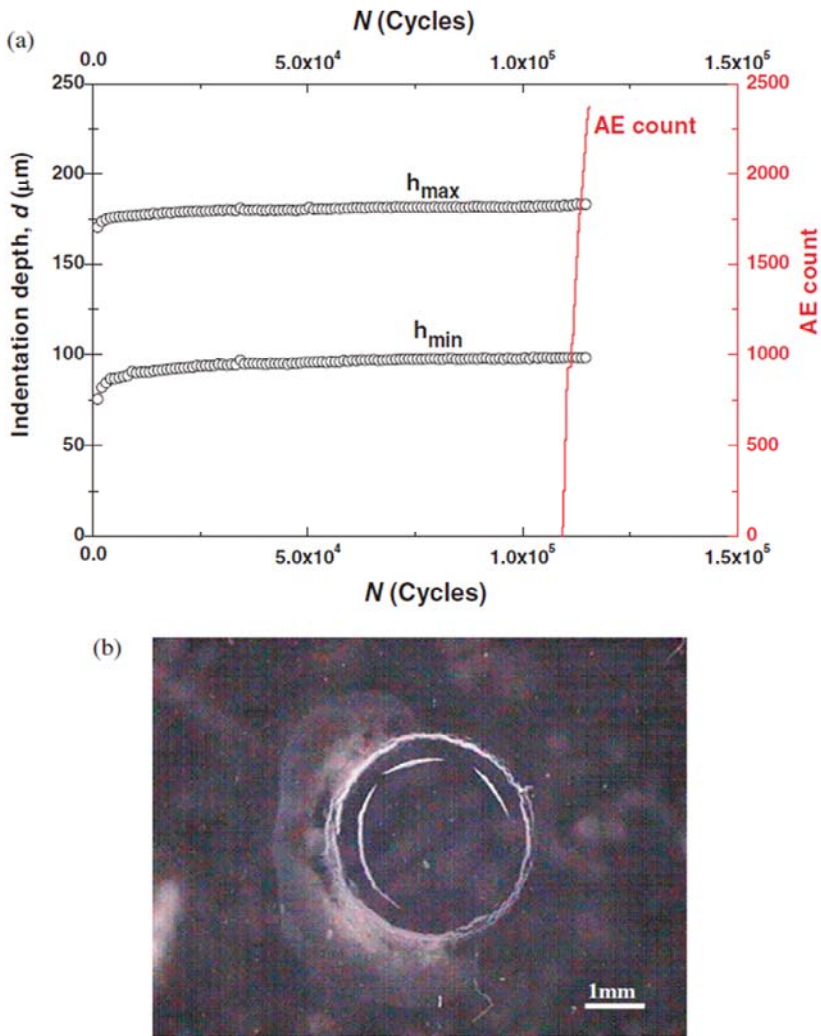


Figure 2.23. Indentation depth-cycles curve and surface topography [78]

- ((a) Evolution of indentation depth with acoustic emission count,
- (b) Surface topography near the impression after failure)

Chapter 3

Estimation of Fatigue Properties Using Cyclic Indentation

Contents

3.1	Motivation and Research Flow	86
3.2	Estimation of Bauschinger effect	89
	3.2.1. Introduction	
	3.2.2. Theoretical Modeling	
	3.2.3. Experimental Verification	
3.3	Estimation of Material Ratcheting Property	108
	3.3.1. Introduction	
	3.3.2. Phenomenological Modeling	
	3.3.3. Experimental Verification	

3.1. Motivation and research flow

Instrumented indentation testing (IIT), which measures penetration depth and applied load continuously under static indentation loading, is widely used to evaluate mechanical properties. IIT has various merit compared to other conventional mechanical testing method, and it attracts much interest as an in-situ nondestructive testing method for evaluating mechanical properties of in-service structures or components for maintenance because its simplicity and non-destructive nature. In addition, IIT can be applied at small scales (micro, nano, pico-scale) because the indentation load can be easily controlled from macro to pico ranges. It has also been used in high/low temperature testing in environmental chambers. However, since most studies of indentation testing have focused on static indentation testing, research on cyclic indentation testing has evolved but little. Cyclic indentation testing has great potential to complement conventional cyclic or fatigue testing because advantages of static IIT apply also to cyclic indentation. Perhaps cyclic indentation testing can be applied to components and materials, for which conventional fatigue testing is difficult or impossible: in-service

structures and components, weld zones, micro/nano thin films, etc. We therefore attempt here to evaluate fatigue properties using cyclic instrumented indentation testing. In this chapter, two kinds of control mode in cyclic indentation are used; cyclic indentation depth-controlled and cyclic indentation load-controlled mode. In cyclic indentation depth-controlled testing, we found a hysteresis loop in the indentation load-depth curve and analyze its cause using contact mechanics. The hysteresis loop is caused by the Bauschinger effect induced by kinematic hardening of material, we thus develop a model for evaluating uniaxial Bauschinger effect also called backstress using cyclic indentation depth-controlled tests. In the load-controlled test, we observed that indentation depth continuously increases and saturates at a certain cycle and that a hysteresis loop occur in the load-depth curve. We analyze these phenomena in terms of the hardening behavior of the material. The indentation depth increase is similar to uniaxial ratcheting, so that we develop a model for estimating the material ratcheting property. Finally, our estimated Bauschinger effect and material ratcheting property were compared to values obtained in conventional fatigue tests.

3.2. Estimation of Bauschinger effect

3.2.1. Introduction

The Bauschinger effect refers to the fact that, after some amount of forward plastic deformation in tension or compression, materials yield at a lower stress when the loading direction is reversed than in forward deformation. Since many alloys are known to exhibit the Bauschinger effect, low flow stresses can result under in-service conditions if the material is loaded in direction opposite to the stretching direction. Hence, to assess structural integrity, the Bauschinger effect should be quantitatively evaluated because yield stress caused by the Bauschinger effect induces early plastic deformation or failure of in-service materials. A common method for quantifying the Bauschinger effect involves definition of the back stress: the back stress is the difference in stress between forward and reverse flow stress at any strain value and characterizes the magnitude of permanent softening. To evaluate the Bauschinger stress, uniaxial cyclic tension-compression testing is widely used. The back stress can be obtained by replotting the cyclic uniaxial

stress-strain curve to magnitudes of the stress and the accumulated strain curve. However, the uniaxial cyclic test requires specific specimen dimensions and a complex testing-procedure, so that it cannot be applied to small-scale volume (e.g., weld zones, thin films) or to in-service structures. Among the alternative test methods available, cyclic indentation testing is attractive because simplicity of the test procedure and specimen preparations make it applicable to small-scale volume and in-service structures. We propose a phenomenological approach to estimating the uniaxial Bauschinger stress using cyclic indentation testing with a spherical indenter.

3.2.2. Theoretical Modeling

3.2.2.1. Indentation stress field

At the end of the indentation loading process, the material beneath a spherical indenter deforms plastically. For an ideal plastic material, the stress directly beneath the indenter along the axis of symmetry (i.e. along the z axis, $r=0$) is expressed by the Tresca yield criterion as

$$|\sigma_z - \sigma_r| = \sigma_y \quad (3-1)$$

where σ_z and σ_r are the normal and radial stresses. During elastic unloading, the unloading causes a uniform tensile pressure, so that the stress beneath the indenter along the axis of symmetry is expressed by the Tresca yield criterion as [24]

$$|\sigma_r - \sigma_z| = Kp_m = Kc\sigma_y \quad (3-2)$$

where K depends on the pressure distribution at the end of loading and on the depth below the specimen surface. The uniform pressure can be assumed to be approximately $3\sigma_y$ in fully plastic indentation. This pressure $3\sigma_y$ acting on the contact area is expressed by elastic contact theory at the location at which the maximum Tresca stresses develop as [24].

$$|\sigma_r - \sigma_z| = Kc\sigma_y = 0.66 \times (3\sigma_y) \quad \text{at } z=0.64a \quad (3-3)$$

Combining equation (3-1) with equation (3-3) using superposition yields the residual stress difference is expressed as

$$|\sigma_r - \sigma_z|_R = [(3 \times 0.66) - 1]\sigma_y = 0.98\sigma_y \quad (3-4)$$

Thus, at the location of maximum Tresca stress, $z = 0.64a$, plastic deformation is not to be expected during subsequent unloading. In other words, for an ideally plastic material, the material beneath the indenter deforms elastically during unloading. However, in materials that exhibit kinematic hardening, reverse plastic yielding can occur during unloading because the kinematic hardening induces permanent softening in the material when a reverse strain is applied. The decrease of yield stress induced by kinematic hardening is called back stress. Thus, reverse plastic yielding is a consequence of the Bauschinger effect in the material beneath the indenter. By the same argument, a second loading to the same maximum depth will cause a reversal of yield in the material. Therefore, for materials exhibiting the Bauschinger effect, the indentation load-depth curve displays a hysteresis loop under cyclic indentation. Suppose that decrease in uniaxial yield stress is $\Delta\sigma_b^i$ during indentation. Inserting the magnitude of this decrease, $\Delta\sigma_b^i$, into equation (3-4), we can rewrite equation (3-4) as:

$$\left| \sigma_r - \sigma_z \right|_R = 0.98(\sigma_y - \Delta\sigma_b^i) \quad (3-5)$$

When $\Delta\sigma_b^i \geq -0.02\sigma_y$, reverse plastic yielding occurs during unloading and an indentation hysteresis loop appears on subsequent loading process. Hence, the load difference caused by the softening of uniaxial yield stress represents the uniaxial back stress. Here, we newly define the load difference as the indentation back load, ΔL_b^i at a certain indentation depth. Figure 3.1 shows a schematic diagram of indentation hysteresis loop and back load.

3.2.2.2. Indentation back stress

In the previous section, the indentation back load was defined to represent uniaxial back stress. However, to estimate the uniaxial back stress quantitatively, the indentation back load must be represented as a stress term. We thus adapt Tabor's representative approach [36]. Tabor suggested that the yield stress at the edge of an indentation should be regarded as an average or a 'representative' value for the whole region of deformed zone beneath the indenter and that the mean pressure can be expressed in a linear relationship with uniaxial true stress as follows [36]:

$$\sigma_r = \frac{1}{\psi} p_m = \frac{1}{\psi} \frac{L}{A_c^2} \quad (3-6)$$

where σ_r is the representative uniaxial true stress obtained from the indentation, p_m is the mean indentation pressure, A_c is contact area and ψ is a plastic constraint factor. Tabor also suggested that the representative strain be defined using a geometric parameter, a/R on the basis of the deformation shape and strain distribution under a spherical indenter as follows [36]:

$$\varepsilon_r = 0.2a/R \quad (3-7)$$

where ε_r is the representative uniaxial strain obtained from the indentation, a is the contact radius and R is the indenter radius. Using Tabor's approach, we represent the indentation back load ΔL_b^i as uniaxial back stress $\Delta\sigma_b^i$. Substituting the indentation back load ΔL_b^i and uniaxial back stress $\Delta\sigma_b^i$ into equation (3-6), we rewrite equation (3-7) as:

$$\Delta\sigma_b^i = \frac{1}{\psi} \frac{\Delta L_b^i}{A_c} \quad (3-7)$$

where ψ is a plastic constraint factor and A_c is the contact area. Equation (3-6) is widely used in indentation research, and there are various definitions of the value of the plastic constraint factor ψ . We adopt a plastic constraint factor of 3 to evaluate the uniaxial back stress in

equation (3-7). The contact area A_c can be obtained from observation of indent by optical microscope. In addition, to estimate uniaxial back stress using equation (3-7), a certain indentation depth should be determined because the extent of the indentation back load can change with indentation depth. As discussed in 3.2.2.1, plastic deformation reaches its maximum value during unloading at the location at which the z-axis displacement z is equal to 0.64 times the contact radius a ($z=0.64a$), so that maximum indentation back load is achieved at the location. Therefore, the indentation depth corresponding to 0.64 times the contact radius is determined as critical indentation depth determining indentation back load. The method for determining the indentation back load and uniaxial back stress are compared in Figure 3.2.

3.2.3. Experimental Verification

3.2.3.1. Identification of Indentation Bauschinger Effect

Cyclic indentation depth-controlled test is performed for 4 kinds of materials (Al6061, SUS316L, SCM4, and S45C). To identify the Bauschinger effect in the indentation curve, size of hysteresis loop in the curve is examined. In addition, effect of loading rate on the hysteresis loop size is observed. The hysteresis loops are appeared in the curve for all four materials and its size depends on material. The hysteresis loop size for Al6061 and SUS316 are relatively small, and for SCM4 and S45C are relative large as shown in Figure 3.4. Its cause can be explained by mechanism of Bauschinger effect. The basic mechanism for the Bauschinger effect is related to the dislocation structure in the cold worked metal. Severe unidirectional cold working results in accumulation of dislocation at barriers and it forms stable dislocation cells. Removal of the load does not affect the dislocation cells as they have a stable structure. When stresses are applied in the reverse direction, the dislocations are now aided by the back stresses that were present at the dislocation barriers previously and also because the back stresses at the

dislocation barriers in the back are not likely to be strong compared to the previous case. Hence the dislocations glide easily, resulting in lower yield stress for plastic deformation for reversed direction of loading. Such work-softening effect is relatively low in aluminum and stainless steel because these materials exhibit less kinematic hardening effect than high carbon and medium carbon steel. So, the hysteresis loop size for Al6061 and SUS316 are relatively small compared to SCM4 and S45C. In addition, effect of loading rate on the hysteresis loop is examined. Figure 3.3 shows hysteresis loop size at different loading rate (0.01Hz, 0.06Hz, and 0.25Hz). These loading rates imply static range, quasi-static, quasi-dynamic in cyclic indentation testing, respectively. The hysteresis loop size on three different loading rates is not significant as shown in Figure 3.3. It is found that the effect of loading rate on the change of Bauschinger effect is comparative less than the effect of pre-cold working.

3.2.3.2. Model Verification

The experimental procedure is divided into four steps to estimate uniaxial Bauschinger effect. In step 1, the indentation depth amplitude corresponding to the uniaxial strain amplitude is pre-determined. Once the strain amplitude in the uniaxial cyclic test is determined, it is converted into an indentation depth amplitude using the representative method to determine the condition for cyclic indentation depth-controlled testing. In step 2, the cyclic indentation test is performed. In step 3, the indentation Bauschinger effect is determined from the load difference at which the depth which maximum tresca stress occurs in the indentation hysteresis loop. In step 4, the measured load difference is represented into a stress difference that is equivalent to a uniaxial Bauschinger effect (or backstress). To verify the proposed model, uniaxial cyclic tests and cyclic indentation test were performed on four kinds of metallic materials, Al6061, SUS316L, SCM4 and S45C, according to the above experimental procedure. Uniaxial cyclic tests were carried out under strain-controlled condition according to ASTM E606. A 100kN fatigue testing machine (MTS, USA) is used for the test (Figure 3.5). In addition, strain amplitudes are set as 0.6 %, 0.9 %, 1.2 %, 1.5 %, strain rate is set as

0.1%/sec to avoid dynamic and strain rate effect and a fully reversed cyclic test is performed to eliminate the mean stress effect (Table 3.1). Cyclic indentation depth-controlled testing was performed on four kinds of specimens sampled from the same materials used for the uniaxial cyclic test. The indentation depth amplitudes converted from uniaxial strain amplitudes are 15 μm , 22.5 μm , 30 μm , 37.5 μm , respectively. The indentation load-depth curves are measured at each depth amplitude. The Load differences at the depth which maximum Tresca stress in hysteresis loops from each indentation curve. In step 4, the measured load differences are represented into stress difference which is equivalent to uniaxial Baushinger effect (or back stress).

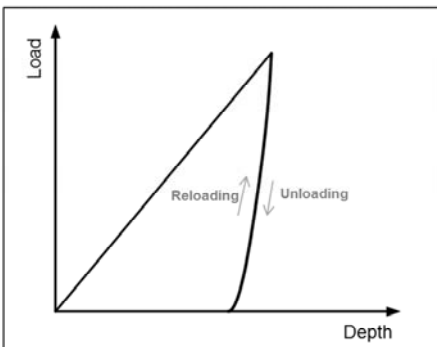
The back stresses estimated from model and measured by uniaxial cyclic testing are compared in Figures 3.6 and 3.7. The results at strain amplitude 0.6%, 0.9% are shown in Figure 3.6 and at 1.2 %, 1.6 % are shown in Figure 3.7. These results indicate an overall variation of approximately 30 % between the cyclic indentation and uniaxial cyclic tests. Further discussion of the cause of this deviation is necessary. It may arise from two sources: limitations of the indentation test itself and limitations of representative methods. First, in section 3.2.2.1, we mentioned that the stress beneath the indenter along the axis of symmetry

is tensile because the unloading cause a uniform tensile pressure. However, this tensile stress is induced by the unloading which the indenter releases. The unloading release compressive load and does not apply tensile load, so that unloading process is not exactly the same as a uniaxial tensile process. Second, in section 3.2.2.2, we represented the indentation back load to uniaxial back stress using representative methods. The plastic constraint factor, ψ , should be defined to represent the indentation load. The plastic constraint effect can vary according to material hardening behavior, so that the plastic constraint effect is expressed in the relation in terms of tensile properties [89]. However, in this study the plastic constraint factor was taken as 3, using Tabor's methods. Defining the plastic constraint factor in cyclic indentation loading is complex and difficult because the stress fields vary continuously as the indentation load and unload changes. However, the results show the possibility of applying cyclic indentation despite these limitations. Exploration of the remaining issue is postponed to future work.

Isotropic hardening

$$|\sigma_r - \sigma_z|_R \leq 0.98\sigma_y$$

➔ Elastic deformation during indentation process



Kinematic hardening

$$|\sigma_r - \sigma_z|_R = 0.98(\sigma_y - \Delta\sigma_b^i)$$

$$\Delta\sigma_b^i \geq 0.02\sigma_y$$

➔ Reversed plastic yielding by Bauschinger effect (permanent softening)

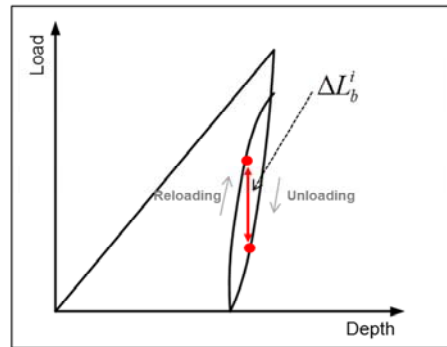
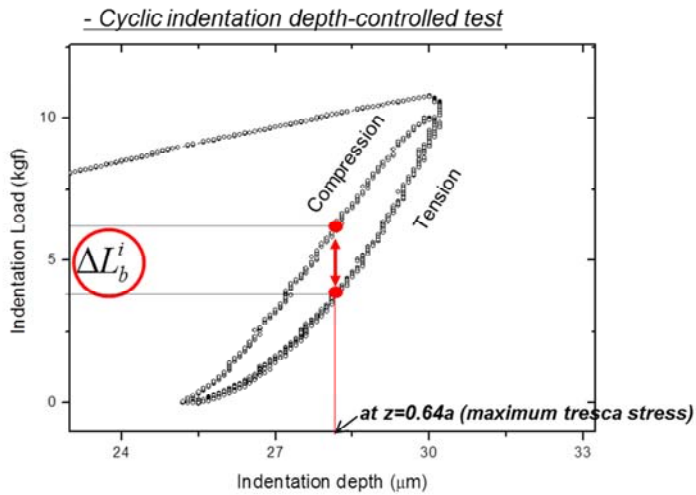


Figure 3.1. Reverse plastic yielding during indentation unloading

Cyclic indentation test



Cyclic uniaxial test

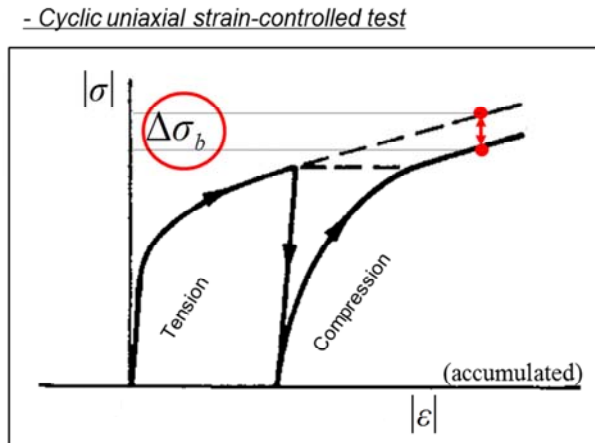


Figure 3.2. Comparison of indentation bauschinger effect and uniaxial Bauschinger effect

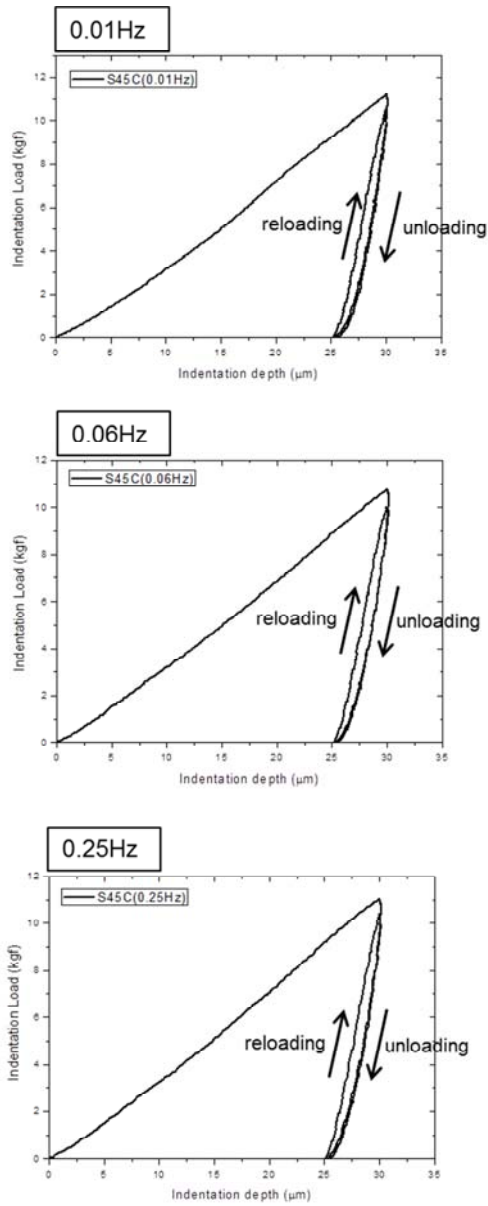


Figure 3.3. Effect of loading rate on indentation hysteresis loop

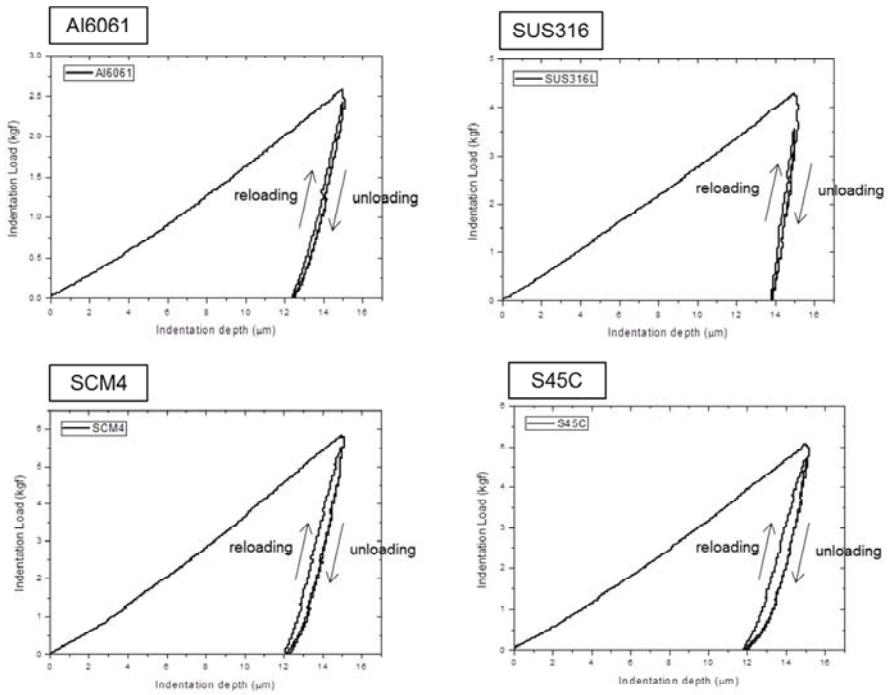


Figure 3.4. material dependency on indentation hysteresis loop

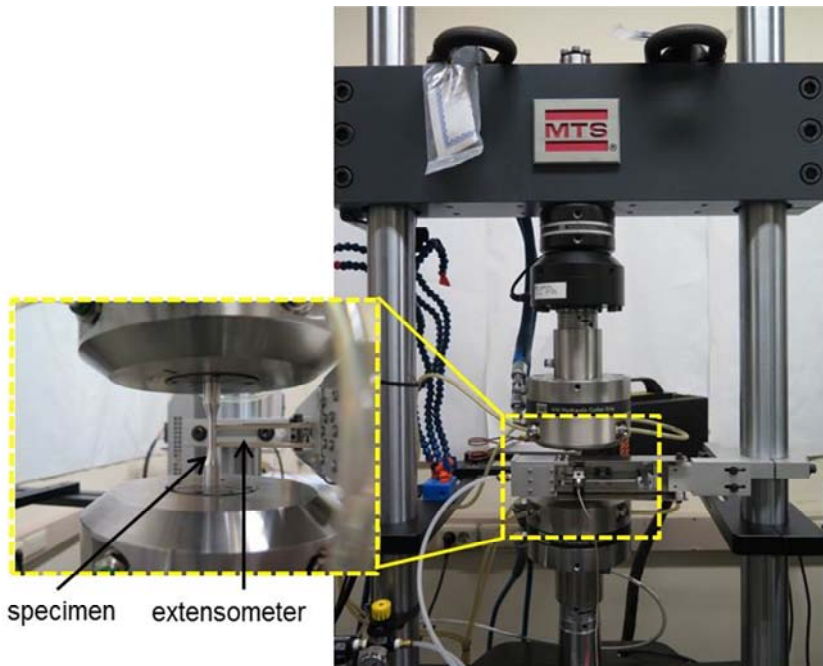


Figure 3.5. Testing machine for obtaining bauschinger effect

Table 3.1. Experimental condition detail for uniaxial ratcheting test.

Category	Detail
Testing Machine	100kN fatigue testing machine (Landmark, USA)
Standard	ASTM E606
Tested materials	Al6061, S345C, SCM4, SUS316L
Strain amplitude	0.6%, 0.9%, 1.2%, 1.5%
Loading rate	0.1%/sec
Stress ratio	-1 (fully reversed)

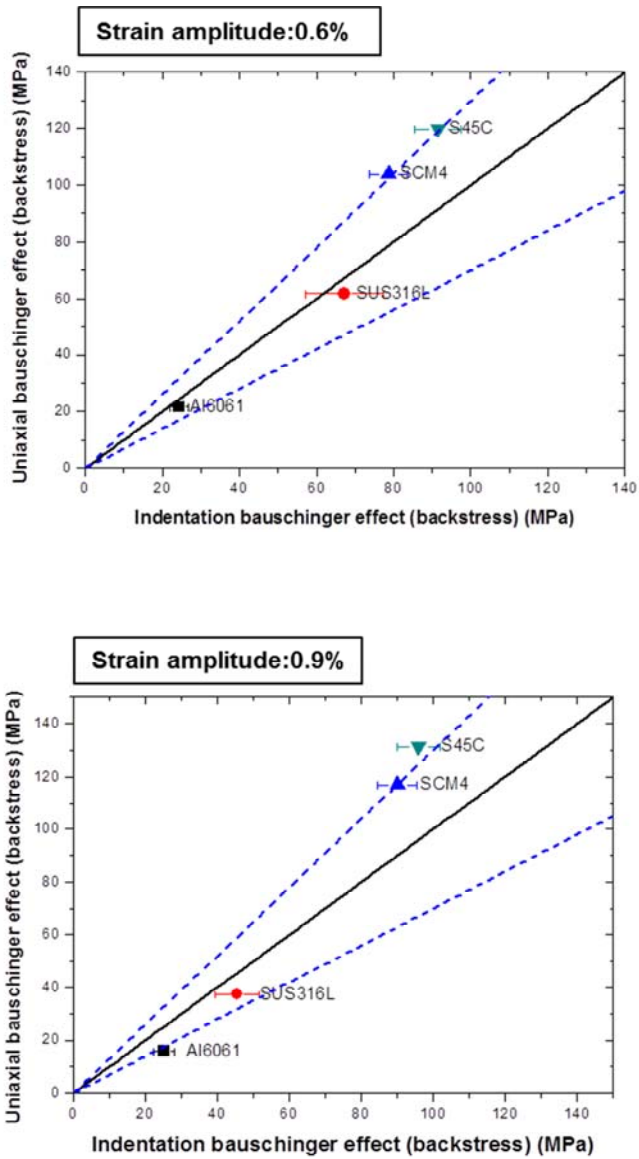


Figure 3.6. Comparison of indentation baushinger effect and Uniaxial baushinger effect at strain rate 0.6 %, 0.9 % (the dotted lines indicate a deviation of 30 %)

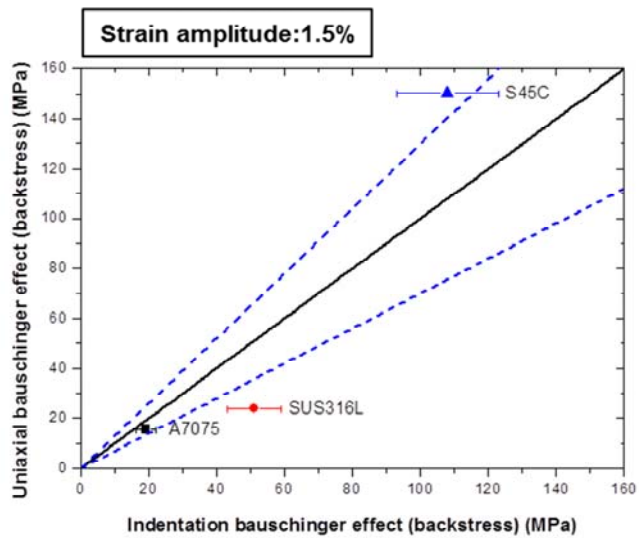
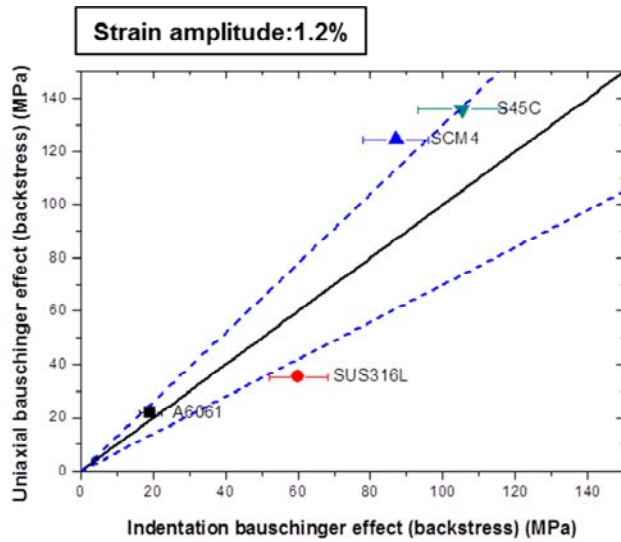


Figure 3.7. Comparison of indentation baushinger effect and Uniaxial baushinger effect at strain rate 1.2 %, 1.5 % (the dotted lines indicate a deviation of 30 %)

3.3. Estimation of Material Ratcheting Property

3.3.1. Introduction

Material ratcheting is a phenomenon in which progressive plastic strain is accumulated during cyclic loading with tensile or compression mean stress without structural effect. The uniaxial stress-controlled fatigue test is widely used to measure material ratcheting. Material ratcheting behavior can be characterized by a strain-cycle curve corresponding to a constant uniaxial stress amplitude. The strain-cycle curve can be divided by three regions that are similar to a strain-time plot in conventional creep testing: 1) primary region, 2) steady-state region and 3) tertiary regions as introduced in Section 2.1.3. In the steady-state region, the rate of plastic strain accumulation, $\varepsilon_N = d\varepsilon/dN$, saturates to a constant rate called the steady state ratcheting strain. The steady state ratcheting strain rate is known to be dependent on the terms of “maximum stress and stress amplitude” by the following power-law relationship [11]:

$$\frac{d\varepsilon}{dN} = K\sigma_{\max}^{\alpha}\Delta\sigma^{\beta} \quad (3-1)$$

where α , β , and K are material constants. These material constants can be regarded as material properties because they represent ratcheting behavior of the material corresponding to an applied stress condition. In this chapter, our goal is to estimate uniaxial material ratcheting properties using cyclic indentation testing. Xu et al. [76] carried out indentation fatigue experiments on the copper with a flat cylindrical indenter. They also verified that ratcheting occurs during indentation fatigue experiments and confirmed that the steady-state indentation depth per cycle is a power-law expression of the maximum indentation load and indentation load variation as an analogue to the steady-state ratcheting rate [76]:

$$\left(\frac{dd}{dN}\right)_{steady\ state} = K_{ind} L_{max}^{\alpha_{ind}} \Delta L^{\beta_{ind}} \quad (3-2)$$

where α_{ind} , β_{ind} , and K_{ind} are material constants obtained by cyclic indentation test. However, previous work has some limitations. First, although ratcheting behavior in cyclic indentation was found experimentally, the mechanism for ratcheting behavior was not explained theoretically. Second, the indentation ratcheting strain corresponding to a uniaxial ratcheting strain was not defined, although Xu et al. defined the

indentation ratcheting depth as the parameter corresponding to uniaxial ratcheting strain. Third, the validity of previous research has not been verified through actual experimental data. Therefore, here we explore the reason for ratcheting behavior in the cyclic indentation curve in terms of hardening behavior. In addition, we try to obtain an indentation ratcheting strain instead of an indentation depth by application of Tabor's representative method, and we then modify Xu's model. Last, the material ratcheting property is estimated using the modified model and compared with conventional uniaxial ratcheting test.

3.3.2. Phenomenological Modeling

3.3.2.1. Mechanism of indentation ratcheting

Cyclic load-controlled indentation test is used to examine the mechanism of indentation ratcheting. In cyclic load-controlled indentation testing, an indenter is pressed on the in-plane position of specimen repeatedly with constant maximum and minimum load. In the load-controlled test, additional indentation depth increments occur, unlike in the cyclic indentation depth-controlled test. The indenter should penetrate more than previous depth to press indenter until a certain load (Figure 3.8), so that the indentation depth naturally increases under cyclic load-controlled test in the early cycles. However, in later cycles, the penetration trend in indentation depth depends on the hardening behavior of the material. We examine this increasing trend for both isotropic and kinematic hardening case. Isotropic hardening occurs when the initial yield surface expands uniformly during plastic flow. The initial yield surface will expand to subsequent yield surface cycle by cycle, hence the magnitude and rate of indentation penetration depth continue to decrease as material beneath indenter hardens. Later, because the material has its own limiting yield

surface, the magnitude and rate of indentation penetration depth converge to zero (Figure 3.9). Kinematic hardening occurs when the initial yield surface translates in stress space, but the size of initial yield surface does not change during plastic flow. The initial yield surface will translate to the subsequent yield surface by the magnitude of the Bauschinger effect, α , cycle by cycle. Accordingly, the magnitude and rate of indentation penetration depth continue to increase. Later, because the material also has its own limiting yield surface, the magnitude of indentation penetration depth increase by a certain amount and the rate of indentation penetration depth converge to a constant value.

However, most metals have a tendency to combined hardening: that is, they exhibit both isotropic and kinematic hardening. In combined hardening, the magnitude of indentation penetration tends to decrease due to isotropic hardening because the influence of kinematic hardening is smaller than that of isotropic hardening for metals. In addition, as the indentation load presses repeatedly into the specimen, compressive residual stresses are accumulated in specimen substrate. So, the magnitude of indentation penetration can be decrease. But in the presence of kinematic hardening, indenter penetration increases at a constant rate because the indentation depth increases as much as the amount of

softening caused by kinematic hardening. Therefore the magnitude of indentation penetration depth will decrease but not become zero and the rate converges to a constant (or steady-state). This analysis is verified by the indentation curve obtained by constant indentation load-controlled testing shown in Figure 3.11. Finally, indentation depth penetration behavior depends on mainly compressive stress in the substrate and the softening caused by kinematic hardening; this phenomenon is notably similar to uniaxial ratcheting behavior.

3.3.2.2. Modification of previous model

As mentioned in Section 3.3.1, Xu et al proposed that the steady-state indentation depth per cycle is a power-law expression of the maximum indentation load and indentation load variation; this is an analogue equation of the steady-state ratcheting rate. We attempt to modify the equation using representative method in order to consider strain accumulation quantitatively. The indentation depth can be represented to the uniaxial strain through geometric parameter, a/R , on basis of the deformation shape and strain distribution under a spherical indenter according to Tabor's representative method [36]:

$$\varepsilon_r = 0.2a / R = 0.2 \frac{\sqrt{2Rh - h^2}}{R} \quad (3-3)$$

where a is contact radius, R is indenter radius and h is indentation depth. The maximum indentation depth in the cyclic indentation curve is represented into strain according to equation (3-3) and then the strain versus cycle curve is plotted as shown in Figure 3.10. In the strain-cycle curve, the indentation strain rate decreases continuously and converges to a steady state rate in a certain cycle. Substituting the steady-state strain rate into equation (3-2), we obtain equation (3-4):

$$\left(\frac{d\varepsilon_i}{dN}\right)_{steady\ state} = K_{ind} L_{max}^{\alpha_{ind}} \Delta L^{\beta_{ind}} \quad (3-4)$$

where K , α_{ind} , β_{ind} are material constants. In case of minimum load, we have

$$\Delta L = \frac{L_{max} - L_{min}}{2} = \frac{L_{max} - 0}{2} = \frac{L_{max}}{2} \quad (3-5)$$

Substituting $L_{max}/2$ into equation (3-4) allows us to rewrite equation (3-4) as:

$$\left(\frac{d\varepsilon_i}{dN}\right)_{steady\ state} = (K/2)^{\beta_{ind}} L_{max}^{\alpha_{ind} + \beta_{ind}} \quad (\alpha_{ind} + \beta_{ind} = n') \quad (3-6)$$

where n' is a material constant that depends on material ratcheting behavior. As the material constant value increases, the strain rate increases at a given stress.

3.3.3. Experimental Verification

To verify the modified model, uniaxial cyclic tests and cyclic indentation test were performed. A cyclic indentation depth-controlled test is performed for four kinds of specimens (Al7075, SUS316L, SCM4 and S45C). Steady-state indentation strain rates are obtained under maximum indentation loads of 5, 10, 15, 20, and 25 kgf. Figure 3.12 show that relation between the strain rate and maximum indentation load is a power-law expression. Using a log-log plot, we obtained the exponent from the slope in the curve (Figure 3.13). The exponent is compared to the exponent obtained in uniaxial fatigue testing to verify the model.

Uniaxial ratcheting tests were carried out for Al7075 under strain-controlled condition according to ASTM E606. The 100kN fatigue testing machine (MTS, USA) is used for the test. In addition, stress amplitudes are set as - 550~0MPa, - 450~0MPa and - 400~0MPa and

mean stresses are - 275MPa, - 225MPa and - 200MPa, respectively. The loading rate is set as 1Hz to avoid loading rate effect. The results shown in Figure 3.14 prove that indentation ratcheting behavior has a tendency similar to uniaxial ratcheting behavior. The steady-state indentation depth per cycle is a power-law expression of the maximum indentation load as an analogue to the steady-state uniaxial ratcheting rate. The exponents estimated from the model and measured by uniaxial ratcheting test are compared. The exponent estimated from the model is 1.638 and that measured by uniaxial ratcheting test is 2.138, so the two values deviate by 30.5%. The cause of the deviation can be the residual stress. Cyclic indentation load-controlled tests cause relatively large compressive residual stress beneath the indenter compared with uniaxial cyclic compression tests. When a zone of permanent plastic deformation is induced during indentation, releasing the applied load creates a zone of residual stress in the deformed region. The residual stresses remaining in the material after release of the indenter can influence the cyclic deformation response. However, the present results show the possibility for application of cyclic indentation despite the limitations. The model can be applied in qualitative comparison of material ratcheting behaviors. In addition, such characteristics of the cyclic indentation method as

residual stress and hardening are similar to contact fatigue as applied to railroad, bearing, etc. [8], and hence the model can also applied in fields where contact fatigue is main concern and to fundamental studies of contact fatigue.

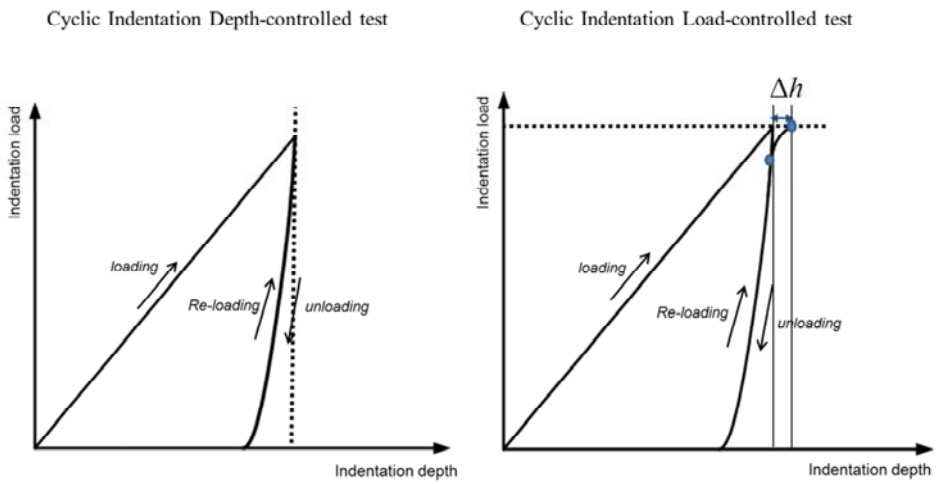


Figure 3.8. Comparison of cyclic depth-controlled test and cyclic load-controlled test.

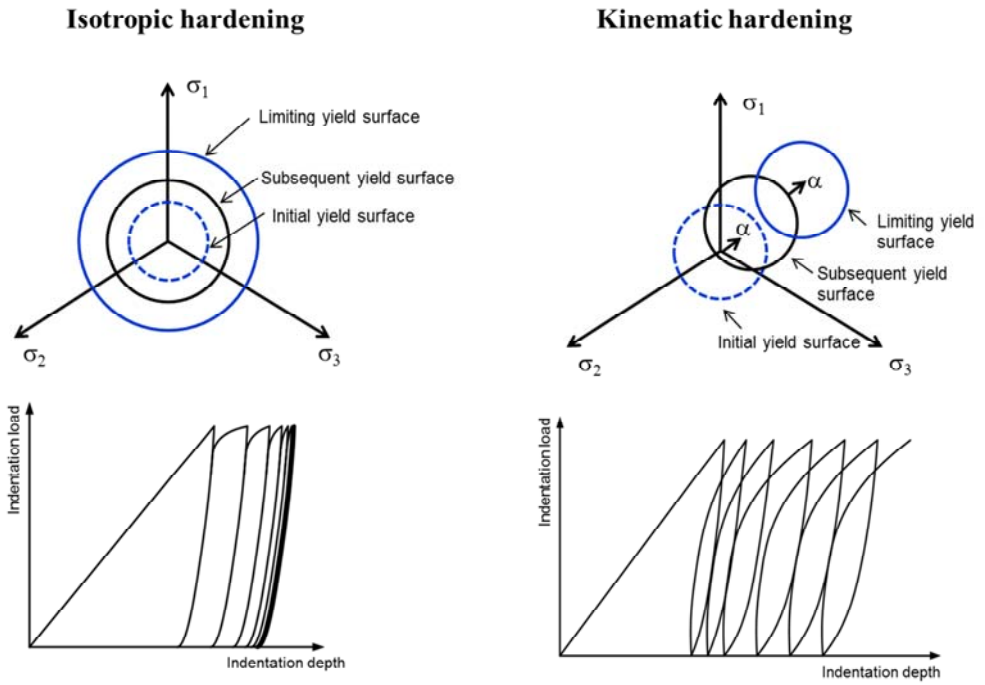


Figure 3.9. Effect of hardening rule on cyclic indentation curve

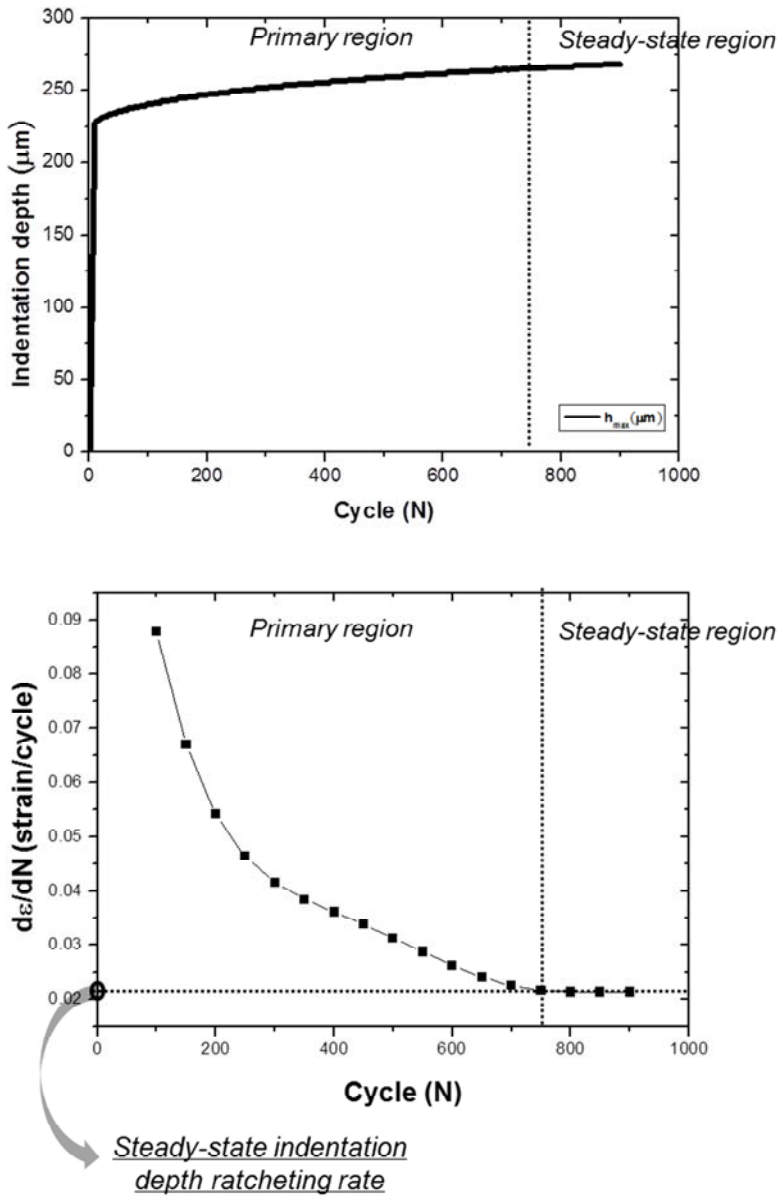


Figure 3.10. Determination of steady-state indentation strain rate.

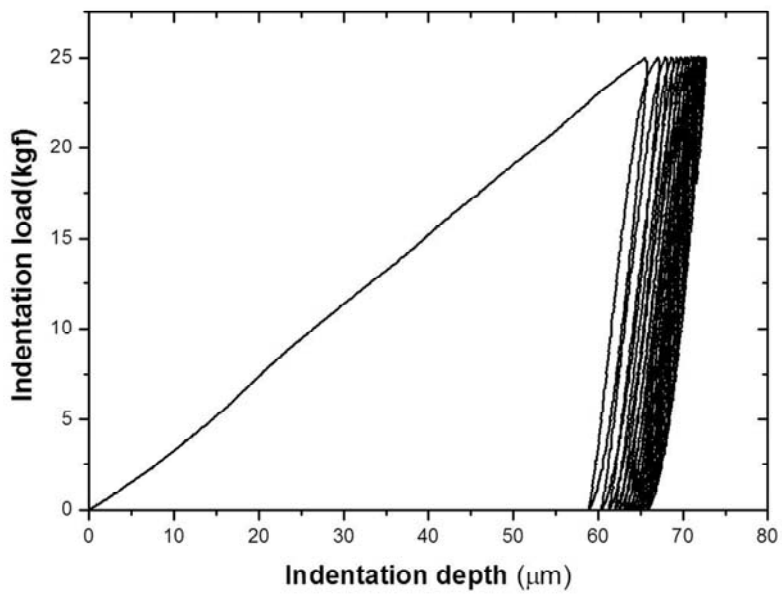


Figure 3.11. Example of indentation load-depth curve under cyclic loading test.(Material: Carbon steel(S45c))

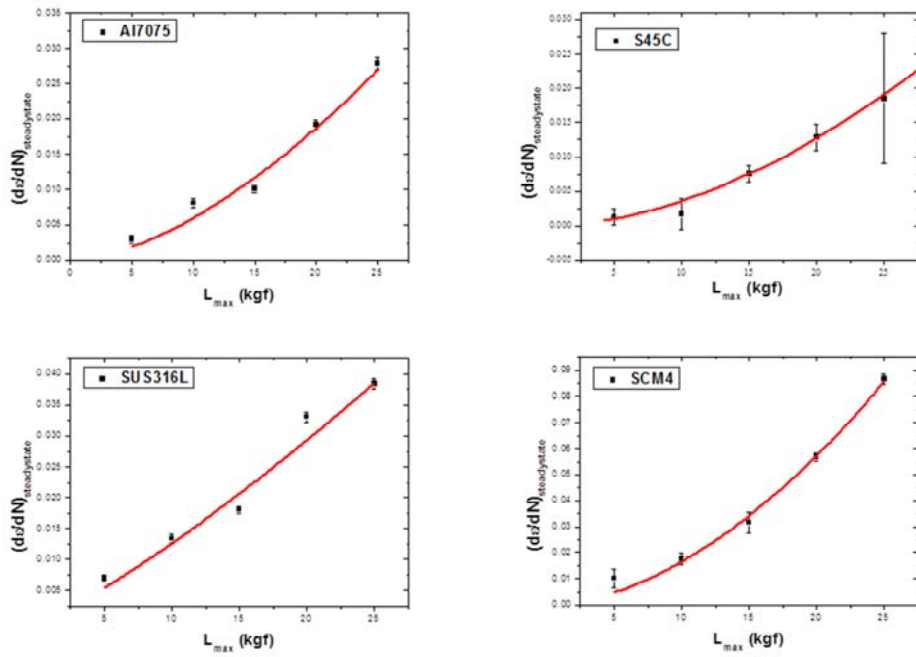


Figure 3.12. Results of indentation ratcheting test for 4 kinds of materials

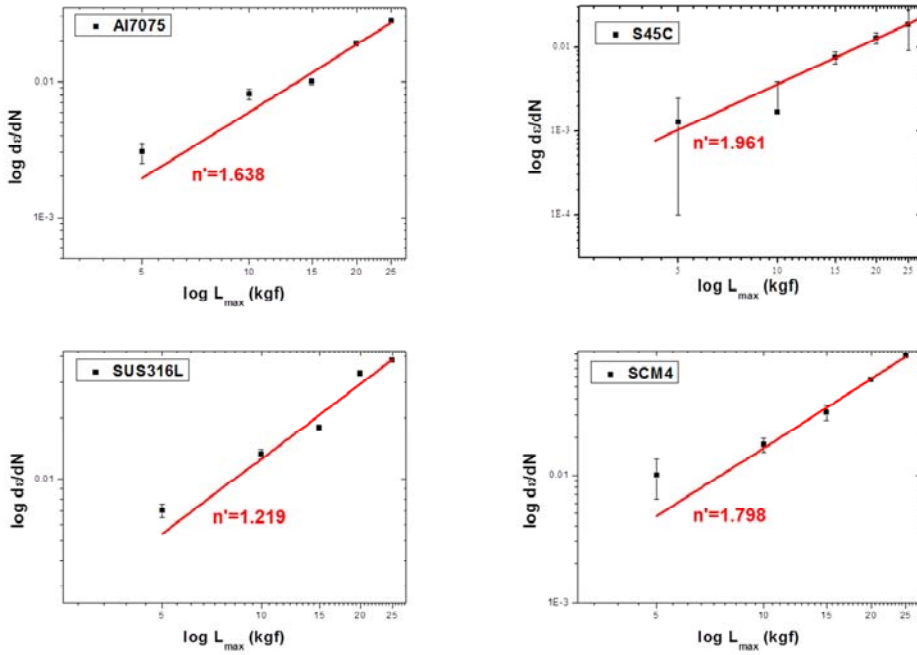


Figure 3.13. Log-log plot of indentation ratcheting test for 4 kinds of material

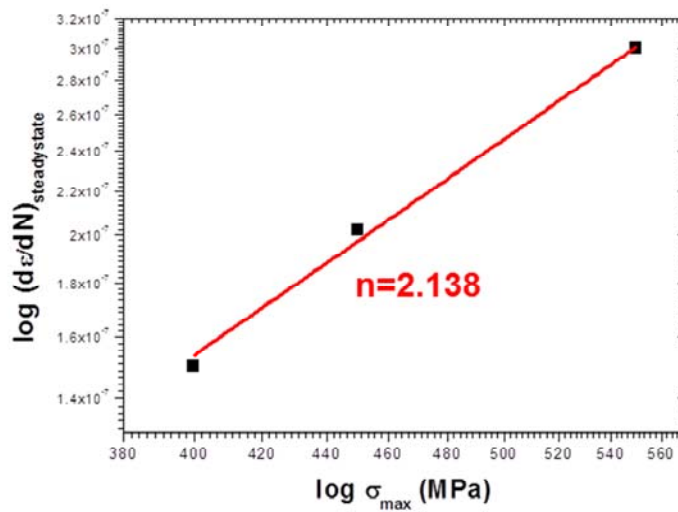
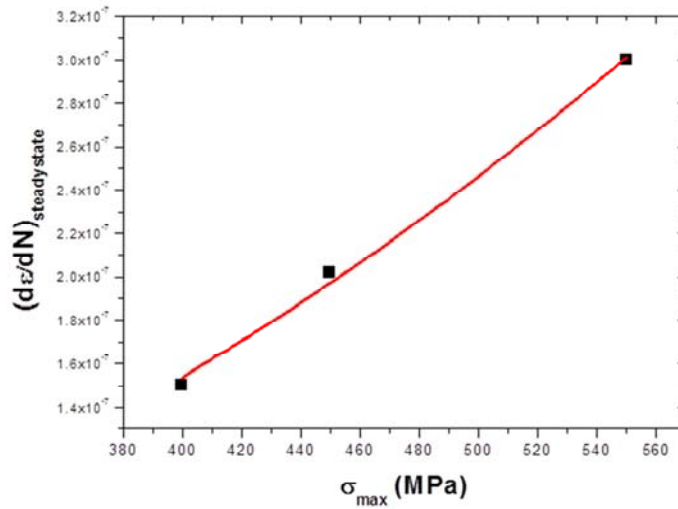


Figure 3.14. Results of uniaxial ratcheting tests for Al7075
(Above: normal plot, below: log-log plot)

Chapter 4

Development of Fracture Criterion Using Static Flat punch indentation

Contents

4.1	Introduction	126
4.2	Empirical Modeling	129
4.3	Experimental Verification	135

4.1. Introduction

Fracture toughness, defined as a material's resistance to crack propagation, is one of the most important aspects of structural integrity. Fracture toughness can be measured using standardized test methods such as those developed by ASTM and BS [1-5]. However, these methods can be difficult because they require specific specimen dimensions and complex test procedures to validate the measured values. In addition, standard measurements cannot be applied to small-volume regions (e.g., weld zones, thin films) or to in-service industrial structures because of the requirements of the test procedures and the destructive nature of the tests. Among the alternative test methods available, indentation testing is widely used to evaluate fracture toughness because of the simplicity of the test procedure and specimen preparation. In addition, indentation testing can be applied to small-volume regions and in-service structures because it is localized and nondestructive in nature. Research on indentation fracture toughness has focused primarily on brittle materials such as glass and ceramics because cracking is induced in such materials upon contact with the indenter. Lawn et al. [56-58] showed that fracture

toughness (K_{IC}) can be determined based on the relation between the crack length and the indentation load using linear elastic fracture mechanics. However, in ductile materials such as metals, cracking does not occur during indentation. Many researchers have attempted to use indentation to estimate the fracture toughness of ductile materials by adopting a criterion for a critical point corresponding to the onset of crack extension. The modified critical strain model [63], the indentation energy to fracture (IEF) model [60], the critical indentation energy model based on continuum damage mechanics [64] and the critical stress and strain indentation model [75] have been proposed for this purpose. However, these models are of two types of models for brittle metallic materials and the models for ductile metallic materials. For brittle metallic materials, the estimated fracture toughness of metals has been limited to specific ranges for relatively low fracture toughness ($K_{IC} < 120 \text{ MPa}\cdot\text{m}^{0.5}$) or in the lower shelf region of the ductile-brittle transition curve. For ductile metallic materials, the estimated value has been limited to specific range for relatively large fracture toughness ($K_{IC} > 250 \text{ MPa}\cdot\text{m}^{0.5}$) or in the upper shelf region of the ductile-brittle transition curve. Therefore, distinguishing the type of models or selecting specific models is important. We must know preliminarily whether the tested

material corresponds to brittle metallic materials-related models or ductile metallic materials-related models when a material to be tested is unknown or the fracture toughness of the material is altered due to embrittlement by degradation or low temperature. Here we propose a criterion for estimating whether a material belongs to the range of brittle fracture characteristic ($K_{JC} < 120 \text{ MPa}\cdot\text{m}^{0.5}$) or ductile fracture characteristic ($K_{JC} < 250 \text{ MPa}\cdot\text{m}^{0.5}$) using static flat punch indentation. The two key factors for developing the criterion are based on equivalence of fracture mechanics and contact mechanics. The fracture toughness values of 23 kinds of materials obtained from conventional fracture toughness test are applied to the criterion for verification. The criterion is also verified for a low-temperature embrittlement materials using low-temperature chamber.

4.2. Empirical Modeling

4.2.1. Analysis of indentation curve characteristic

The indentation of an elastic–plastic material is difficult to solve analytically due to the unknown shape and extent of the plastic field. We thus analyze the plastic behavior of material beneath an indenter using the finite element method. The analysis is carried out by means of the commercial Abaqus program. Figure 4.1 shows the Abaqus model. The model consists of a perfectly rigid flat punch (radius 500 μm) that penetrates a specimen (radius 2.5mm, thickness 2.5mm). The indenter is modeled by a rigid body while the specimen is modelled by a mesh of four nodes of axisymmetric elements. Boundary conditions are imposed along the symmetry axis and at the bottom of the specimen. The material was considered homogeneous, isotropic and described by the elastic modulus E , the Poisson coefficient ν , the yield stress σ_y and the plastic stress/strain of the uniaxial tension test. The indentation load-depth curve obtained by the finite element method exhibits a typical trend with different stage. The curve is divided into three regions (Region 1, 2, and 3)

according to plastic zone extension as shown figure 4.2. When the indenter is pressed into the specimen, small-scale yielding occurs at the contact edge of the indenter. In region 1, the material beneath the indenter is almost elastic because the plastic zone size is relatively very small. Hence, in region 1, the slope is linear and an elastic solution can be applied. As the indentation load increases, the plastic zone expands toward the symmetry axis and reaches the axis in region 2. So, in region 2, the slope is non-linear and the elastic-plastic solution must be applied. After the plastic zone reaches the axis, it extends upward and downward with the load increase, so that the material beneath the indenter undergoes fully plastic deformation in region 3. In that region, the slope has a nonlinear shape depending on the material hardening behavior.

4.2.2. Derivation of indentation fracture parameters

Indentation fracture parameters are determined from the three regions of the flat punch curve in order to develop the criterion for distinguishing brittle and ductile characteristics. The parameters can be derived from the flat punch curve because the stress field of flat punch indenter is identical to that of circumferentially cracked round bar specimen, as mentioned in

Section 2.2.3. Since the contact mechanics of flat punch indentation and fracture mechanics of a circumferentially cracked round bar specimen are almost identical, we can treat flat punch indentation as a virtual fracture toughness test with crack round bar (CRB) geometry (Figure 4.4). Because the geometry of the flat punch indenter matches that of a cracked round bar specimen, the indenter radius corresponds to the remaining ligament radius of circumferentially cracked round bar specimen (Figure 4.3). Therefore, from the indentation load-depth curve, we can derive indentation fracture parameters corresponding to virtual fracture toughness parameters and estimate the fracture characteristic through a combination of the parameters.

In region 1, the stress intensity factor of an axisymmetric rigid punch of circular contact radius a can be expressed as follows [29]:

$$K_I = \frac{P}{2a\sqrt{\pi a}} \quad (4-7)$$

where P is indentation load and a is contact radius. This result is the same as for a circular semi-infinite crack located along the circumference of a cylindrical rod (with an uncracked ligament of radius a) loaded remotely with a concentrated normal load. Hence, the indentation load can be considered to distinguish brittle and ductile material under constant

contact radius condition. We determine the maximum indentation load in region 1 as indentation fracture parameter.

In region 2, we derive the parameter from a crack determination method for a cracked round bar specimen. Scibetta et al [83] confirmed that the crack initiates at the maximum load in load-displacement curve. They also observed through fractographic analysis that ligament of a cracked round bar specimen undergoes fully plastic at maximum load. However, for metallic materials, the maximum load does not appear and the load continues to increase in the indentation curve because the plastic zone is highly constrained by the surrounding elastic material. In other word, although the condition for crack initiation might be attained, the high degree of plastic constraint is the reason that cracks do not develop during flat punch indentation of metallic materials. Cracking might occur after the fully plastic condition if the constraint effect is excluded because stress field of flat punch indenter is identical to that of a circumferentially cracked round bar specimen. Hence, we take as the indentation fracture parameter the load at the moment which fully plastic occurs. In regions 1 and 2, the maximum indentation load in the linear slope and the load at the fully plastic point are determined as indentation fracture parameters. To consider both linear elastic and elastic-plastic fracture mechanics

beneath the indenter, the slope of the line connecting the two indentation fracture loads is determined as the first key parameter, designated P' , for the criterion as shown in Figure 4.5.

After fully plastic flow occurs, the analogy between flat punch and crack round bar specimen no longer valid and the indentation increase trend is similar to the stress-strain curve in uniaxial tensile or compressive testing. In region 3, the strain-hardening exponent is determined as an indentation fracture parameter by power-law fitting in the fully plastic regions of the indentation curve, just as is done in tensile testing. In general, the effect of strain-hardening on the plastic zone ahead of the crack tip is important. In previous research, a high strain hardening effect results in a larger plastic zone because the material inside the plastic zone is capable of resisting unstable crack extension. So, we determine the strain hardening exponent obtained from the indentation curve as the second key parameter, designated n' (Figure 4.5).

Finally, we determine the criterion for distinguishing the fracture characteristic based on the general fracture behavior of material. In brittle materials such as ceramics, crack extension occurs with little or no plastic deformation after yielding ahead of the crack tip. However, in metallic materials, a large amount of plastic deformation occurs before crack

extension, so plastic deformation characteristics must be considered in determining indentation fracture parameters. So, we assume that the first key parameter reflects small-scale yield behavior ahead of crack tip and the second key parameter represents the plasticity at the crack tip. Because two key parameters are independent of each other, their product is proposed as the criterion.

4.3. Experimental Verification

4.3.1. Determining Indentation Parameters

There are two issues in obtaining the two key parameters from the flat punch curve. First, different load-depth curves are measured for different flat punch indenter sizes, as shown in Figure 4.6, because increasing the radius of flat punch indenter increases the load at the same indentation depth. To resolve the issue, the indentation curve is normalized. If the load and indentation depth are divided by the contact area and indenter radius, respectively, the normalized curves obtained are identical for different indenter sizes shown in Figure 4.7. This is derived from the geometrical self-similarity of flat punch indentation. The normalized curve can be treated as a master curve for the material that describes the response to indentation. This stress-like mean pressure and strain-like h/a curve is used in determining the parameters. Second, the moment at which fully plastic flow is reached is difficult to determine on the indentation curve. Therefore, we experimentally determined the h/a value representing the fully plastic region from the normalized curve. The h/a

value determined, 0.2, is used to determine the indentation fracture parameter in region 2.

4.3.2. Experimental detail

To verify the proposed criterion of fracture characteristic, fracture toughness tests, and indentation tests were performed on the materials listed in Table 4.1, selected on the basis of industrial requirements for fracture toughness.

Instrumented indentation tests were performed using an AIS 2100 portable indentation system (Frontics Inc., South Korea). This indentation system applies and measures real-time indentation loads and depths with a 300-kgf load cell and a linear variable displacement transducer with resolution of 0.002 kgf and 0.1 μm . The indenter was a tungsten carbide flat punch with a 500 μm radius, and testing was performed under displacement-controlled conditions at an indentation speed of 0.3 $\mu\text{m}/\text{min}$. The maximum indentation depth was 100 μm . At least three sets of indentation data were obtained from indentation tests on each material, and the average values were used to analyze the fracture toughness. Indentation specimens were 20 \times 20 \times 20 mm in size, and their surfaces

were polished with 1- μm Al_2O_3 powder.

The fracture toughness tests were performed according to ASTM E1820 [2] using two methods: the basic procedure and the resistance curve procedure. The basic method was used for materials that did not exhibit significant stable crack growth prior to fracture instability. The fracture toughness J_C was measured using the basic method. The resistance curve method was used to measure the fracture toughness J_{IC} near the onset of ductile crack extension, i.e., stable crack growth. A J - R curve was obtained using the single specimen with unloading compliance method: the crack length was computed at regular intervals while testing each specimen by partially unloading the specimen and measuring the compliance. The fracture toughness J_C and J_{IC} was converted to an equivalent K_{IC} , which is designated K_{JC} using equation (2-10). The results of the fracture toughness test and information about the specimen thickness are summarized in Table 4.1.

All test specimens with an orientation corresponding to loading in the longitudinal direction and crack propagation in the transverse direction were extracted from rolled plate. Specimens were extracted from the disk and hollow orientation of L-R, i.e., loading in the longitudinal direction and crack propagation in the radial direction. Straight fatigue pre-cracks

were made on the specimens in front of the side-notch to make the ratio of the total crack length to the specimen width (a/W) between 0.5 and 0.7 because the unloading compliance technique is less sensitive for $a/W < 0.5$. The maximum load for fatigue pre-cracking was calculated from the following equation:

$$P_m = \frac{0.5Bb_0^2\sigma_R}{S} \quad (4-8)$$

where σ_R is the flow stress, which is typically the average of the yield strength and the ultimate tensile strength. After pre-cracking was performed, side grooves were machined into each specimen to maintain a straight crack front during the J - R curve test. The total thickness reduction was 0.2B.

An INSTRON 8503 was used as the fracture toughness testing instrument. The maximum interval of the extensometer was 10 μm . Fracture toughness values for each material were averaged from at least three tests. The tested materials were heated to measure the length of the original crack. Stereographic microscopes were used to measure the crack length. Provisional J_{IC} values were determined from the J - R curves,

and verification of their validity was performed in accordance with the data requirements in ASTM E1820 [2].

4.3.3. Experimental Results

Figure 4.8 shows the results for verification of the proposed criterion. Fracture toughness values of 23 metallic materials were used to verify the criterion. It can be seen that the fracture toughness values are well distinguished by the product of two key parameters: ductile materials ($K_{JC} > 250 \text{ MPa}\cdot\text{m}^{0.5}$) are contained in the range below 1900 and brittle materials ($K_{JC} < 120 \text{ MPa}\cdot\text{m}^{0.5}$) are contained in the range over 2100. Further investigation may be required for material such as SS400, which is classified as brittle metallic material even though it is a ductile metallic material. The cause for the criterion error can be found in the results of conventional fracture tests. The material exhibits stable crack growth prior to fracture instability in fracture testing, but the fracture surface exhibits both brittle cleavage and ductile tearing, that is, both ductile and brittle fracture characteristics. Such characteristics correspond to the fracture behavior of materials in the transition temperature region. Therefore, the material can be classified as a brittle material. Although

our criterion causes an error for SS400, all materials tested except SS400 are successfully distinguished. Hence, the proposed criterion shows great potential for in-service structure and embrittlement applications.

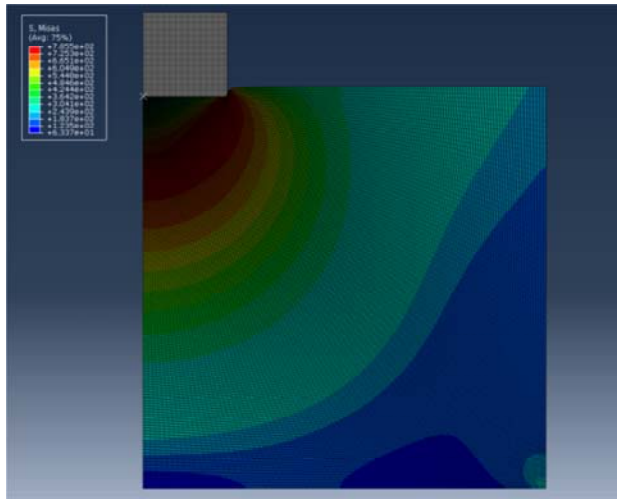


Figure 4.1. Finite element model of flat punch indentation

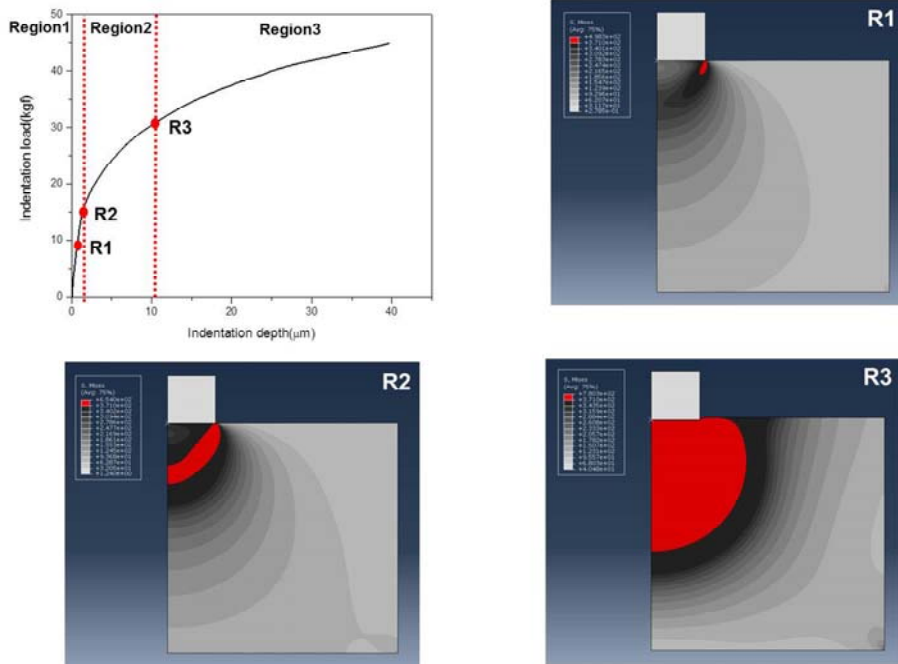


Figure 4.2. Development of plastic zone beneath flat punch indenter

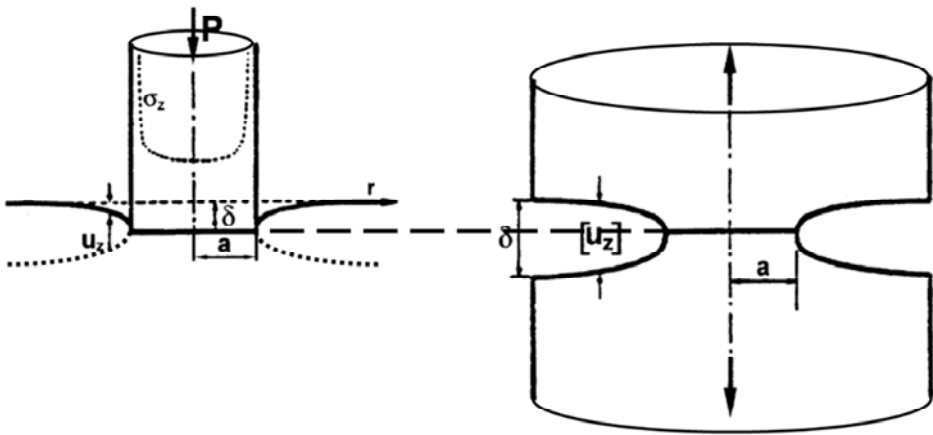
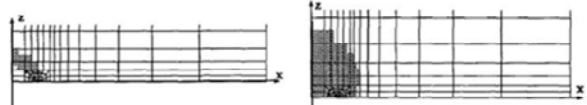
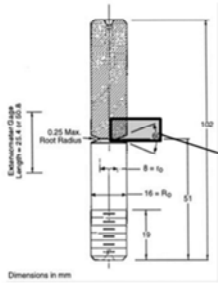


Figure 4.3. Geometrical similarity between flat punch indenter and circumferentially cracked round bar specimen

*** Cracked round bar tension**



*** Flat punch indentation**



Loading

Figure 4.4. Equivalence of cracked round bar specimen and flat punch specimen

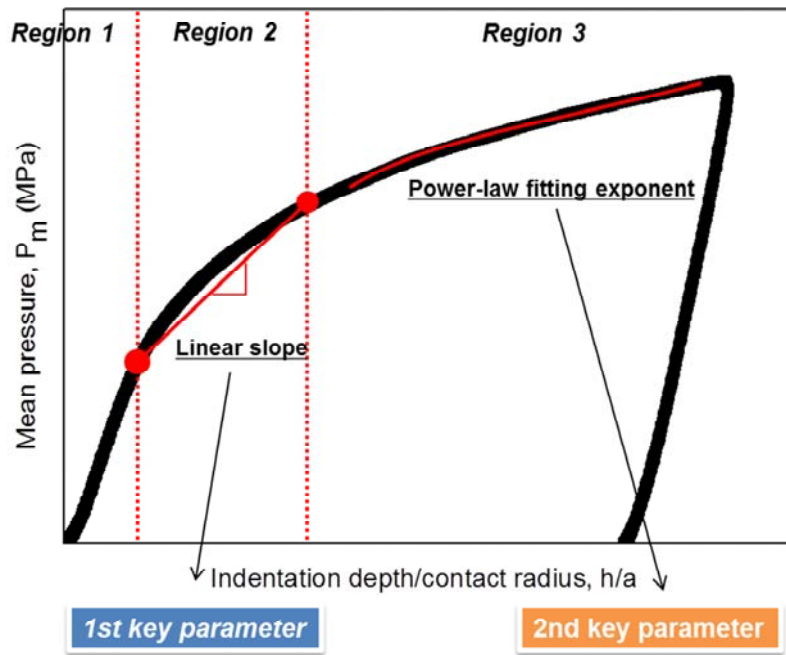


Figure 4.5. Determination of key parameters from flat punch curve

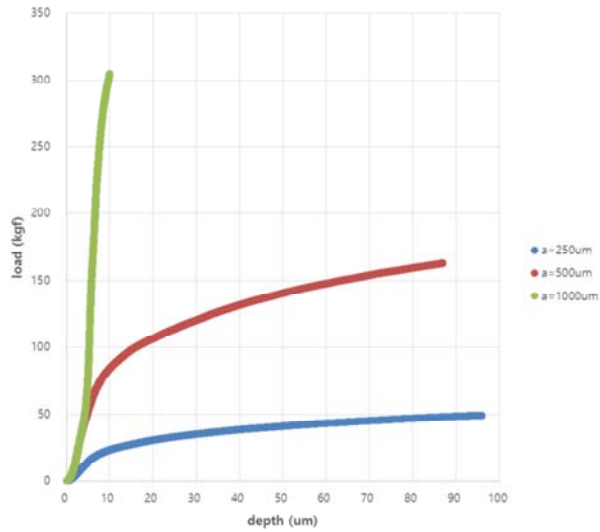


Figure 4.6. Indentation load-depth curves using flat punch indenters of various indenter radius

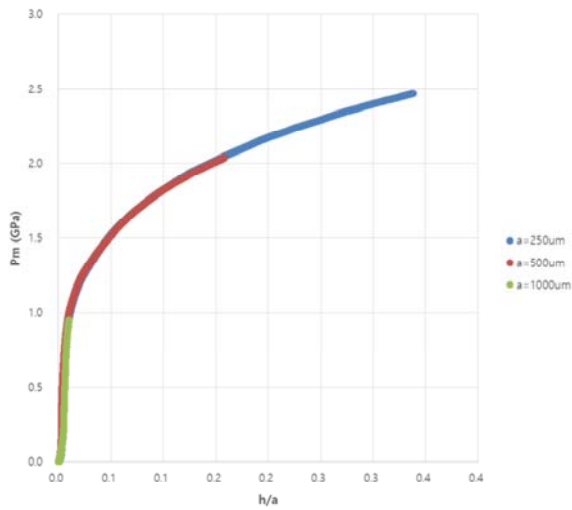


Figure 4.7. Normalization of indentation load-depth curves using flat punch indenters of various indenter radius

Table 4.1. List and fracture toughness for tested materials

No.	Material	B	J _{IC} or J _C	K _{JC}	stdev.	
Unit		mm	kJ/m ²	(MPam ^{0.5})	-	
1	Tool Steels	SKH51	8	14.57	59.75	4.356
2		SKD11	8	40.52	98.37	6.83
3		SKS3	8	60.6	118.17	5.78
4		SUJ2	8	54.38	113.87	13.03
5		SKD61	20	517.61	360.58	3.0
6	Carbon Steels & Alloy Steels	S45C	15	144.61	181.32	5.065
7		S20C	25.4	192.20	178.2	N/A
8		SCM21	15	339.98	281.37	12.034
9		SS400	20	423.05	310.21	0.052
10		API X65	14	372.91	291.18	7.986
11		API X100	19	548.24	352.8	19.073
12		API X120	16	687.95	395.52	9.254
13		SA508Gr.1	25.4	1145.38	501.73	N/A
14		SA508Gr.3	25.4	550.83	340.02	N/A
15		SA516	25.4	1123.92	499.49	N/A
16	A36	25.4	1104.69	447.01	N/A	
17	Stainless steel	SUS304	20	537.13	349.27	17.054
18		SUS304L	20	666.29	389.21	11.037
19		SUS347	23	591.39	366.74	6.434
20		SUS321	22	499.02	336.91	2.673
21	Ti-alloy	Ti-6Al-4V	9	90.155	113.622	11.426
22		Ti-5Al-2.5Sn	9	61.555	86.626	5.734
23		Ti-10Al-2Fe-3Al	9	94.073	106.465	4.024

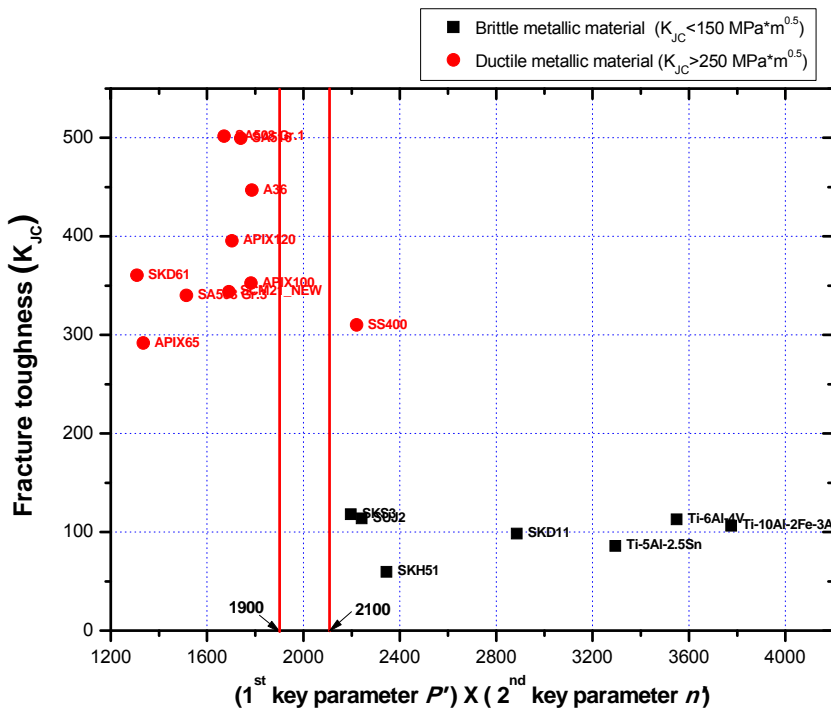


Figure 4.8. Results of verification for the criterion.

Chapter 5

CONCLUSIONS

We have proposed a new model for evaluating fatigue properties and the new criterion for distinguish brittle and ductile characteristic. The two modes of cyclic indentation, cyclic indentation depth-controlled and cyclic indentation load-controlled mode, are used to estimate the uniaxial Bauschinger effect and material ratcheting property.

In cyclic indentation depth-controlled testing, we found that a hysteresis loop in the indentation load-depth curve and is caused by the Bauschinger effect induced by kinematic hardening. We thus developed a new model for evaluating the uniaxial Bauschinger effect, also called backstress.

In the load-controlled test, we observed that indentation depth continuously increases and saturates at a certain cycle. We analyze this phenomenon in terms of hardening behavior and confirmed that the indentation depth increase behavior is similar to uniaxial ratcheting behavior. Hence, we developed a modified model for estimating the material ratcheting property. The estimated Bauschinger effect and material ratcheting property were verified by comparison to values from conventional fatigue tests.

In analyzing the fracture criterion, static flat punch indentation was also used to develop a new criterion for estimating the fracture

characteristic of materials. We propose a criterion for estimating whether a material falls in the range of brittle fracture characteristic ($K_{Jc} < 150 \text{ MPa}\cdot\text{m}^{0.5}$) or ductile fracture characteristic ($K_{Jc} < 250 \text{ MPa}\cdot\text{m}^{0.5}$) using static flat punch indentation. The two key factors in criterion are determined based on equivalence of fracture mechanics and contact mechanics and the strain-hardening effect on the plastic zone of the crack tip. The fracture toughness values of 23 kinds of materials obtained from conventional fracture toughness testing are applied to verify the validity of the criterion. The brittle and ductile metallic materials are well distinguished by the proposed criterion.

Reference

- [1] ASTM standard E399: Standard Test Method for Linear-Elastic Plane-Strain Fracture Toughness K_{Ic} of Metallic Materials (2009)
- [2] ASTM Standard E1820: Standard Test Method for Measurement of Fracture Toughness (2009)
- [3] British Standard 7448-1: Fracture mechanics toughness tests, The British Standards Institution (1991)
- [4] ASTM standard E466: Standard Practice for Conducting Force Controlled Constant Amplitude Axial Fatigue Tests of Metallic Materials (2015)
- [5] ASTM standard E466: Standard Test Method for Strain-Controlled Fatigue Testing (2012)
- [6] ASM Handbook volume 19: Fatigue and Fracture (1996)
- [7] J. Bauschinger, *Civiling*. N. F. 27, 289 (1881)
- [8] S. Suresh, *Fatigue of Materials*, Cambridge University Press (1998)

- [9] S.K. Paul, S. Sivaprasad, S. Dhar, S. Tarafder, *J. Mater. Sci.* **47**, 4660 (2012)
- [10] M. Dahlberg, P. Segle, *Swedish Radiation Safety Authority*, **45** (2010)
- [11] M. M. Megahed, A. R. S. Ponter, C. J. Morrison, *Int. J. Mech. Sci.* **26**, 625 (1984)
- [12] R. Sowerby, D. K. Uko, Y. Tomita, *Mater. Sci. Eng.* **41**, 43 (1979)
- [13] A. Abel, H. Muir, *Philos. Mag.* **26**, 489 (2006)
- [14] H. Hubel, *Nuclear Engineering and Design* **162**, 55 (1996)
- [15] H.M. Westergad, *J. App. Mech.* **6**, 49 (1939).
- [16] G.R. Irwin, *J. App. Mech.* **24**, 361 (1957).
- [17] J.M. Barsom and S.T. Rolfe, *Fracture and fatigue control in structures: application of fracture mechanics 3rd* (ASTM, 1999).
- [18] W.S. Pellini, *Proc.: Joint United States-Japan Symposium on Application of Pressure Component codes*, Tokyo, Japan, March 13-15 (1973).
- [19] T.L. Anderson, *Fracture Mechanics 3rd edition* (CRC Press, 2005).

- [20] J.R. Rice and G.F. Rosengren, *J. Mech. Phys. Solids* **16**, 1(1968).
- [21] I. N. Sneddon, *Int. J. Eng. Sci.* **3** (1965).
- [22] S. Timoshenko, J.N. Goodier, *Theory of Elasticity, third ed.*, (McGraw Hill, New York, 1951).
- [23] R.F. Bishop, R. Hill, N.F. Mott, *Proc. Phys. Soc. London* **57** (1945).
- [24] K.L. Johnson, *Contact Mechanics* (Cambridge University Press, Cambridge, 1985).
- [25] K. Lange, *Handbook of Metal Forming*, (McGraw Hill, New York, 1980).
- [26] W. Yu, J.P. Blanchard, *J. Mater. Res.* **11** (1996).
- [27] R.T. Shield, *Proc. R. Soc. A* **233** (1955).
- [28] G. Eason, R.T. Shield, *Zeitschrift für Angewandte Mathematik und Physik* **11** (1960).
- [29] I. N. Sneddon, *Proc. Cambridge Philos. Soc.*, **42** (1946).
- [30] H. Tada, P. C. Paris, and G. R. Irwin, *Stress Analysis of Cracks Handbook*, (Del Research Corporation, Hellertown, 1973).
- [31] D. P. H. Rooke and D. J. Cartwright, *Compendium of Stress Intensity Factors*, (Her Majesty's Stationary Office, London, 1976).

- [32] Y. Murakami, *Stress Intensity Factors Handbook*, (Pergamon Press, New York, 1987).
- [33] M.F. Doerner and W.D. Nix, *J. Mater. Res.* **1**, 601 (1986).
- [34] W.C. Oliver and G.M. Pharr, *J. Mater. Res.* **7**, 1564 (1992).
- [35] W.C. Oliver, G.M. Pharr. *J. Mater. Res.* **19**, 3 (2004).
- [36] D. Tabor, *The Hardness of Metals*, Clarendon Press (1951).
- [37] D.M. Marsh, *Proc. of Res. Soc. of London*, Ser. **A 279**, 420 (1964)
- [38] C.H. Mok, *Exp. Mech.*, **87** (1966).
- [39] R.A. George, S. Dinda, A.S. Kasper, *Metals progress*, **30**, (1976)
- [40] D. Kramer, H. Huang, M. Kriese, J. Robach, J. Nelson, A. Wright, D. Bahr, W.W. Gerberich, *Acta. Mater.*, **47**, 333 (1999).
- [41] J.H. Underwood, G.P. O'Hara, J.J. Zalinka, *Exp. Mech.*, **379** (1986).
- [42] H.A. Francis, *Trans. of ASME*, **9** 272 (1976).
- [43] F.M. Haggag and G.E. Lucas, *Mater. Tran. A* **14A**, 1607 (1983)
- [44] J.S. Field, M.V. Swain, *J. Mater. Res.*, **10**, 101 (1995).

- [45] A.C. Fischer-Cripps, B.R. Lawn, *Acta Mater.*, **44**, 519 (1996).
- [46] J. Alcala, A.E. Giannakopoulos, S. Suresh, *J. Mater. Res.*, **13**, 1390 (1998).
- [47] B. Taljat, T. Zacharia, F. Kosel, *Int. J. Solids Struct.*, **35**, 4411 (1998).
- [48] J.H. Ahn, D. Kwon, *J. Mater. Res.*, **16**, 3170 (2001).
- [49] J.Y. Kim, K.W. Lee, J.S. Lee, D. Kwon, *Surf. Coat. Technol.* **201**, 4278 (2006).
- [50] T.Y. Tsui, W.C. Oliver, G.M. Pharr. *J. Mater. Res.* **11**, 752 (1996).
- [51] S. Suresh, A.E. Giannakopoulos. *Acta Mater.* **46**, 5775 (1998).
- [52] A. Bolshakov, G.M. Pharr. *J. Mater. Res.* **13**, 1049 (1998)
- [53] Y.H. Lee, D. Kwon. *J. Mater. Res.* **17**, 901 (2002).
- [54] Y.H. Lee, D. Kwon. *Acta Mater.* **52**, 1555 (2004).
- [55] S. Palmquist, *Jernkontorest Ann.* **141**, 300 (1957).
- [56] B.R. Lawn BR and J. Wilshaw, *J. Mater. Sci.* **10**, 1049 (1975).
- [57] B.R. Lawn, M.V. Swain, *J. Mater. Sci.* **10**,113 (1975).

- [58] B.R. Lawn, E.R. Fuller, *J. Mater. Sci.* **10**, 2016 (1975).
- [59] B.R. Lawn, A.G. Evans, D.B. Marshall, *J. Am. Ceram. Soc.* **63**,574 (1980).
- [60] F.M. Haggag and R. K. Nanstad, ASTM PVP **170**, 41 (1989).
- [61] G.T. Hahn and A.R. Rosenfield, ASTM STP432, American Society for Testing and Materials, 5 (1968): Philadelphia.
- [62] T.S. Byun, J.W. Kim, J.H. Hong, *J. Nucl. Mater.* **252**, 187 (1998).
- [63] J.B. Ju, Ph. D. thesis in Seoul National University, (2003).
- [64] J.S. Lee, J.-i. Jang, B.W. Lee, Y. Choi, S.G. Lee, and D. Kwon, *Acta. Mater.* **54**, 1101 (2006).
- [65] ISO 14577-1: *Metallic Materials – Instrumented Indentation Test for Hardness and Materials Parameters – Part 1: Test Method* (2002).
- [66] ISO 14577-4: *Metallic Materials – Instrumented Indentation Test for Hardness and Materials Parameters – Part 4: Test Method for Metallic and Non-metallic Coatings* (2007).
- [67] ISO/TR 29381: *Measurement of Mechanical Properties by an Instrumented Indentation Test – Indentation Tensile Properties* (2008).

- [68] G.M. Pharr and A.J. Bolshakov, *J. Mater. Res.* **17**, 2660 (2002).
- [69] Y. Liu, A.H.W. Ngan, *Scripta Mater.* **44**, 237 (2001).
- [70] J.Y. Kim, J.J. Lee, Y.H. Lee, J.I. Jang, D. Kwon, *J. Mater. Res.* **21**, 2975 (2006).
- [71] G.R. Antis, P. Chantikul, B.R. Lawn, D.B. Marshall, *J. Am. Ceram. Soc.* **64**, 533 (1981).
- [72] J.R. Rice and D.M. Tracey, *J. Mech. Phys. Solids*, **17**, 201 (1969).
- [73] A.A. Griffith, *Phil. Trans. A* **221**, 163 (1920).
- [74] J. Lemaitre, *J. Eng. Mater. Tech.*, **107**, 83(1985).
- [75] S.-W. Jeon, K.-W. Lee, J.Y. Kim, W.J. Kim, C.-P. Park, D. Kwon, *Experimental Mechanics*, (2016)
- [76] B.X. Xu, Z.F. Yue, *J. Mater. Res.* **21**, 1793 (2006)
- [77] I. Pane, E. Blank, *Int. J. Solids Struct.* **43**, 2014 (2006)
- [78] B. Xu, Y. Akio, Xi Chen, *Philos. Mag. Lett.* **90**, 313 (2010):
- [79] Xu, B. X., Z. F. Yue, *J. Mater. Res.* **22**, 186 (2007)
- [80] Xu, Baoxing, Zhufeng Yue, Xi Chen, *Scripta Mater.* **60**, 854 (2009)

- [81] Xu, B. X., Z. F. Yue, J. Wang, *Mech. Mater.* **39**, 1066 (2007)
- [82] M. Scibetta, R. Chaouadi, and E. Van Walle, *International Journal of Fracture*, **104** (2000)
- [83] B. Riccardi, R. Mntanari, *Mater. Sci. Eng. A*, **381** (2004).
- [84] G.E. Dieter, *Mechanical Metallurgy* (McGraw-Hill, New York, 1986).
- [85] S. Jayaraman, W. Oliver, G.T. Hahn, P. Bastias, C. Rubin, *Scr. Metall. Mater.* **29**, 122 (1993)
- [86] N. Huber, Ch. Tsakmakis, *J. ENG. MATER-T. ASME*, **120**, 143 (1998)
- [87] C.M. Li, *Mater. Sci. Eng. A*, **322**, 23 (2002).
- [88] P. Kaszynski, E. Ghorbel, D. Marquis, *Journal of Engineering Materials and Technology*, **120(3)**, 218 (1998)
- [89] S.K. Kang, Y.-C. Kim, K.-H Kim, J.-Y Kim, D. Kwon, *Int. J. Plasticity*, **49**, 1 (2013)
- [90] A.A. Wells, *Proc. Crack Prop. Sym.* **1**, 84 (1961).

초 록

구조 건전성은 변형, 파괴, 혹은 피로에 의한 파손 없이 설계된 가동하중을 견딜 수 있는 구조 혹은 부품의 능력을 의미한다. 구조 건전성이 있는 구조물을 설계 및 건설하기 위해서 공학자는 반드시 강도, 경도, 파괴인성 및 피로물성과 같은 재료의 기계적 물성을 고려해야 하고, 장수명을 위해 요구되는 하중을 견딜 수 있는 적합한 크기, 두께, 형상을 결정해야 한다. 많은 파손사례에 있어 구조의 파손은 열화 혹은 취화에 의한 재료의 기계적 물성의 변화에 의해 발생하므로 구조건전성 평가를 위해 가동 중 구조물의 부품의 기계적 물성을 평가하는 것은 중요하다.

구조건전성을 위해 평가가 요구되는 가장 중요한 물성 중에 피로물성과 파괴인성은 ASTM 과 BS 에 의해 개발된 표준화된 시험법을 통해 결정된다. 그러나, 이러한 시험법은 특수한 시험편 크기 및 형상과 복잡한 시험절차를 요구하기 때문에 가동 중 구조물 혹은 용접부와 같은 재료의 국부 영역에 직접적으로 적용될 수 없다. 이와 같은 한계로 인해, 기존 표준 시험법을 보완, 대체할 수 있는 시험법이 개발되어 왔다.

현장의 가동 중 구조물을 비파괴적으로 평가하기 위해 개발된 연속압입시험법은 압입하중 및 깊이를 분석하여 경도, 탄성계수, 인장물성, 잔류응력 및 파괴인성과 같은 다양한 기계적 물성을 평가할 수 있다. 연속압입시험은 시험 후 재료표면에 아주 작은

압흔만을 남기기 때문에 비파괴 시험법으로써 가동 중 실시간 평가가 가능할 뿐만 아니라, 나노스케일에서 매크로스케일까지 시험하중을 조절함으로써 국부 영역 물성을 맵핑하여 평가하는 것이 가능하다. 이러한 연속압입시험에 대한 대부분의 연구는 주로 정적인 하중을 인가하는 정적압입시험에 초점을 맞춰 진행되어 왔다. 반면 동적인 하중을 반복적으로 인가하는 반복압입시험에 대한 연구는 반복압입하중에 대해 나타나는 재료의 현상을 해석하는 현상론적인 접근이 시도되고 있으나, 기존 시험법의 피로물성과 연관시키기 위한 연구는 아직 초기단계이다. 반복압입시험은 기존의 정적압입시험의 장점을 그대로 적용하여, 기존 표준화된 피로시험법을 보완 및 대체할 수 있다는 점에서 큰 가능성을 가진다. 따라서 본 논문에서는 구형압입자를 활용한 반복압입시험을 통해 구조건전성 평가를 위해 중요한 피로특성인 재료의 바우징거 효과와 라체팅 물성을 평가하는 모델을 개발하였다.

모델 개발을 위해 실험적으로 두 가지의 제어방식이 (변위제어 방식과 하중제어 방식) 활용되었다. 반복 변위제어 시험방식에서는 압입하중-변위커브 상에서 히스테리시스 루프가 나타남을 확인하였다. 접촉역학을 활용한 응력해석을 통해 압입 히스테리시스 루프는 이동성 경화에 기인한 바우징거 효과에 의해 발생함을 규명하였다. 압입시험에서 발생하는 바우징거 효과를 대표응력-변형률 방법을 도입하여 기존 표준화된 일축시험에서 나타나는 바우징거 효과와 연관성이

있음을 유도하였다. 이로부터 반복압입시험으로부터 기존 일축피로시험의 바우징거 효과를 예측할 수 있는 새로운 모델을 개발하였다.

반복 하중제어 시험방식에서는 반복적으로 압입하중이 인가됨에 따라 압입깊이가 계속적으로 증가하다가 특정 반복 하중 사이클에서 수렴하는 현상이 관찰되었다. 우리는 이 현상을 재료의 경화거동 관점에서 해석하였고, 압입깊이가 증가하는 거동과 일축피로시험의 라체팅 거동이 동등함을 확인하였다. 이로부터 우리는 재료의 라체팅 물성을 예측할 수 있는 새로운 모델을 개발하였다. 모델로부터 예측된 바우징거 효과와 재료 라체팅 물성은 기존 피로시험에서 도출된 결과와 비교하여 유효성을 검증하였다.

또한, 정적 플랫펀치 압입시험을 활용하여 정적 파괴특성을 평가하기 위한 기준을 개발하였다. 금속과 같은 연성재료는 압입시험에서 균열이 발생하지 않기 때문에, 많은 연구자들은 연속압입시험을 통해 금속재료의 파괴인성을 평가 하기 위해 실험적 혹은 이론적 모델을 개발하여 왔다. 대부분은 모델은 재료의 파괴거동에 따라 취성금속재료에 대한 모델과 연성금속재료에 대한 모델로 구분되었다. 취성금속재료 모델에서 예측된 파괴인성 값은 연성취성천이곡선의 하부온도영역에 해당하는 상대적으로 낮은 범위($K_{JC} < 120 \text{ MPa} \cdot \text{m}^{0.5}$)에 한정되어 있고, 연성금속재료 모델에서 예측된 파괴인성 값은 연성취성천이곡선의 상부온도영역에 해당하는

상대적으로 높은 범위 ($K_{JC} > 250 \text{ MPa} \cdot \text{m}^{0.5}$)에 한정되어 있다. 따라서 이 두 모델을 구분을 하는 것이 압입파괴인성 모델을 가동 중 구조물에 적용하는 데 있어 중요한 이슈이다. 우리는 플랫펀치 압입자를 활용하여 두 타입의 모델을 구분하기 위해 두 개의 중요한 인자를 제안하였다. 이 두 개의 인자는 플랫펀치 압입자 모서리와 균열 첨단의 응력 동등성과 압입자 하부 소성역 증가거동을 기반으로 압입커브에서 직접적으로 유도되는 파라미터로부터 결정되었다. 결정된 인자들로부터 개발된 파괴기준은 23 종의 금속재료에 대해 표준 파괴인성 시험법으로부터 측정된 결과와 비교하여 유효성이 검증되었다.

주요어: 반복압입; 플랫 펀치 압입; 바우징거 효과; 재료 라체팅; 취성파괴; 연성파괴; 구조 건전성

학번: 2010-20629

List of Publication

I. International Journal

1. Chan-Pyoung Park, Jung-Jun Lee, Seung-Kyun Kang, Young-Cheon Kim, Kwan-Sik Woo, **Seung-Won Jeon**, Dongil Kwon: Evaluation of high-temperature Vickers hardness using instrumented indentation system, *Material Science & Engineering A* 650 (2015) 15-19
2. **Seung-Won Jeon**, Kyung-Woo Lee, Junyeong Kim, WooJoo Kim, Chan-Pyoung Park: Estimation of Fracture Toughness of Metallic Materials Using Instrumented Indentation: Critical Indentation Stress and Strain Model, *Experimental Mechanics* (2016) 1-13
3. **Seung-Won Jeon**, WooJoo Kim, Junyeong Kim, Seung-Hoon Choi: Method for Evaluating Material Fracture Toughness Using Instrumented Flat Punch Indentation and Application to Low-temperature Embrittlement, *Engineering Fracture Mechanics* (*preparing for submission*)

II. Patents

1. Dongil Kwon, **Seung-Won Jeon**, Hee-Kwang Chang, Jung Hyun Ji: Indentation fatigue test module, PCT/KR2013/005560, PCT (2013) Seoul National University

2. 권동일, 전승원, 장희광, 지정현: 압입 피로 시험 모듈 (Indentation fatigue test module), 10-1455112, 대한민국 (2014) 서울대학교 산학협력단

3. 김준영, 권동일, 김광호, 전승원, 김우주, 최승훈: 연속압입시험법을 이용한 파괴인성 측정방법(Evaluating Method of The Fracture Toughness Using Instrumented Indentation testing), 10-2016-0095742, 대한민국 (2016) (주)프론틱스

4. Junyeong Kim, Dongil Kwon, Kwang-Ho Kim, Seung-Won Jeon, WooJoo Kim, Seung-Hoon Choi: Method for Evaluating Fracture Toughness Using Instrumented Indentation Testing, 15/269,012, USA (2016) Frontics Inc.

III. International Conferences (* indicates speaker)

1. Junyeong Kim*, Kyung-Woo Lee, Seung-Won Jeon, Dongil Kwon: Estimation of Fracture Toughness Using Instrumented Indentation Testing: Ductile/Brittle Fracture Models, Fourth International Indentation Workshop (IIW4), Seoul National University, Seoul, Korea (2011)

2. Hee-Jun Ahn*, Jong-Hyoung Kim, **Seung-Won Jeon**, June Sang Lee, Min-Jae Choi, Kwang-Ho Kim, Dongseong Ro, Dongil Kwon: Estimation of Stress-free State From Hardness Ratio For Evaluation of Residual Stress Using Instrumented Indentation Testing (IIT), ASME Pressure Vessel and Piping 2015, Boston, USA (2015)

3. **Seung-Won Jeon***, Junyeong Kim, Kyung-Woo Lee, Dongil Kwon: Estimation of Fracture Toughness of Metallic Materials Using Instrumented Indentation Testing, Fifth International Indentation Workshop (IIW5), Dallas, USA (2015)

IV. Domestic Conferences (* indicates speaker)

1. **전승원***, 김준영, 이진우, 권동일: 구조용강의 파괴인성 천이거동 해석을 위한 연속압입시험의 응용, 2011년도 대한금속·재료학회 추계 학술대회, 대전컨벤션센터(DCC) (2011)

2. 박찬평*, 김국환, 조원제, **전승원**, 권동일: 연속압입시험의 탄소성 응력해석을 통한 대표응력-대표변형률 결정, 제 25 회 첨단구조재료 심포지엄, 한국원자력안전기술원, 대전 (2011)

3. 전승원*, 김준영, 권동일: 피로특성 예측을 위한 연속압입시험법의 활용, 2012 년도 대한금속·재료학회 춘계 학술대회, 현대성우리조트(강원도 횡성) (2012)

4. 이진우*, 김준영, 조원제, 전승원, 권동일: 연속압입시험법을 이용한 금속재료의 샤르피 충격에너지 예측, 2012 년도 대한금속·재료학회 춘계 학술대회, 현대성우리조트(강원도 횡성) (2012)

5. 전승원*, 김준영, 권동일: 연속압입시험법을 이용한 AI 합금의 피로특성 예측, 제 26 회 첨단구조재료 심포지엄, 부산센텀호텔 (2012)

6. 전승원*, 김준영, 김지연, 권동일, 계장화 압입시험법을 이용한 API 강재의 피로특성 예측, 2013 년도 대한금속·재료학회 춘계 학술대회, 제주 국제 컨벤션센터 (2013)

7. 권동일*, 송원석, 전승원: 계장화 압입시험법의 국제표준화 동향과 기기의 국내개발현황, 2013 년도 대한금속·재료학회 춘계 학술대회, 제주 국제 컨벤션센터 (2013)

8. 안희준*, 박찬평, 전승원, 김지연, 권동일: 법공학 도입을 통한 안전사고 예방 및 대응체계 구축 방안에 대한 연구, 2013 한국안전학회 춘계학술대회, 서귀포 KAL 호텔 (2013)

9. 김준영*, 전승원, 이경우, 권동일: 연속압입시험을 이용한 금속소재의 파괴인성 평가, 2014 년도 재료 및 파괴부문 춘계학술대회, 서귀포 KAL 호텔 (2014)

10. 전승원*, 김준영, 권오민, 권동일: 연속압입시험법을 이용한 API 강재의 피로특성 예측, 2014 Materials Fair, 서울대학교 (2014)

11. 김준영*, 전승원, 이경우, 권동일: 연속압입시험을 이용한 금속소재의 파괴인성 평가, 2014 년도 대한기계학회 추계학술대회, 김대중 컨벤션센터(광주) (2014)

12. 안희준*, 김종형, 김준영, 전승원, 이경우, 권동일: 계장화 압입시험을 활용한 금속소재 물성 평가 연구, 2015 년도 대한기계학회 춘계학술대회 재료 및 파괴 부문, 서귀포 KAL 호텔 (2015)

13. 권동일*, 전승원, 김승규: 연속압입시험법의 멀티스케일 응용 및 국제표준화동향, 2015 년도 대한금속·재료학회 춘계 학술대회, 창원 컨벤션센터 (2015)

14. 김우주*, 김준영, 전승원, 권동일: Estimation of Fracture Properties of Metallic Materials Using IIT, 2016 년도 대한금속·재료학회 춘계 학술대회, 경주화백컨벤션센터 (2016)